Study of Radio Waves in Geospace via Spacecraft Observations and Numerical Simulations

Yasumasa KASABA

March 1997

I dedicate this thesis to
my parents Kyohei and Mineko Kasaba.

DOCTORAL THESIS
SUBMITTED TO
THE FACULTY OF ENGINEERING
KYOTO UNIVERSITY

Acknowledgments

I gratefully thank Prof. Hiroshi Matsumoto for addressing me the motivation for the present study and giving me a philosophical concept of space science and technology. I am grateful to Prof. Kozo Hashimoto for his continual guidance and discussion on planetary radio activities. I express my appreciation to Prof. Toshitaka Tsuda for his suggestions and the helpful advice of this thesis. Many thanks are due to Dr. Yoshiharu Omura for providing his original particle code, and for patient and valuable comments in his scientific and technological discussions. I am grateful to Mr. Hirotsugu Kojima for his advice in analyzing GEOTAIL data and his exciting, enjoyable and fruitful discussions. I would like to express my thanks to Dr. Hideyuki Usui and Dr. Naoki Shinohara for his technical advice and scientific discussions. I wish to express my hearty appreciation to Prof. Daniel Summers, Prof. Victor Krasovsky, Prof. David Nunn, Prof. Walter J. Heikkila, Dr. Yong Liang Zhang, and Dr. Zhi Liang Wang who gave me kind advice.

The data analyses of the GEOTAIL spacecraft were carried out with the help of a lot of researchers. This thesis mainly owes to GEOTAIL plasma wave data provided by the PWI team. I wish to express my thanks to Prof. Isamu Nagano, Dr. Satoshi Yagitani, and Dr. Xiang Yang Wu at Kanazawa University, Dr. Roger R. Anderson at the University of Iowa, Dr. Minoru Tsutsui at Kyoto Sangyo University, Dr. Toshimi Okada at Toyama Prefectural University, Dr. Takeshi Murata at Ehime University, Dr. Greg Crawford at Stanford Research Institute, and other members who have worked on constructing well-designed instruments and analysis packages. GEOTAIL particle data are provided by the LEP team. We would like to thank Prof. Toshinori Mukai and Dr. Yoshifumi Saito at the Institute of Space and Astronautical Science (ISAS), Prof. Toshio Terasawa at University of Tokyo, and Dr. Shinobu Machida at Kyoto University for their cooperation. GEOTAIL magnetic field data are provided by the MGF team. Thanks are due to Prof. Susumu Kokubun at Solar Terrestrial Environment Laboratory, Nagoya University, and Dr. Tatsundo Yamamoto at ISAS.

In chapters 2, 5, and 6, we use simultaneous data sets of the WIND spacecraft. WIND plasma wave data are provided by the WAVES team. I especially thank to Dr. Mike L. Kaiser and Dr. R. J. MacDowall at NASA Goddard Space Flight Center (GSFC), Dr. Mike J. Reiner at Hughes STX, Dr. Jean-L. Bougeret at Observatoire de Paris, and Prof. Paul J. Kellogg at Minnesota University. WIND particle data are provided by the SWE team. We would like to thank Dr. K. W. Ogilvie at NASA/GSFC. WIND magnetic field data are provided by the MFI team. Thanks are due to Dr. R. P. Lepping at NASA/GSFC.

Geomagnetic indices used in chapter 5, 6, and 7 are provided by Data Analysis Center for Geomagnetism and Space Magnetism, Kyoto University. We would like to thank to Dr. Toshihiko Iyemori at Kyoto University. Thanks are also due to Dr. Yu. I. Galperin for providing the structure models of the magnetosphere and the plasmasphere used in chapter 5. We would like to thank to Prof. Kouichiro Maeda at Hyogo Medical University and Dr. Tetsuya Kodama at National Aeronautical and Space Development Agency (NASDA) for providing information on the possibilities of low frequency radio astronomy and precursor radio wave observations associated with large earthquakes.

Many thanks are also due to all of the members at Radio Atmospheric Science Center (RASC), Kyoto University. I gratefully thank all members of RASC office to provide the best environment to work as a graduate student. I express my appreciation to Prof. Iwane Kimura and Prof. Shoichiro Fukao for experienced suggestions in the seminars. I would like to thank Mr. Taketoshi Miyake and all students for their help and fruitful discussions. I wish to thank Ms. Keiko Miwa for her encouragement and secretarial help. I gratefully thank Miss Tomoko Taniguchi for her daily efforts to transport huge number of GEOTAIL data sets from ISAS. I express my appreciation to Miss Reiko Kita, Miss Nanako Izumi, and Ms. Mitsuko Abe to make me at ease and provide the best atmosphere. I would also thank the previous members of RASC, Mr. Satoshi Chikuba at JR Toukai Co., Mr. Hiroaki Hamada at NEC Co., Mr. Masaya Yamane at NTT Co., Mr. Masatoshi Furukawa at Sharp Co., Miss Satoko Horiyama at NASDA, Miss Junko Koizumi at Ministry of Posts and Telecommunications, and all the member of the participants. Whole computer simulations are carried out on the KDK system at RASC, Kyoto University.

Finally I thank my parents Kyohei and Mineko Kasaba, my grandparents Seiuemon and Iku Kasaba, Tomoe Furuichi, and late my grandfather Heiuemon Furuichi, for their continuous encouragement.

Abstract

In the present thesis, we mainly use data sets of the GEOTAIL spacecraft to investigate low frequency radiations generated in the geospace, i.e., space around the Earth. These radio waves can provide real-time information around their sources and on their propagation paths to distant observers. Therefore, the combinations of remote/in-situ observations and numerical simulations of these radio waves are possible to become powerful tools to study global phenomena in the geospace. Based on such techniques, we present numerous new facts with assistance of the GEOTAIL/WIND spacecraft and numerical simulations.

In Chapter 2, we investigate the geometry of terrestrial electron foreshock by remote observations of $2f_p$ radiation. We determine the geometry of the $2f_p$ radio source by three methods; 'two-spacecraft triangulation by collaboration with WIND'. 'statistical analysis of direction finding', and 'statistical analysis of bifurcation phenomena associated with solar wind density jump'. We present three new results; (1) The $2f_p$ radio source is superposed on upstream and downstream wings of the electron foreshock. When the interplanetary magnetic field (IMF) displays a systematic rotation, the $2f_p$ radio source follows the motion of the electron foreshock. These results support the idea that $2f_p$ radiation is generated from strong Langmuir waves in the electron foreshock. (2) The region close to the contact point of the tangential IMF line to the bow shock surface is not bright source of the $2f_p$ radiation. This should be due to lack of sharp electron beams, because of a shortage of flight time for beam formation through the time-of-flight effect. (3) The distance of source region from the Earth is limited below 100 R_E. This should be due to consumption of free energy of the electron beam enough to excite the $2f_p$ radiation.

In Chapter 3, we further investigate the physical conditions in the terrestrial electron foreshock by in-situ observations of the $2f_p$ radiation, other plasma waves, and energetic particles. First, we investigate the distributions of plasma waves and energetic particles in the foreshock region by mapping analyses. We find that the $2f_p$ radio source centroid is superposed on the electron foreshock, at a distance of 5-40 R_E from the contact point. This suggests the formation and the consumption of sharp electron beams through the time-of-flight effect and wave–particle interactions. We also find that the flux of the $2f_p$ radiation is positively correlated with the solar wind kinetic flow and the location of the contact point on the bow shock surface. These results suggest that the $2f_p$ radiation can work as a remote sensing probe for the population of energetic electron beams. On the other hand, we also investigate the direct observations of plasma waves and energetic particles on and across the electron foreshock. We confirm that the density of the electron quasi-beam component decreases faster than the energy on the way from the contact point. This favors the beam formation process through the time-of-flight effect. We also find the clear enhancement of electric field at $2f_p$ and below 1 kHz at the leading edge of the electron foreshock. Ratio of 'local' wave at $2f_p$ to Langmuir wave is below -40 dB, while that of electrostatic wave below 1 kHz is below -10 dB.

In Chapter 4, we investigate the physical processes in the terrestrial electron foreshock by numerical simulations in order to generate electrostatic and electromagnetic $2f_p$ waves. Our numerical simulations are executed by electromagnetic particle code,

KEMPO, for 1D and 2D periodic systems. In 1D periodic systems, electrostatic $2f_p$ waves are generated associated with intense beam-excited Langmuir wave at $k = 2k_L$, where k_L is wave number of Langmuir wave. Growth of electrostatic $2f_p$ waves is strongly correlated with peak amplitude of beam-excited Langmuir waves. Features of this wave support the generation process of wave–wave coupling of two beam-excited Langmuir waves. Typical intensity ratio of electrostatic $2f_p$ waves to Langmuir waves is below −40 dB, which is consistent with in-situ observations presented in Chapter 3. On the other hand, we successfully reproduce electromagnetic $2f_p$ waves in a 2D periodic system. Growth of electromagnetic $2f_p$ waves is strongly correlated with amplitude of backscattered Langmuir waves, and independent of the electrostatic $2f_p$ waves. Features of this wave support the generation process of wave–wave coupling of beam-excited and backscattered Langmuir waves. Typical growth time of electromagnetic $2f_p$ wave is about 200-400/Π_e, which does not contradict to thickness of the electron foreshock. Typical amplitude ratio of electromagnetic $2f_p$ waves to Langmuir waves is below −80 dB, which is too weak to detect local enhancement at the electron foreshock.

In Chapter 5, we investigate the global dynamics around the plasmapause during substorms by remote observations of 'continuum enhancement', short-lived enhancement of the nonthermal continuum radiation generated at the plasmapause by injected electrons into the local midnight zone associated with each substorms. We use three features of this radiation as a remote sensing probe to study real-time processes around the plasmapause associated with substorms; 'the differences with the classical continuum', 'the variation of the frequency range', and 'the variation of the banded frequency structure'. We find three points; First, the continuum enhancement and the following classical continuum are generated by a series of injected electrons associated with the onset of the same substorm which show dawnward motion by gradient and curvature drift. Secondly, sometimes the continuum enhancement consists of fast and main components which are distinguished by the duration time and the rising rate in frequency. The fast component is generated first at the plasmapause in the local midnight zone by the low energy electrons, while the main component is generated later on the dawnside plasmapause by the higher energy electrons. Thirdly, rising of the spacing of the banded frequency structure indicates decrease of the plasmapause radius which continues for ~1 hour after the onset of each substorms. Radius of the plasmapause is converged long after substorm and inversely correlated with Kp index in the long time scale. Sometimes we also observe the increase of the radius after the decrease event. Since the increase rate exceeds the value expected from the refilling rate into the outer plasmasphere from the ionosphere, the decrease of the plasmapause radius is caused not only by the peeling off of the plasma but also by the relaxation of compression.

In Chapter 6, we investigate the global dynamics in the auroral region by remote observations of auroral kilometric radiation (AKR). We search for the possible dependences on the factors which may affect generation and propagation conditions of AKR; 'the geomagnetic disturbances', 'the longitude of the source region', and 'the angle between the geomagnetic axis and the Sun-Earth line'. Based on the results of these analyses, we evaluate the characteristics of generation and propagation conditions of AKR in four points; (1) Extension of the illumination region of AKR is larger at the lower frequency range. This feature should basically be explained by the propagation of AKR determined by the difference of the source position and the propagation path. (2) In geomagnetic disturbed phase, the illumination region extends to more duskward at the lower frequency range. This suggests that the source region of AKR extends to duskward especially at high altitude. We also suppose that such duskward extension is not evident at lower altitude because of the blocking of the auroral plasma cavity formation caused by density increase in the duskside plasmasphere. (3) We find the dependence on the longitude of the source region especially at the higher frequency range in the same manner as that of optical auroral activity. This suggests that the population of energetic electrons at lower altitude is controlled by the altitude of the magnetic mirror point. Lack of such dependence at the lower frequency range might be caused by the duskward extension of the source region. (4) From the dependence on the angle between the geomagnetic axis and the Sun–Earth line, we show that AKR is more active on the winter hemisphere especially at the higher frequency range. The asymmetry of precipitating electron population is a possible candidate, while we also propose the asymmetry of the auroral plasma cavity, blocking of its formation on the summer hemisphere, caused by density increase in the inner plasmasphere.

In Chapter 7, we show possibility of the techniques presented in this thesis for future planetary investigations. And as an example, we show the remote observations of the Jovian hectometric (HOM) and kilometric (KOM) radiations associated with a first historic event, the impacts of Comet Shoemaker-Levy 9 (SL-9). Some activities in X-ray and decimetric synchrotron radiations indicate some strong perturbations at the impact sites gave non negligible changes in the inner magnetosphere, directly or indirectly. However, GEOTAIL detected no clear enhancement of the Jovian non-thermal HOM and KOM radiation in the whole impacts' period. This suggests that there was no clear variation of the plasma activity in the Jovian outer magnetosphere induced by mass loading or direct interactions between the cometary fragments and Jovian outer magnetosphere along the trajectories of cometary fragments. This conclusion is consistent with the results of some ground-based DAM/optical observations.

In Chapter 8, we summarize the present studies and present the possible future projects for the development and the extension of the road toward the space.

Contents

Chapter 1

General Introduction

1.1 Introduction

'Space' was first dramatically demonstrated by Johannes Kepler in the 17th century. He was not only a famous scientist, but also a first novelist of a scientific fiction. He wrote a masterpiece on the space voyage entitled as 'Somnium', a Latin word that means 'dream' [*Sagan*, 1980]. The long dream finally came true just 40 years ago, by the launch of the first artificial satellite, SPUTNIK on 4 October 1957.

For these 40 years, steady efforts of many people have been accumulated to build the road to the space. Unfortunately, it was true that the past space development had been strongly influenced by national prestige and military demands. Such situations were changed by the end of the cold war, at the beginning of this decade. It is sure that wastes of human and material resources become not to be allowed. However, on the other hand, spread of international collaborations and opening of technological information compensate enough and stimulate whole space activities. Especially, 'geospace', space around the Earth, is finally becoming essential and daily space for our life.

In a practical aspect, industries associated with space technology are really standing up. New-generations of communications and broadcasting satellites transport huge information across borders and strongly drive the present countries toward a borderless world. In this decade, Global Positioning System (GPS), which was limited in military usage, is opened to public applications and explosively becoming one of key infrastructures of the future society. At the beginning of 1997, the first communications satellite consisting of 'IRIDIUM project' was launched, and opened the new era of worldwide portable telephone networks. At the end of this century, first international space station 'FREEDOM' will provide various jobs on the orbit for people from USA, Europe, Canada, Russia, and Japan. This decade will be estimated as takeoff era of the space industry.

In a scientific aspect, new international projects are going on now. Powerful satellite observatories are bringing discovery era in all over the astronomical activities from radio to γ-ray radiations. Intensive observations to the planet Earth provide valuable information on complicated environmental problems, and have deepened our recognition that is symbolized by a word, "a spaceship Earth". This decade is also the beginning

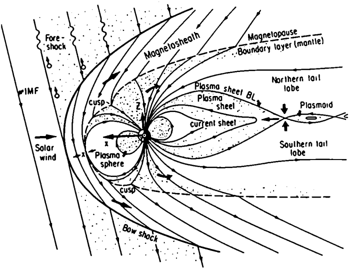

Figure 1.1: Side view of the terrestrial magnetosphere, showing the solar wind [*Sonnerup*, 1985].

of second phase of planetary explorations following the discovery era in early days, and various spacecraft toward Moon, Venus, Mars, Jupiter, and asteroids are launched or planned one after another. Discoveries of extraterrestrial bacterium-like organic matters in a meteorite from Mars and ice on the Moon further accelerate this tendency. Accumulations of these efforts are steadily changing quality of the present civilization. Viewpoints from the space are already indispensable to construct the sustainable civilization in the future.

Of course, our country is not an exception. Space programs of Japan have been promoted by a unique system with two national agencies, National Aeronautical and Space Development Agency (NASDA) and The Institute of Space and Astronautical Science (ISAS). Especially, scientific programs promoted by ISAS have obtained international praises as "Small is beautiful! Quick is beautiful!". On these bases, various international collaborations are carried out or planned now. 'International Solar-Terrestrial Physics' (ISTP) program is one of such programs. In the space around the Earth, interaction between terrestrial atmosphere, magnetic field, and solar wind plasma flow forms a region called 'the geospace'. The most evident feature of ISTP program is simultaneous multi-spacecraft observations. Compared with past single-satellite observations, ISTP program is expected to provide direct views of global phenomena in the geospace.

However, majority of observed results by individual satellites is essentially local information. Therefore, especially for global and fast-variable phenomena, multi-satellite observation is not always almighty. Although imaging techniques to obtain global features at a time are expected to give breakthrough to the global phenomena, they are still incomplete. Fortunately, there are some low frequency radio sources in the geospace. They can provide real-time information in the sources and on the propagation paths to distant observers. In the present thesis, we mainly use data sets of the GEOTAIL spacecraft, one of ISTP satellites, and try to get global information in the geospace by spacecraft observations and numerical simulations of these radio waves. Such investigations will also contribute the whole ISTP program, research of terrestrial environments, and future space activities.

1.2 The geospace: The magnetosphere and the plasmasphere

First, we briefly introduce structure of the geospace. The geospace roughly consists of 'the magnetosphere' and 'the plasmasphere'.

The magnetosphere is the terrestrial plasma atmosphere formed by interaction between the solar wind and the terrestrial magnetic field. Namely, the solar wind blows around the Earth, compresses the original dipole-like magnetosphere, and forms a long anti-sunward tail [*Chapman*, 1931]. The magnetosphere consists of various regions characterized by different plasma and magnetic field parameters (Figure 1.1).

At the head of the magnetosphere, the bow shock is formed because velocity of the solar wind exceeds the local sound or Alfvén velocity. Some particles are reflected to upstream region along interplanetary magnetic field (IMF) lines, and form the foreshock region in the downstream of the IMF lines tangent to the bow shock. In the magnetosheath, a region behind the bow shock, the solar wind flow is reduced and thermalized. The boundary between the magnetosheath and the magnetosphere is called the magnetopause. Inside the magnetopause, density is depressed and global structure is generally supported by pressure of magnetic fields connected to the Earth.

The structure of the magnetosphere is largely different between in the dayside zone and in the nightside zone. The dayside magnetosphere is compressed but generally maintains dipole-like configuration. On the contrary, the nightside magnetosphere shows a cylindrically-shaped region called the magnetotail. The boundary region between dayside and nightside magnetosphere is called the polar cusp. The magnetotail consists of the tail lobe, the plasma sheet, and other parts indicated in Figure 1.1. The tail lobe occupies most of the cylindrically-shaped magnetotail with low β plasma. The plasma sheet is situated between north and south lobe region with high β plasma. The marginal region at the shoulder of the plasma sheet is called the plasma sheet boundary layer (PSBL). The PSBL should play important roles as a source region of the auroral particle since the PSBL magnetic field lines are connected to the high-latitude auroral region.

The plasmasphere is a region between the upper ionosphere and the inner magnetosphere. Plasma particles in the plasmasphere are moved associated with rotation of

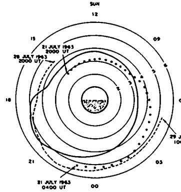

Figure 1.2: The location of the plasmapause as a function of magnetic local time and radial distance deduced from the dispersion of electron whistlers for three days [*Carpenter*, 1966].

the Earth. These plasma particles are supplied from upper ionosphere by diffusion and trapped in the magnetic tubes. Since the volume of magnetic tubes with fixed sectional areas at the upper ionosphere are larger at high latitude, typical fulfilling time by supply of plasma particles from the upper ionosphere is larger in high-latitude (i.e., outer) magnetic tube. Fulfilling time calculated with typical physical parameters in the upper ionosphere is ~1 day at $L = 2$ and ~5 days at $L = 5$.

At the border between the plasmasphere and the magnetosphere, large density gap called the plasmapause is formed. Radius of the plasmapause is not symmetric on the magnetic equatorial plane, i.e., usually larger on the duskside than on the dawnside as indicated in Figure 1.2 [*Carpenter*, 1966].

In the magnetosphere, dawn-to-dusk electric field is induced by rotation of the Earth and interaction with the solar wind flow. This induces large Earthward convection in the nightside magnetosphere by $\mathbf{E}\times\mathbf{B}$ drift. In the inner magnetosphere, plasma motion is also affected by gradient and curvature drift whose amount is correlated with charge and kinetic energy of particles. By both effects, energetic electrons and ions show dawnward and duskward motions separately, as indicated in Figure 1.3 [*DeForest and McIlwain*, 1971].

1.3 Energy conversion processes

Around the magnetosphere, several kinds of activities are induced by energy conversion from kinetic energy of the solar wind flow. Here, we consider two major processes occurred at the bow shock and in the magnetotail.

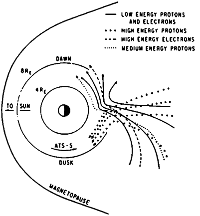

Figure 1.3: Trajectories of electrons and protons in the magnetosphere [*DeForest and McIlwain*, 1971].

1.3.1 The bow shock: Formation of the foreshock

At the bow shock, part of kinetic energy of the solar wind flow is converted not only to the thermal energy of downstream plasma particles but also to the kinetic energy of upstream particles streaming away from the bow shock along the IMF lines. Velocity distributions of such foreshock particles are spatially structured in a systematic way depending on distance from the IMF line tangent to the bow shock (Figure 1.4). The energetic electrons above 1 keV are confined to a thin sheet just behind the IMF lines tangent to the shock, while the moderate electrons below 1 keV extend over a broad region behind the magnetic tangent surface. The region containing these backstreaming electrons is the electron foreshock. The energetic ions extend to further downstream region that is called the ion foreshock. Such structure is formed by acceleration at the bow shock and propagation in the foreshock [cf. *Fitzenreiter*, 1995].

Magnetic reflection is suggested as an acceleration mechanism based on three features of upstream particles; high energization at the nearly perpendicular shock, velocity distributions with a high energy tail, and a loss cone structure at energies below 1 keV. Adiabatic arguments yield that the average energy parallel to the magnetic field of a reflected particle is $2m_e v_{sw}^2/\cos^2\theta_{B_n}$, where v_{sw} is the solar wind velocity and θ_{B_n} is the angle of magnetic field to the shock normal [*Leroy and Mangeney*, 1984], and the density of reflected particles is proportional to density of cold or suprathermal particles in the solar wind [*Wu*, 1984; *Leroy and Mangeney*, 1984]. On the other hand, the fraction of particle reflection is positively correlated with the maximum magnetic field at the bow shock, which is correlated with the shock Mach number and particle β [*Mellott and Livesey*, 1987]. Consequently, density and energy of the reflected particle

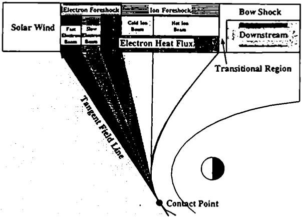

Figure 1.4: Structure of the terrestrial foreshock region [*Matsumoto et al.*, 1997].

beams are determined by velocity, density, temperature and magnetic field in the solar wind [*MacDowall*, 1995].

Upstream leakage is also suggested as other acceleration mechanism based on two features; the shock-modified particle fluxes in the mirror loss cone and upstreaming suprathermal particles within the shock layer at the contact point. Suprathermal electrons with energies up to 20 keV are commonly present in the downstream region of the quasi-perpendicular portion of the bow shock, but rarely seen in that of the quasi-parallel portion. The flux of such suprathermal electrons peaks just downstream from a region of the shock overshoot, and falls off with increasing penetration into the magnetosheath. Observed suprathermal electron flux appears as a high-energy tail with power law with exponent $-3 \sim -4$, merged onto the downstream thermal solar wind distribution.

There is a further spatial ordering of the backstreaming electrons according to energy due to a time-of-flight effect on particles propagating from the bow shock. Particles leaving the shock surface with an initial upstream velocity parallel to the magnetic field are moved to downstream by a cross-field drift due to the motional electric field. Therefore, foreshock particles have velocity components of

$$v_{\parallel} = v cos\alpha \quad (1.1)$$

$$v_{\perp} = \mathbf{B} \times (\mathbf{v}_{sw} \times \mathbf{B})/B \quad (1.2)$$

where v is the particle velocity, α is the particle pitch angle, $\mathbf{B}$ is the magnetic field, and $\mathbf{v}_{sw}$ is the solar wind velocity vector [cf. *Fitzenreiter*, 1995]. That is to say, faster electrons travel further upstream than slower ones, and slow ions travel further downstream than electrons.

1.3.2 The magnetotail: Birthplace of substorms

Kinetic energy of the solar wind flow is also converted to the geomagnetic activities through reconnection process of magnetic field in the magnetotail. This process is named as substorm. The Earth-origin magnetic fields are connected with IMF at the dayside magnetopause, and conveyed anti-sunward in the magnetosheath associated with the plasma convection in the magnetosphere. These magnetic fluxes are gradually accumulated on the magnetotail, and converted to energy of substorm phenomena. Magnetospheric substorm process is grouped into four stages; quiet phase, growth phase, expansion phase, and recovery phase [cf. *Murata*, 1995].

At the quiet phase, the interactions between solar wind and the magnetosphere are weak. Large scale convection remains constant in the magnetosphere. Input energy from the solar wind and output energy dissipated in the ionosphere and the magnetosphere are balanced. These conditions are realized when the IMF orientation keeps northward because the northward IMF can hardly cause the reconnection at the dayside magnetopause.

At the growth phase, the southward turning of the IMF drives the reconnection at the dayside magnetopause. The reconnected magnetic field lines are conveyed to the magnetotail, and gradually increase the total magnetic flux in the tail lobe. The flux accumulation is also regarded as a permeation of the electric field $\mathbf{E}$ (= $\mathbf{v}_{sw} \times \mathbf{B}$) into the magnetosphere. This electric field is equivalent to additional dawn-to-dusk electric field that increases the magnetospheric convection. Breaking down of the pressure balance between in the tail lobe and in the plasma sheet leads the thinning of the plasma sheet. The original dipole-like fields of the Earth change to the tail-like configuration. General duration of this stage is from 40 minutes to 1 hour if the IMF orientation keeps southward.

At the expansion phase, the stored magnetic energy in the magnetosphere is eventually released through the reconnection process in the magnetotail. This time is identified with aurora breakup associated with expansion to poleward and duskward. A simple substorm lasts ~60 minutes, while it is hard to distinguish each substorm process when orientation of IMF is kept southward. The reconnected magnetic field lines rapidly return to the dipole-like configurations after the reconnection.

At the recovery phase, the energy storage into the magnetosphere ceases when the IMF orientation alters into northward. At the beginning of this phase, poleward expansion of the aurora illumination region finishes. The magnetospheric convection decreases and magnetic pressure in the lobe is reduced. The thickness of the plasma sheet gradually recovers up to the original level.

1.4 Radio activities in the geospace

For more than 20 years, the Earth has been known as a bright radio source. Theories to explain these non-thermal radio emissions can be divided into (A) direct-conversion mechanisms and (B) mode-conversion mechanisms, and both can be subdivided into 'linear' and 'nonlinear' processes [cf. *Lee*, 1989]. In the direct-conversion mechanisms, electromagnetic (EM) waves are directly generated by plasma instabilities. On the

	frequency	source	mechanism	power
$2f_p$	twice of f_p in the solar wind	the electron foreshock	wave–wave coupling? [mode-conversion/non-linear]	10^{3-4} W
continuum	local f_p – 500 kHz	equator of the plasmapause	$(n+1/2)f_g \rightarrow f_{UHR}$ [mode-conversion/linear]	10^{5-6} W
AKR	100–600 kHz	plasma cavity in the auroral zone	cyclotron maser instability [direct-conversion/non-linear]	10^{7-8} W

Table 1.1: Summary of radio activities in the geospace.

other hand, in the mode-conversion mechanisms, electrostatic (ES) waves are produced first and then converted into EM waves.

The Earth has three kinds of radio sources; the $2f_p$ radiation from the electron foreshock, the nonthermal continuum radiation from the equatorial plasmapause, and the auroral kilometric radiation (AKR) from the auroral region (Table 1.1). We should get real-time information of physical conditions in the source region and on the propagated path through extensive observations of these radiations.

$2f_p$ radiation

The $2f_p$ radiation is narrow line electromagnetic emission at twice the solar wind electron plasma frequency, f_p, and shows relative smooth variation in intensity and frequency associated with solar wind conditions [*Gurnett*, 1975; *Gurnett and Frank*, 1976]. The $2f_p$ radiation is rarely observed deep in the ion foreshock nor behind the bow shock. It appears that the $2f_p$ radiation is strongly scattered by density fluctuations in the ion foreshock and reflected by density overshoot at the bow shock [*Lacombe et al.*, 1988].

The $2f_p$ radiation is believed to be generated in the electron foreshock close to the IMF line tangent to the bow shock. In the electron foreshock, strong Langmuir waves are generated by backstreaming energetic electron beams [*Anderson et al.*, 1979; *Anderson*, 1981; *Anderson et al.*, 1981]. Therefore, the $2f_p$ radiation is believed to be generated by these Langmuir waves. Several mechanisms have been proposed to explain how the $2f_p$ radiation is generated.

The first is wave-wave conversion process induced by 'the oscillating-two-stream instability' [*Filbert and Kellogg*, 1979]. In this mechanism, the $2f_p$ radiation is generated through the three-wave nonlinear process

$$L + L \rightarrow T \tag{1.3}$$

where L is beam-driven Langmuir wave and T is the transverse wave, which satisfy conditions of $\mathbf{k}_L + \mathbf{k}_L = \mathbf{k}_T$ and $\omega_L + \omega_L = \omega_T$, where $\mathbf{k}$ is the wave vector and ω is wave number of each component.

The second is that the ion acoustic wave leads to the generation of the transverse wave through wave–wave interaction [*Cairns and Melrose*, 1985; *Cairns*, 1988],

$$L \pm S \rightarrow L' \tag{1.4}$$

$$L + L' \rightarrow T \tag{1.5}$$

where S is ion acoustic wave, and L' is Langmuir wave produced by backscattering of the beam-driven Langmuir wave L off the ion acoustic wave S (or thermal ions).

The last is based on the mode-conversion from electrostatic $2f_p$ wave [*Yoon et al.*, 1994]. The electron beam first leads to the excitation of electrostatic quasi-normal mode at $2f_p$, which appears in the dispersion relation changed by interaction of the beam with Langmuir waves. Such quasi-mode has small wave number close to the electromagnetic branch, and is easily converted to electromagnetic $2f_p$ wave in the perturbed region.

Nonthermal continuum radiation

The nonthermal continuum radiation is electromagnetic emission at frequencies from local plasma frequency to several hundred kHz, characterized by smooth variation in intensity and frequency continuing for several hours [*Gurnett and Shaw*, 1973; *Brown*, 1973]. 'Trapped component' below the local solar wind plasma frequency is confined to the magnetosphere by reflection at the magnetopause, and shows conglomerate broad band spectrum with low modulation index. 'Escaping component' above the solar wind plasma frequency propagates outside of the magnetopause, and shows banded frequency structures with large modulation index.

The nonthermal continuum radiation is generated in a broad source region at the geomagnetic equator close to the plasmapause in 4-14h LT zone [*Gurnett*, 1975; *Gurnett and Frank*, 1976; *Kurth et al.*, 1981]. The nonthermal continuum radiation is believed to be generated in the region with a large density variation, like the plasmapause, through the linear mode-conversion process from the electrostatic instabilities near the upper-hybrid resonance frequency at $(n + 1/2)f_g$ to the O-mode radio waves [*Gurnett and Frank*, 1976; *Jones*, 1976; *Jones*, 1985]. The conversion efficiency calculated by using cold plasma theory in a one-dimensional inhomogeneous plasma is in the range of 10^{-2}–10^{-3} [*Okuda et al.*, 1982].

Auroral kilometric radiation

Auroral kilometric radiation (AKR) is intense radio emission in frequency of ~100-600 kHz, characterized by fast variation in intensity and frequency during geomagnetic substorm [*Gurnett*, 1974; *Kurth et al.*, 1975; *Alexander and Kaiser*, 1976; *Benson and Calvert*, 1979].

AKR is generated by the electron cyclotron maser process, one of non-linear direct-conversion mechanisms [*Wu and Lee*, 1979], at the frequency close to the local electron gyrofrequency in the auroral plasma cavity ($f_p/f_g < 0.3$) along the nighttime auroral field lines, at a radial distance of 1.5-3 R_E. Generation of AKR is closely related with the precipitating inverted-V electrons with energy of > 1 keV. On the other hand, the plasmapause often prevents propagation of AKR at a distance below 10 R_E [cf. *Hashimoto*, 1984].

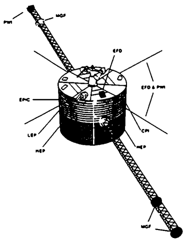

Figure 1.5: Configuration of the GEOTAIL spacecraft [*Nishida*, 1994].

1.5 The GEOTAIL spacecraft

Here, we present overview of the GEOTAIL spacecraft [cf. *Nishida*, 1994]. The GEOTAIL spacecraft was launched on 24 July 1992, from Cape Canaveral, Florida, USA, by Delta II launch vehicle. This is a joint program of the ISAS of Japan and NASA of USA. ISAS developed the spacecraft and provided about 2/3 of the science instruments, while NASA provided the launch and about 1/3 of the science instruments. The spacecraft is operated from ISAS but the telemetry is received by both agencies.

1.5.1 Spacecraft

The GEOTAIL spacecraft has a cylindrical shape with diameter of 2.2 m and height of 1.6 m. Two masts that are 6-m long are deployed symmetrically to separate the magnetometers from the main body, and four 50-m antennas are deployed to measure the electric field from DC to 800 kHz. The configuration of the spacecraft is illustrated in Figure 1.5. The spin axis is inclined sunward and makes an angle of 87° with respect to the solar ecliptic plane. The spin rate is about 20 rpm. Data are recorded continuously in two sets of the onboard data recorders at 16 kbps and dumped to the NASA Deep Space Network. In addition, there is a real-time data transmission at 64 kbps when GEOTAIL can transmit to the Usuda Deep Space Center of ISAS.

Item	Description	Range	PI(*), co-I
Electric Field (EFD)	Spherical probe and wire antenna Electron boomerang Ion emitter	dc-40Hz (2 comp) dc-10Hz (3 comp)	K. Tsuruda* F.S. Mozer R. Schmidt
Magnetic Field (MGF)	Fluxgate Search coil	dc- 8Hz (3 comp) 0.5-50Hz (3 comp)	S. Kokubun* M. Acuña D. H. Fairfield
Plasma (LEP)	Ion/electron 3-dim vel. distribution Solar wind ions Ion mass/energy spectrum	6eV - 36keV/q 100eV - 8keV/q 5eV - 25keV/q	T. Mukai*
Plasma (CPI)	Ion/electron 3-dim vel. distribution Solar wind ions Ion mass/energy spectrum	1eV - 50keV/q 150eV - 7keV/q 1eV - 50keV/q	L.A. Frank*
Energetic Particles (HEP)	Low energy particles Ion/electron burst Medium energy ion isotope ratio High energy ion isotope ratio	2keV - 1.5MeV/n 0.7 - 3.5MeV/n 5 - 50MeV/n 20 - 100MeV/n	T. Doke* B. Wilken
Energetic Particles (EPIC)	Ion charge state/mass/energy Ion mass and energy Electron energy	30 - 230 keV/q > 50 keV - 5MeV > 30 keV	D. J. Williams*
Plasma Waves (PWI)	Frequency sweep Multichannel analyzer Waveform capture	E: 25Hz-800kHz H: 25Hz-12.5kHz 10Hz - 4kHz	H. Matsumoto* R. Anderson

Table 1.2: GEOTAIL scientific investigations [*Nishida*, 1994]

Band	Frequency Range	Freq. Step	Bandwidth	Source	Sweep
1	24 Hz ~ 200 Hz	1.3 Hz	2.6 Hz	B and E	64 sec
2	200 Hz ~ 1600 Hz	10.7 Hz	10 Hz	B and E	64 sec
3	1.6 kHz ~ 12.5 kHz	85.4 Hz	85 Hz	B and E	8 sec
4	12.5 kHz ~ 100 kHz	683 Hz	680 Hz	E only	8 sec
5	100 kHz ~ 800 kHz	5.47 kHz	5.4 kHz	E only	8 sec

Table 1.3: Specification of the SFA [*Matsumoto et al.*, 1994].

1.5.2 Scientific instruments

Seven sets of scientific instruments are on GEOTAIL. These are listed in Table 1.2 with their frequency/energy ranges and the investigators.

This thesis mainly owes to the Plasma Wave Instrument (PWI). The PWI is composed of 3 distinct receivers with different frequency and time resolutions: (1) the Sweep Frequency Analyzer (SFA), (2) the Multi-Channel Analyzer (MCA), and (3) the Wave-Form Capture (WFC) [*Matsumoto et al.*, 1994]. The first two sets of receivers are devoted to measuring wave spectra, while the last one is designed to capture wave forms. The SFA covers from 24 Hz to 800 kHz for the electric field and from 24 Hz to 12.5 kHz for the magnetic field with 8 linear receivers listed in Table 1.3. Each receiver of the SFA has frequency resolution of 1/128 of its frequency bandwidth and time resolution of 8 seconds above 1.6 kHz and 64 seconds below 1.6 kHz. The MCA provides data of coarser frequency resolution and higher time resolution than those of the SFA. The MCA covers from 5.6 Hz to 311 kHz for the electric field and from 5.6 Hz to 10 kHz for the magnetic field with logarithmically ordered 20 and 14 channels, respectively. The bandwidth of filters are ±15% below 10 kHz or ±7.5% above 10 kHz of the channel center frequency. Time resolution is 0.25 or 0.5 seconds which depends on the data transmission format. The WFC provides wave form data to investigate the detailed wave characteristics from 10 Hz to 4 kHz. The WFC is usually operated under the Memory mode. In this mode, the WFC is triggered in 5 minutes intervals and obtains wave form data for 8 seconds.

These receivers are connected to two sets of electric dipole antenna systems, and two sets of tri-axial search coils. Electric dipole antenna systems, a wire dipole antenna (WANT) and a pair of top-hat probe antennas (PANT), have 100 m tip-to-tip length and are extended in the spin plane of the spacecraft that is stabilized close to the ecliptic plane. Tri-axial search coils, the PWI-SC and the MGF-SC, measure wave magnetic fields over a frequency up to 12 kHz and 1 kHz, respectively.

In this thesis, we also used data obtained from the Magnetic Field instrument (MGF) [*Kokubun et al.*, 1994] and the Low Energy Plasma experiments (LEP) [*Mukai et al.*, 1994]. The MGF consists of three sensors; two fluxgate magnetometers (16 Hz and 4 Hz sampling rate) and a search coil magnetometer (128 Hz sampling rate). We use 3-seconds averages of vector magnetic field data. On the other hand, The LEP can obtain energy-per-charge analysis of three-dimensional velocity distributions of ions and electrons from several eV/q to 43 keV/q with logarithmically ordered 32 channels, using seven sensors whose look directions are separated by 22.5° in the spacecraft meridional plane. Velocity distributions are obtained in a period of four spins (12 seconds), while the velocity moments up to the third order are calculated onboard every spin period.

1.5.3 Orbit

The primary purpose of the GEOTAIL mission is to study structure and dynamics of the geomagnetic tail. In the first phase of the mission, GEOTAIL stayed in the Distant-Tail orbit and explored the distant magnetotail beyond the lunar distance by adjusting its orbit by a number of double lunar swing-by maneuvers. In the second phase of the mission, GEOTAIL was thrown into the Near-Tail orbit in the fall of 1994 and the apogee is lowered of earthward of lunar orbit. The orbit after February 1995 has an apogee of $\sim$30 R_E, a perigee of $\sim$10 R_E, and the orbital period of $\sim$7 days. Such trajectories are also suitable for investigations of the foreshock region. Trajectories of GEOTAIL in the Geocentric Solar Ecliptic (GSE) coordinates is indicated in Figure 1.6.

1.6 Other data sets used in this thesis

1.6.1 The WIND spacecraft

Original start year of ISTP was 1992. However, launch schedules of other ISTP satellites delayed and we did not have enough chance so far to make simultaneous observations with them. Fortunately, the WIND spacecraft (Figure 1.7) was successfully launched

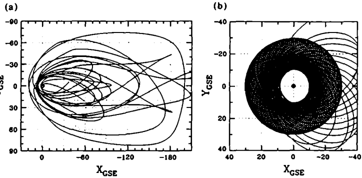

Figure 1.6: Orbit of GEOTAIL in the geocentric solar ecliptic (GSE) coordinates. (a) the Distant-Tail orbit from September 1992 to October 1994; (b) the Near-Tail orbit from November 1994 to October 1996.

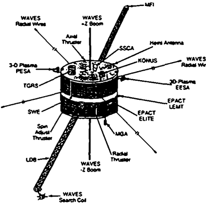

Figure 1.7: Configuration of the WIND spacecraft [*Ogilvie and Parks*, 1994].

Instrument	Description	PI	Institute
Magnetic field (MFI)	DC Mag. field	R. Lepping	NASA/GSFC
Radio and plasma wave Experiment (WAVES)	AC EM fields 8 Hz-16 MHz	J. Bougeret	Obs. de Paris
Solar Wind Experiment (SWE)	Mass, energy, direction of low energy ions and electrons, 7 eV-22 keV	K. Ogilvie	NASA/GSFC
3-D Plasma (3D Plasma)	Distribution and Energy of ions and electrons 3 eV-30 keV, 20 keV-11 MeV	R. Lin	U.C. Berkeley
Energetic Particles: Acceleration, Composition (EPACT)	Mass, energy, direction of ions, 0.2 - 500 MeV	T.von Rosenvinge	
Solar wind/mass Superthermal ion composition	Mass, energy, direction of ions, 0.5 - 500 MeV	G. Gloeckler	U. of Maryland
Transient Gamma ray spectrometer (TGRS)	High spectral resolution gamma-ray detector 15 keV-10 MeV	B. Teegarden	NASA/GSFC
KONUS (Russian Instrument)	High-time resolution gamma-ray detector	E. Mazels	IOFFE Russia

Table 1.4: WIND scientific investigations [*Ogilvie and Parks*, 1996].

on 1 November 1994 [cf. *Ogilvie and Parks*, 1996]. Therefore, we can make some simultaneous observations on the Near-tail orbit from fall of 1994.

WIND carries eight different experiments, six of which are designed to measure particles from a few eV to hundreds of MeV, and electric and magnetic fields from DC to tens of MHz. Table 1.4 lists the WIND instruments and summarizes their capabilities. In Chapter 2, 3 and 5, we use part of data sets obtained from the MFI (magnetic field) [*Lepping et al.*, 1995], the WAVES (radio and plasma waves) [*Bougeret et al.*, 1995], and the SWE (particles) [*Ogilvie et al.*, 1995] to compare our GEOTAIL data with the data observed in the solar wind.

The primary objective of WIND is to obtain information on the behavior of particles and fields in the solar wind. Figure 1.8 shows the trajectory of WIND during the first year of operation in the GSE coordinates.

1.6.2 Indices for geomagnetic activities

In the present study, we use Kp index and AKR index as indices of geomagnetic activities to compare with observed radio wave activities.

We use Kp index to know long-interval geomagnetic activities. Kp index is provided by 3-hour intervals in 10 levels from 0 to 9, and denotes the activity of geomagnetic fields or solar activity. This index is calculated with 11 magnetometers in the northern hemisphere and one in the southern hemisphere. These stations are selected in 50°–60° magnetic latitude.

On the other hand, we use AKR index to know short-interval geomagnetic activities. AKR index is defined as flux of AKR normalized at a distance of 25 R_E from the Earth in 1-minute interval [*Murata*, 1995], based on the correlation between flux of AKR and geomagnetic activity [cf. *Voots et al.*, 1977; *Kaiser and Alexander*, 1977]. Auroral-

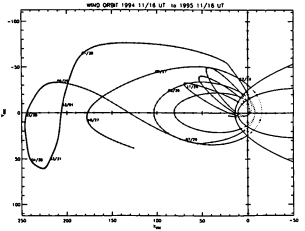

Figure 1.8: Orbit of WIND on the GSE coordinates from November 1994 to November 1995 [*Ogilvie and Parks*, 1996].

electrojet (AE) index is also able to be used as short-interval index. AE index is usually provided by both hourly and 2.5 minute values, and calculated from twelve ground-based magnetometer measurements in the auroral latitude in the northern hemisphere. Unfortunately, AE data set is not available from 1992.

1.7 Electromagnetic particle code, KEMPO

In this study, we executed some numerical experiments on the conditions of the electron foreshock, expected source region of the $2f_p$ radiation. We used the 2-1/2D electromagnetic particle code, Kyoto university's ElectroMagnetic Particle cOde (KEMPO) [*Matsumoto and Omura*, 1985], which is able to treat both electromagnetic and electrostatic wave modes simultaneously with a special time-filter technique using a multi-time-step (MTS) scheme. In KEMPO, we solve Maxwell's equation

$$\nabla \times \mathbf{B} = \mu_0 \mathbf{J} + \frac{1}{c^2}\frac{\partial \mathbf{E}}{\partial t} \quad (1.6)$$

$$\nabla \times \mathbf{E} = -\frac{\partial \mathbf{B}}{\partial t} \quad (1.7)$$

where current density $\mathbf{J}$ is computed from motion of a large number of particles under the equations of motion,

$$\frac{\partial \mathbf{v}}{\partial t} = \frac{q}{m}(\mathbf{E} + \mathbf{v} \times \mathbf{B}) \quad (1.8)$$

$$\frac{\partial \mathbf{r}}{\partial t} = \mathbf{v} \tag{1.9}$$

where q is charge and m is mass of single particle. As an initial condition, the electric field should satisfy the electrostatic equation

$$\nabla \cdot \mathbf{E} = \frac{\rho}{\epsilon_0} \tag{1.10}$$

$$\nabla \cdot \mathbf{B} = 0 \tag{1.11}$$

where ρ is a charge density computed from the positions of particles. **E**, **B**, and **J** are defined at the spatial grid points, while **E** and **B** in the equation of motion (1.8) are interpolated from those at the neighboring grid points.

In numerical simulations in this thesis, we defined $c = 1.0$, $\epsilon_0 = 1.0$, and $\mu_0 = 1.0$, respectively.

1.8 Contribution of the present work

In Chapter 2, we investigate geometry of the terrestrial electron foreshock by remote observations of the $2f_p$ radio emission. Since, only few direct evidence for a foreshock origin of the $2f_p$ radiation, we definitely determined geometry of the source region by three methods; 'the two-spacecraft triangulation by collaboration with the WIND spacecraft', 'the statistical analysis of direction finding', and 'the statistical analysis of bifurcation phenomena associated with solar wind density jump'.

In Chapter 3, we further investigate physical conditions in the terrestrial electron foreshock by in-situ observations of the $2f_p$ radio emission, based on the results obtained in Chapter 2. We investigated global distributions of plasma waves and particles in the electron foreshock by mapping analysis, local observations on and across the IMF line tangent to the bow shock.

In Chapter 4, we further investigate physical processes in the terrestrial electron foreshock by numerical experiments to generate the $2f_p$ radio emission in the computer space. We executed numerical experiments based on the results obtained in Chapter 2 and 3, and generate electrostatic and electromagnetic waves at $2f_p$ by the electromagnetic particle code, KEMPO.

In Chapter 5, we investigate global dynamics around the plasmapause during substorm by remote observations of the continuum enhancement, short-lived enhancement of the nonthermal continuum radiation. This emission is generated at the plasmapause by electrons injected into the local midnight zone associated with substorm. We used this emission to study global processes around the plasmapause through three features; 'the source locations', 'variation of the frequency range', and 'variation of the banded frequency structure'.

In Chapter 6, we investigate the global dynamics in the auroral region by remote observations of AKR. We study the frequency of occurrence of AKR, and searched the possible dependences on the factors which affect generation and propagation conditions of AKR; 'the global magnetic disturbances', 'the longitude of the source region', and 'the angle between the geomagnetic axis and the Sun-Earth line'. Based on results of these analyses, we independently evaluated characteristics of generation conditions of AKR.

In Chapter 7, we present possibility of the techniques presented in this thesis applied for planetary explorations. For a such example, we show investigation of the Jovian radio activities associated with a first historic event, the impacts of Comet Shoemaker-Levy 9 (SL-9), by remote observations of the Jovian low frequency radiations below 1 MHz. We study perturbations in the outer magnetosphere caused by direct interactions between the comet and Jovian outer magnetosphere through activity of low frequency radio emissions. We also take account of results obtained by other ground-based and orbiting observatories, and the ULYSSES spacecraft flying in the solar system distant from the Earth.

In Chapter 8, we summarize the present studies, and present possible future space studies for development and extension of the road toward space.

Chapter 2

Remote Observations of $2f_p$ Radiation

The $2f_p$ radio emission is frequently observed around the terrestrial electron foreshock. However, only few direct evidences for a foreshock origin of the $2f_p$ radiation. In this study, we definitely determine the geometry of source region by three kinds of remote observations.

First is 'the two-spacecraft triangulation'. We combine direction-finding data from simultaneous GEOTAIL/WIND observations of $2f_p$ radio emission to provide the first 3-D source location. These observations are made when both GEOTAIL and WIND are relatively close to the electron foreshock region and to each other. For two cases presented, the $2f_p$ radio source centroid is found to be stationary and located in the upstream wing of the electron foreshock region, 10-50 R_E from the contact point. In a third case, we find the $2f_p$ source centroid to follow the motion of the electron foreshock associated with rotation of interplanetary magnetic field line.

On the other hand, GEOTAIL itself has frequently provided the remote observations of the $2f_p$ radiation from regions with a distance of 10–30 R_E from the Earth. Based on these data sets, we determine the geometry of $2f_p$ radio source by two kinds of statistical analyses. First is 'the statistical analysis of direction finding'. We show that the $2f_p$ radio source centroid is not concentrated to the contact point of interplanetary magnetic field on the bow shock. Typical location of the $2f_p$ radio source centroid is the region with a distance of 10–30 R_E from the contact point. The second is 'the statistical analysis of bifurcation phenomena associated with solar wind density jump'. We show that the source location projected on the Sun-Earth line is generally limited about 5-10 R_E on the upstream side and about 10–20 R_E on the downstream side.

These results of three kinds of analyses agree well with a model that $2f_p$ radio source is in the electron foreshock. Some disagreement points in these results are also discussed.

2.1 Introduction: Geometry of $2f_p$ radio source in the electron foreshock

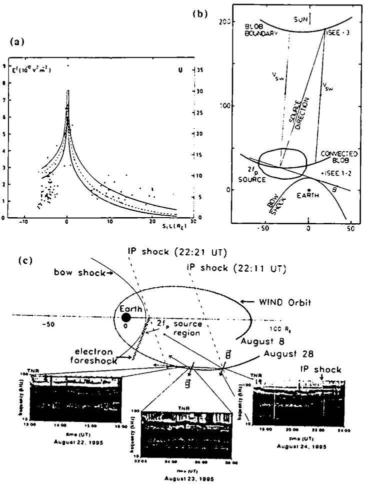

Figure 2.1: Previous results to determine the $2f_p$ radio source. (a) Flux of the $2f_p$ radiation associated with passage of ISEE-1 through the electron foreshock region. X-axis is distance from the tangential IMF line projected to the Sun-Earth line. Y-axis is flux of $2f_p$ radiation [*Lacombe et al.*, 1988]. (b) The direction finding result by ISEE 3 associated with density jump in the solar wind [*Hoang et al.*, 1981]. (c) The direction finding result by WIND associated with density jump in the solar wind [*Reiner et al.*, 1996].

The $2f_p$ radiation, at twice the solar wind electron plasma frequency, f_p, is frequently observed in whole upstream regions of the terrestrial bow shock. Early direction finding analyses indicated that the $2f_p$ radiation is originated outside the magnetosphere [*Gurnett*, 1975; *Gurnett and Frank*, 1976]. This emission is believed to be generated by intense Langmuir waves through the same mechanism as type III solar radio bursts. In the electron foreshock region just downstream of the interplanetary magnetic filed (IMF) lines tangent to the bow shock, backstreaming energetic electron beams generate strong Langmuir waves. Since strong Langmuir waves are still observed far upstream in the region with a distance of 100-200 R_E from the bow shock, the $2f_p$ radio source is also thought to extend far from the bow shock along the tangential IMF lines [cf. *Lacombe et al.*, 1988].

However, there have actually been few evidences for a foreshock origin of the $2f_p$ radiation. Figure 2.1 (a) shows the ISEE-1 measurement of $2f_p$ radiation with passage of the spacecraft through the electron foreshock region [*Lacombe et al.*, 1988]. This provides the only direct evidence for a foreshock origin of the $2f_p$ radiation. On the other hand, there are other two indirect evidences indicated in Figure 2.1 (b)-(c) [*Hoang et al.*, 1981; *Reiner et al.*, 1996]. One is that variations of frequency of the $2f_p$ radiation line associated with the density jump in the solar wind indicate the corresponding time delay by convection at the solar wind rate from the spacecraft to the electron foreshock. The other is that direction finding results are consistent with suggested $2f_p$ source in the foreshock region. These observations suggest that the $2f_p$ radio source is very large and can extend some 100 R_E along the electron foreshock [*Gurnett and Frank*, 1976; *Steinberg and Hoang*, 1986]

In this study, we definitely determine the geometry of the $2f_p$ radio source by three methods of remote observations; 'the two-spacecraft triangulation by GEOTAIL and WIND', 'the statistical analysis of direction finding', and 'the statistical analysis of bifurcation phenomena associated with density jump in the solar wind'.

2.2 GEOTAIL/WIND triangulation

In this section, we show results of the first 3-D triangulation by two spacecraft, GEOTAIL and WIND. This method can provide not only direct information of the $2f_p$ radio source location, but also real-time tracking of the $2f_p$ source centroid for finite periods of time. Therefore, this method can be used to study dynamic changes of the $2f_p$ source location in response to orientation of the interplanetary magnetic field (IMF).

2.2.1 Observational configurations

We analyze data sets simultaneously obtained by the Plasma Wave instrument (PWI) onboard the GEOTAIL spacecraft [*Matsumoto et al.*, 1994] and by the WAVES experiment onboard the WIND spacecraft [*Bougeret et al.*, 1995].

The PWI that was extensively used is Band-4 of the Sweep Frequency Analyzer (SFA), which has a frequency range of 12.5-100 kHz, a frequency resolution of 684 Hz, and a time resolution of 8 seconds. The SFA is connected to a wire dipole antenna with 50 m elements in the spacecraft spin plane that is stabilized close to the ecliptic plane.

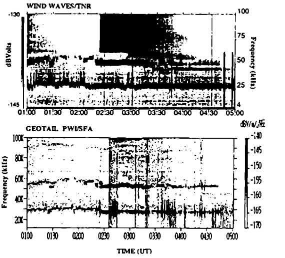

Figure 2.2: Dynamic spectra of the WIND and GEOTAIL radio data from 1-5h UT on 22 September 1995. The narrow intermittent horizontal band at about 50 kHz is the $2f_p$ radiation.

On the other hand, two WAVE instruments that were extensively used are the super-heterodyne receivers (RAD1) and the multichannel thermal noise receiver (TNR). RAD1 covers from 20-1040 kHz at 16 discrete frequencies, and TNR covers from 4-256 kHz with the bandwidth of 3 kHz, respectively. The high time and frequency resolution of the TNR makes it suitable for identifying frequency of the $2f_p$ radiation. The step-tuned RAD1 receivers are used for the direction finding by a synthesis of signals from the spin plane (S-) and spin axis (Z-) antennas [*Manning and Fainberg*, 1980]. The electric sensors consist of a long wire dipole antenna with 50 m elements in the spacecraft spin plane, and a shorter spin axis dipole with elements presently extended 4.3 m.

2.2.2 Results of the triangulation

In this section, we present the three cases of GEOTAIL/WIND triangulation of the $2f_p$ radiation. For former two cases, conditions in the solar wind are relatively stable. For the third case, IMF orientation is abruptly changes associated with passage of the density jump in the solar wind.

Case 1: in 1-5h UT on 22 September 1995

Figure 2.2 shows dynamic spectra of the radio emission in 1-5h UT on 22 September 1995 measured by the TNR on WIND and by the SFA on GEOTAIL. The frequency range on the vertical axis is 4-100 kHz for WIND and 12.5-100 kHz for GEOTAIL. The lower dark horizontal bands running at 20–30 kHz across the dynamic spectra are the quasi-thermal noise line, whose low frequency limit identifies the local plasma frequency. For this time period, the local plasma frequency at WIND and GEOTAIL remained steady at ~25 kHz. The upper dark (sometimes intermittent) band at ~50 kHz is the narrow band $2f_p$ radio emission. Although both spacecraft observed the $2f_p$ radiation from very different perspectives, the $2f_p$ radiations in both panels show much close structure in detail. This directly affirms to the wide visibility of the $2f_p$ radiation [*Steinberg and Hoang*, 1986]. The intense emission beginning at ~02:25 UT is the low-frequency extension of a type III radio burst (which saturates the WIND/TNR). The vertical noise running across the GEOTAIL dynamic spectrum, with intensification in the local plasma line, are artificial saturation effects caused by intense Langmuir waves produced by the suprathermal electrons. Presence of intense Langmuir waves indicates that GEOTAIL crossed upstream edge of the electron foreshock region.

Figure 2.3 shows the results of the simultaneous direction finding from GEOTAIL/WIND for the $2f_p$ source observed at ~50 kHz in 2–4h UT. At this time, WIND was at $(54.1, -50.5, -7.6)R_E$ and GEOTAIL was at $(18.5, -16.2, -1.6)R_E$ on the geocentric solar ecliptic (GSE) coordinates, as indicated in Figure 2.3 (a). The amplitudes of the $2f_p$ radiation simultaneously measured by GEOTAIL and WIND are shown in Figure 2.3 (b). The intensity at WIND is ~3 times smaller than at GEOTAIL. This difference may be due to the beaming of the radiation along the axis of the foreshock and/or due to the closeness of GEOTAIL to the foreshock region. The azimuth angles of the $2f_p$ emission, ϕ_{2f_p}, measured by GEOTAIL/WIND are shown in Figure 2.3 (c). The scatter in ϕ_{2f_p} is a measure of the uncertainty and arises primarily from the intensity variation of the source over the time of the measurements (3 seconds for WIND, 180 seconds for GEOTAIL). The uncertainty in ϕ_{2f_p} is significantly greater for GEOTAIL since the source intensity significantly varied over the 180 seconds which is required for each direction-finding determination.

Figure 2.3 (d) indicates the elevation angle of the $2f_p$ radiation, θ_{2f_p}, measured by WIND. Since θ_{2f_p} is slightly below the dashed line which is the direction of Earth as seen from WIND, the source lies to the north of the Earth-WIND line. A source elevation angle from GEOTAIL cannot be determined because the direction finding can only be performed with the spin-plane antenna signal on GEOTAIL. Figure 2.3 (e) shows the modulation index, α, defined by $(I_{max} - I_{min})/(I_{max} + I_{min})$. α depends on both the source elevation angle relative to the spacecraft spin axis and source angular size. The average value of 0.2 for α measured by WIND and GEOTAIL suggests a relatively large $2f_p$ source. For a source in the spin plane with $\alpha \sim 0.2$, angular radius of the source is ~70°.

The values of ϕ_{2f_p} represent the ecliptic plane projection of the direction to the source centroid. The median of azimuth angle ϕ_{2f_p} measured by GEOTAIL from 02:30 to 3:00 UT was ~114°. At the same time, the $2f_p$ source azimuth ϕ_{2f_p} mea-

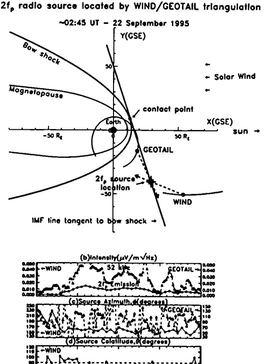

Figure 2.3: (a) WIND and GEOTAIL orbit projected on ecliptic plane. Triangulated $2f_p$ source location and field line tangent to the bow shock is also shown. (b) Observed radio intensity measured by WIND and GEOTAIL (c) Derived source azimuth angle measured from WIND and from GEOTAIL. (d) Derived source elevation angle measured from WIND. (e) Derived modulation index measured by WIND and GEOTAIL. In each panel, the solid dots and the right scale refer to the WIND measurements; the open triangles and the left scale refer to the GEOTAIL measurements.

sured by WIND was ~158° and the elevation angle θ_{2f_p} was ~76°. Therefore, the triangulated 3-D source centroid location on the GSE coordinates is found to be $(29.3, -40.5, -0.93)R_E$. Figure 2.3 (a) shows the location of source centroid obtained by GEOTAIL/WIND triangulation projected onto the ecliptic plane.

At the time of this measurement, both WIND and GEOTAIL were in the solar wind and both measured orientation of the IMF. The average IMF azimuth in the $2f_p$ source region, taking the appropriate delay to account for the convection time to the source region, was 285°. This field line makes contact with the bow shock at ~ $(9.0, 12.8, 0.0)R_E$. Figure 2.3 (a) also shows this contact point and the outer boundary of the electron foreshock region defined by orientation of the IMF. The latitude of the IMF was ~20°N. Assuming that the IMF latitude outside the orbit plane was the same, the 3-D picture of the foreshock region is these tilted parallel field lines wrapped about the paraboloid bow shock. The orientation of the bow shock shown in Figure 2.3 (a) takes into account the 4° aberration due to the orbital motion of the Earth and the additional 2° due to the solar wind flow direction measured at WIND during the time of these observations.

As indicated in Figure 2.3 (a), the triangulated $2f_p$ source centroid lies within the expected electron foreshock region. In particular, the $2f_p$ source centroid was in the upstream wing of the electron foreshock region about 50 R_E from the contact point. The above results represent the first 3-D determination of the $2f_p$ source centroid location using two spacecraft triangulation.

Case 2: in 20–24h UT on 22 September 1995

Next, we show the second GEOTAIL/WIND triangulation of $2f_p$ radiation occurred in 20–24h UT on 22 September 1995. Figure 2.4 shows the dynamic spectra of the radio emission in 20–24h UT observed by GEOTAIL and WIND. The triangulation results are shown in Figure 2.5, with the same notation as in Figure 2.3. At this time, WIND was located at $(64.4, -50.3, -8.8)R_E$ and GEOTAIL at $(14.7, 2.8, 0.8)R_E$, both in the solar wind upstream of the bow shock as indicated in Figure 2.5 (a). The results of the direction finding from 22:30 to 24:00 UT at ~80 kHz are shown in Figure 2.5 (b)-(e). Since the $2f_p$ radiation observed by WIND was weak, the results of the direction finding by WIND are not so well-defined. From Figure 2.5 (c), we find the median of azimuth angles ϕ_{2f_p} measured from WIND and GEOTAIL is 140° and 280°, respectively. Figure 2.5 (d) shows that the average elevation angle from WIND θ_{2f_p} was 86°. The modulation index α indicated in Figure 2.5 (e) is ~0.4. This indicates a somewhat smaller source region, with ~60° of angular radius.

The GEOTAIL/WIND triangulation gives the $2f_p$ radio source centroid location at $(15.78, -3.35, -4.074)R_E$ on the GSE coordinates. Figure 2.5 (a) shows the $2f_p$ radio source centroid location projected onto the ecliptic plane. During the time of these measurements, the IMF was steady with azimuth at ~290° and latitude at ~10°N. This implies an outer boundary of the electron foreshock as illustrated in Figure 2.5 (a). The triangulated $2f_p$ source location lies just inside this boundary. In this case, the $2f_p$ source centroid lies about 15 R_E from the contact point, at $(12.0, 10.0, 0.0)R_E$.

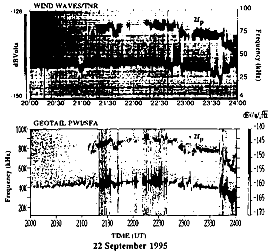

Figure 2.4: Dynamic spectrum of the WIND and GEOTAIL radio data in 20–24h UT on 22 September 1995.

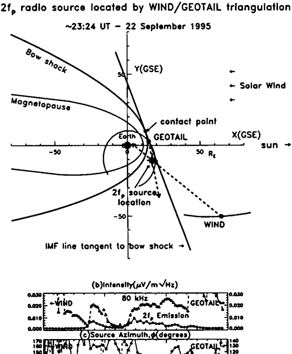

Figure 2.5: GEOTAIL/WIND triangulation results for the $2f_p$ radiation from 22:30 to 24:00 UT on 22 September 1995.

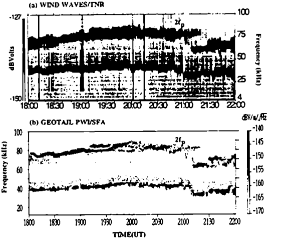

30 July 1995

Figure 2.6: Dynamic spectrum of the WIND (a) and GEOTAIL (b) radio data in 18–22h UT on 30 July 1995.

Case 3: in 18–22h UT on 30 July 1995

As a final example, we present a $2f_p$ event on 30 July 1995 observed when the electron foreshock moved during the period of the observation associated with rotation of the IMF in the solar wind. Figure 2.6 shows the dynamic spectra of the radio emission in 18–22h UT. At this time, WIND was at $(41.6, 32.0, -3.0)R_E$ and GEOTAIL was at $(22.6, 5.9, -1.4)R_E$. The IMF direction rotated rapidly from 270° at ~20:45 UT to 225° at ~21:05 UT, as observed from both GEOTAIL and WIND. Correspondingly, there was a sudden change in the $2f_p$ azimuth at WIND from 140° at 20:45 UT to 200° at 21:10 UT and a change in that at GEOTAIL from 100° at 20:45 UT to 40° at 21:20 UT, as shown in Figure 2.7 (c).

The results of the triangulation at 20:45, 21:00, 21:10 and 21:20 UT are shown in Figure 2.7 (a). The orientation of the IMF tangent to the bow shock at these times is indicated by the various lines. The directions of the $2f_p$ radiation from GEOTAIL/WIND are indicated by the dotted lines. The triangulated $2f_p$ source locations are indicated by the stars. It is clear in Figure 2.7 (a) that the $2f_p$ source is following the rotation of the IMF in such way as to maintain its centroid in the electron foreshock region. On the other hand, this $2f_p$ event also illustrates the motion of the electron foreshock. For example, distance of source centroid from the contact point varies associated with passage of the density jump; ~50 R_E at 20:45 UT, then decreases to ~30 R_E, and finally increases to ~85 R_E.

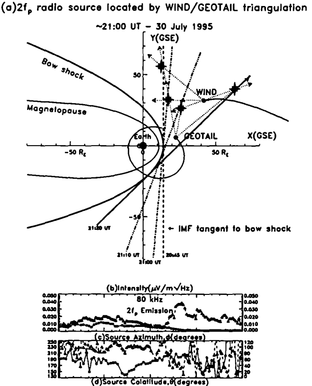

Figure 2.7: GEOTAIL/WIND triangulation results for the $2f_p$ emission from 20:00 to 22:00 UT on 30 July 1995. The deduced orientation of the electron foreshock at 20:45, 21:00, 21:10 and 21:20 UT are shown by the dashed, dash-dot, dash-dot-dot-dot and solid lines, respectively. The GEOTAIL/WIND triangulation is indicated by the dotted lines and the $2f_p$ source locations by the stars.

2.3 Statistical analysis of remote observations

In previous section, we show by the triangulation of GEOTAIL and WIND that the $2f_p$ source locates in the electron foreshock and follows the motion of the electron foreshock associated with rotation of the IMF. However, we should note that the GEOTAIL/WIND triangulation frequently fails to locate the source, or locates far inside or outside the electron foreshock. Fortunately, the $2f_p$ radio emission is generally observed by GEOTAIL in all the upstream region of the bow shock in a distance of 10–30 R_E from the Earth. In order to confirm results of the triangulation, we analyze GEOTAIL data sets by two kinds of statistical methods; 'the statistical analysis of direction finding', and 'the statistical analysis of bifurcation phenomena associated with the density jump in the solar wind'.

Plasma wave data is obtained by the Sweep Frequency Analyzer (SFA), a part of the Plasma Wave Instrument (PWI) aboard GEOTAIL [*Matsumoto et al.*, 1992]. Simultaneous values of the IMF orientation and velocity of the solar wind are taken from GEOTAIL the Magnetic Field Measurements (MGF) [*Kokubun et al.*, 1992] and the Low Energy Particle (LEP) experiment [*Mukai et al.*, 1992] aboard GEOTAIL.

2.3.1 Statistical analysis of direction finding

On this study, we statistically analyze 21 cases of direction finding results of the $2f_p$ radiation observed from February to November 1995. Direction finding is based on spin modulation of electric field strength, and determined by standard Fourier technique [*Manning and Fainberg*, 1980]. We should mention that directions of the source region indicated by direction finding are generally scattered in GEOTAIL data. This might be caused by fast variation of $2f_p$ flux over the time of the measurements (~180 seconds), scattering of $2f_p$ radiation in the ion foreshock or at the bow shock, and/or too large apparent angular radius of the source from the location of GEOTAIL too close to the source. We select samples with a condition that variation of the source direction stays within 10° for 30 minutes. For such cases, variations of the IMF orientation stay within 10° and elevation angles of the IMF is within 30°. This means that location of expected source region on the IMF line tangent to the bow shock should be stable and close to the ecliptic plane. Such condition is suitable for direction finding by GEOTAIL whose spinning plane is close to the ecliptic plane.

Figure 2.8 shows the result of direction finding in the GSE coordinates grouped with azimuth angle of the IMF ϕ_B; (a) 60–80°, (b) 80-100°, (c) 100–120°, and (d) 120–140°. We also show whole the direction finding results normalized to $\phi_B = 120°$ in Figure 2.8 (e). In Figure 2.8, the source directions are generally close to parallel with IMF direction, even in the region close to the contact point. General crossing positions between observed source directions and the IMF lines tangent to the bow shock is at a distance of 10–30 R_E from the contact point. This indicates that the source region of the $2f_p$ radiation is not concentrated around the contact point. We also find that features of the source directions indicate symmetric extension of the source region along the tangential IMF line in upstream and downstream wing.

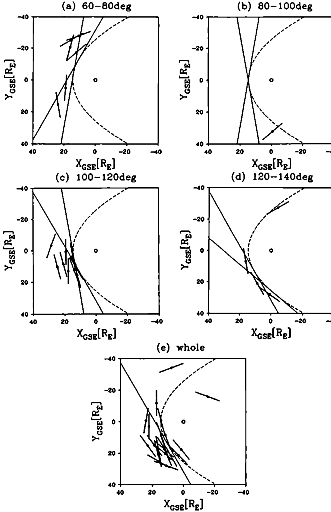

Figure 2.8: Direction finding results grouped to azimuth angle of the IMF, ϕ_B. (a) 60°-80°; (b) 80°-100°; (c) 100°-120°; (d) 120°-140°; (e) normalized to ϕ_B = 120°. Circles indicate satellite locations. Thick lines indicate $2f_p$ radio source directions. Thin lines indicate tangential IMF lines.

2.3.2 Statistical analysis of bifurcation

Bifurcation phenomena of the $2f_p$ radiation are sometimes observed associated with the density jump in the solar wind [*Lacombe et al.*, 1988; *Reiner et al.*, 1996]. Figure 2.9 (a) shows an example at 22:20–22:45 UT on 24 August 1995. Such phenomena are caused by progressive variation of the plasma frequency in the extended source region. For example, Figure 2.9 (a) shows that the new $2f_p$ radiation at 105-110 kHz appears at 22:22 UT and old $2f_p$ radiation at 85 kHz vanishes at 22:42 UT. Figure 2.9 (b) shows a schematic view of this case. We can estimate the former and the latter indicate the times when the density jump reached at the most upstream edge of the upstream wing and passed at the most downstream edge of the downstream wing, respectively. Therefore, from appearance and vanishing times of the $2f_p$ radiations in the bifurcation phenomena, we can define locations of the edges of the upstream/downstream wings projected to the Sun-Earth line, X_{up} and X_{down} by

$$\begin{aligned} X_{up} &= X_{s/c} + (T_{up} - T_{s/c})v_{sw} \\ X_{down} &= X_{s/c} + (T_{down} - T_{s/c})v_{sw} \end{aligned} \quad (2.1)$$

where $X_{s/c}$ and $T_{s/c}$ are location and time when the density jump passed at GEOTAIL, T_{up} is the appearance time of new $2f_p$ line, T_{down} is the vanishing time of old $2f_p$ line, and v_{sw} is the solar wind velocity along the Sun-Earth line, respectively. For simplification, we assume that normal of the density jump in each case is parallel to the Sun-Earth line in each analysis. For this study, we find 32 cases of bifurcation phenomena from February to October 1995. We select samples with conditions that variations of the IMF orientation stay within 10°, and elevation angles of the IMF is within 30°.

Figure 2.9 (c) shows the observed upstream/downstream wing of the source region projected along the Sun-Earth line. Since the bow shock is roughly rotational symmetry about the solar wind flow line, we superpose the results in the cylindrical X_{GSE}-$\sqrt{Y_{GSE}^2 + Z_{GSE}^2}$ coordinates. Circle indicates the contact point of the tangential IMF line estimated at each event. Bars indicate extension of the $2f_p$ source region projected on the Sun-Earth line, from X_{up} to X_{down}. In Figure 2.9 (c), we find that typical extension of the upstream wing projected on the Sun-Earth line is up to 5-10 R_E from the contact point. Such projected extension seems to be inversely correlated with the angle between the Sun-Earth line and the IMF direction as expected. Therefore, real extension of the upstream wing estimated from this analysis is larger. On the other hand, extension of the downstream wing projected on the Sun-Earth line is 10-20 R_E. Such asymmetry of extensions of the upstream and downstream wings is not consistent with symmetric extension indicated in the statistical direction finding results. However, Figure 2.9 (d) shows the same result. Figure 2.9 (d) shows real extension of the upstream/downstream wing of the $2f_p$ radio source suggested by the all cases indicated in Figure 2.9 (c), plotted in the cylindrical X_{GSE}-$\sqrt{Y_{GSE}^2 + Z_{GSE}^2}$ coordinates. In Figure 2.9 (d), we find that typical extension of the upstream wing is 5-40 R_E from the contact point, while that of the downstream wing is 20–80 R_E, which is twice of that of the upstream wing.

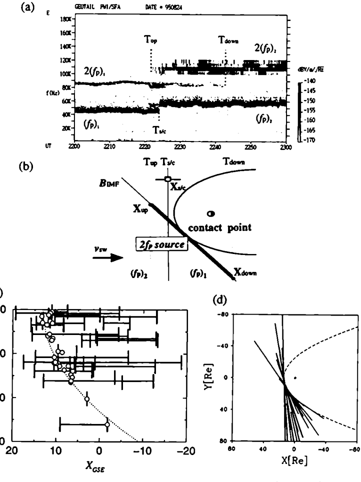

Figure 2.9: Edge of the upstream/downstream wing of the $2f_p$ radio source determined by analysis of 'bifurcation'. (a) An example of bifurcation observed at ~22:30 UT on 24 August 1996. (b) A schematic view of bifurcation. (c) The $2f_p$ radio source projected on the Sun-Earth line in X_{GSE}-$\sqrt{(Y_{GSE}^2 + Z_{GSE}^2)}$ coordinates. Circles indicate the expected contact points. (d) The $2f_p$ radio source projected on X_{GSE}-$\sqrt{(Y_{GSE}^2 + Z_{GSE}^2)}$ coordinates.

2.4 Discussions

First, we evaluate GEOTAIL/WIND triangulation, which illustrate the advantage of making simultaneous spacecraft observations. Two events are chosen when the IMF direction remained relatively steady during the period of observation. In these cases, the $2f_p$ source location remained constant on the electron foreshock region over the time of the measurements. We also presented the result of the triangulation for a $2f_p$ event observed when the IMF displayed a systematic rotation. We showed that the triangulated $2f_p$ source centroid followed the motion of the electron foreshock region.

We should mention that often the GEOTAIL/WIND triangulation either fails to locate the source or locates the source far inside or outside the electron foreshock in analyzing many examples of $2f_p$ radiation. There are a number of possible explanations for this failure. Depending on the position of GEOTAIL/WIND relative to the source, they may observe very large $2f_p$ source from very different perspectives. Therefore, proximity effects can alter the true centroid of the source region. GEOTAIL which by nature of its orbit is always very close to the $2f_p$ source region is particularly susceptible to these proximity effects. Regions of the radio source closer to GEOTAIL can have a much greater influence on the direction finding than the regions farther from GEOTAIL. WIND is less effected by these proximity effects because WIND stays generally farther from the source region. On the other hand, the $2f_p$ radio source centroid in all cases presented here is found to lie in the upstream wing of the electron foreshock. It seems to be because all cases presented here are observed in the regions close to upstream wing of the electron foreshock. In such situation, both satellites are easy to be affected by closer source in the upstream wing. In addition, the bow shock can interrupt the propagation of $2f_p$ radiation from the downstream wing.

We also define the geometry of the $2f_p$ radio source by two statistical methods using GEOTAIL PWI data sets: statistical analysis of direction finding, and statistical analysis of bifurcation phenomena associated with density jump in the solar wind. Statistical analysis of direction finding shows apparent locations of the $2f_p$ radio source centroid from GEOTAIL. We find that the observed source directions generally seem to be close to parallel with IMF direction. This result indicates that the source region of the $2f_p$ radiation is not concentrated around the contact point. This can be explained by a model that a sharp electron beam is not formed through the time-of-flight effect at the region close to the contact point because of a shortage of flight time. Other possible explanations are sharp beaming along the tangential IMF. Although such beaming was not supported by previous observations [cf. *Lacombe et al.*, 1988], we need to verify in future studies. We also indicated that distribution of apparent locations of the source centroid on the tangential IMF line is generally symmetric in the upstream and downstream wings, at a distance of 10–30 R_E from the contact point. On the other hand, statistical analysis of bifurcation phenomena shows locations of the upstream/downstream edges of the $2f_p$ radio source. We find that extension of the source projected on the Sun-Earth line seems asymmetry. Distances of the edges from the contact point is about 5–10 R_E in the upstream wing and about 10–20 R_E in the downstream wing. Both analyses show that typical extension of $2f_p$ radio source is not so long, below 100 R_E, which is shorter than values expected by previous obser-

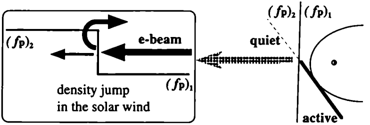

Figure 2.10: A schematic model of possible electron beam destruction at density jump in the solar wind associated with bifurcation phenomena.

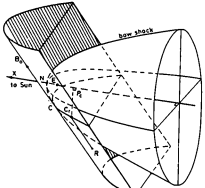

Figure 2.11: The 3-D picture of the foreshock region [*Lacombe et al.*, 1988].

vations of Langmuir waves in far upstream region. This indicates the typical length of consumption of free energy in the electron beams accelerated at the contact point.

Limitation of the $2f_p$ source extension from the contact point should be caused by the consumption of free energy of electron beams in the long trip from the contact point. Therefore, we expected symmetric extension as indicated in the statistical analysis of direction finding. There are two possible explanations for short extension of the upstream wing determined from bifurcation phenomena. One is destruction of electron beams on the tangential IMF line associated with crossing at the density jump, which is indicated in Figure 2.10. On this point of view, the $2f_p$ radiation is hard to be generated beyond upstream of the density jump, and edge of upstream wing should be under-estimated. The other is wide distribution of the contact points of tilted parallel field lines wrapped about the paraboloid bow shock, as indicated in Figure 2.11. Since the contact points on the bow shock also distribute more downstream than that of the

IMF line on GEOTAIL, the $2f_p$ radiation source should also distribute far downstream region. In order to confirm this model, we need to investigate efficiency of electron beam generation correlated with location of the contact points.

This hypothesis seems to be tested by the triangulation of the bifurcation phenomena. One of such cases is already shown in Figure 2.4 and Figure 2.7. In this case, $X_{s/c}$, $T_{s/c}$, T_{up}, T_{down}, and v_{sw} is 22.6 R_E, 21:08, 21:09, 21:22, and 320 km/s. Therefore, we can define approximate locations of $2f_p$ radio source edges, $X_{up} = 23$ R_E at 21:09 and $X_{down} = -19$ R_E at 21:22, respectively. Although Figure 2.7 can not give clear evidence to distinguish both effects, such investigations will provide beam destruction and/or 3-D views of the electron foreshock.

2.5 Conclusion

In this chapter, we investigated the geometry of $2f_p$ radio source by remote observation techniques. Our current conclusion is as follows:

(1) The $2f_p$ radio source lies in the electron foreshock. When the IMF displays a systematic rotation, $2f_p$ source follows the motion of the electron foreshock. These results support the idea that $2f_p$ radiation is generated from strong Langmuir waves in the electron foreshock.

(2) The region close to the contact point is not bright source of the $2f_p$ radiation. This should be due to lack of a sharp electron beam in the region close to the contact point, because of a shortage of flight time. Other possible explanations are beaming of $2f_p$ radiation parallel to the tangential IMF.

(3) The distance of source region from the Earth is below 100 R_E, which is shorter than expected values by previous observations. This indicates the typical length of consumption of free energy in the electron beams accelerated at the contact point.

We need to confirm these suggestions by extensive in-situ observations of the $2f_p$ radiation source by in-situ observation to confirm these suggestions.

Chapter 3

In-situ Observations of $2f_p$ radiation

We analyze the in-situ observations around the electron foreshock in order to investigate physical conditions in the $2f_p$ radio source.

First, we show the spatial distributions of plasma waves and energetic particles in the foreshock region. We can roughly divide the foreshock region into three parts; 'the leading edge of the electron foreshock' with the enhancement of energetic electrons above 1 keV, strong Langmuir wave, and electrostatic wave below 1 kHz; 'the deep region of the electron foreshock' with the enhancement of moderate electrons below 1 keV, weak Langmuir wave, and electromagnetic wave below 100 Hz; 'the ion foreshock' with ion beams and sporadic electrostatic wave at several kHz. We find that the centroid of the $2f_p$ radio source is superposed on the electron foreshock, so that the $2f_p$ radio source should be living with intense Langmuir waves generated by energetic electron beams and without sporadic Doppler-shifted ion acoustic waves at several kHz. The source centroid is located at the region with the distance of about 5–40 R_E from the contact point, and not concentrated around the bow shock. This suggests that sharp electron beams are formed in a region distant from the bow shock through time-of-flight effect after the initial acceleration at the contact point. We also confirm that the power flux of the $2f_p$ radiation is positively correlated with solar wind kinetic flow. Since the population of energetic electrons is also correlated in the same manner, the power flux of the $2f_p$ radiation should be positively correlated with the strength of energetic electron beams. On the other hand, we also find that the $2f_p$ radiation is more intense on the IMF line tangent to the nose portion of the bow shock. Since the strength of Langmuir wave and the population of energetic electrons also increase in the same manner, the population of the electron beams should be more enhanced on the IMF line tangent to the nose portion. These results suggest that $2f_p$ radiation can work as a remote sensing probe to study various plasma activities in the electron foreshock.

Secondly, we show direct observations of plasma waves and energetic particles along and across the tangential IMF line. Although we can not find clear evolution of plasma waves and electron beams along the tangential IMF line, we find that density of the quasi-beam component shows faster decrease than its kinetic energy on the way from the contact point. This suggests beam formation process by the decrease of dense low-energy components through the time-of-flight mechanism. This model agrees well with results of the remote observations and the spatial distributions of plasma waves and energetic particles. On the other hand, on the pass across the leading edge of the electron foreshock where Langmuir waves and energetic electrons are dramatically enhanced, we also find clear enhancement in electric field at $2f_p$ and below 1 kHz in both SFA and MCA. Although we are afraid artificial enhancement in the SFA/MCA by saturation from intense Langmuir wave and in the MCA by cross-talk between neighboring channels, this might suggest enhancement of electrostatic waves at $2f_p$ and below 1 kHz associated with nonlinear decay of strong Langmuir wave. Typical ratio of 'local' wave at $2f_p$ to Langmuir wave is below −40 dB, while that of 'local' wave below 1 kHz to Langmuir wave is below −10 dB. These values give a strong limitation when we evaluate emission mechanisms of the $2f_p$ radiation.

3.1 Introduction: Physical conditions in $2f_p$ radio source

In Chapter 2, we present by remote observations that the electron foreshock is possibly superposed to the $2f_p$ radio source. In the electron foreshock, strong Langmuir waves are generated by backstreaming energetic electrons at the electron plasma frequency, f_p [*Anderson et al.*, 1979; *Anderson*, 1981; *Anderson et al.*, 1981]. Electromagnetic $2f_p$ wave is believed to be generated by these Langmuir waves through a nonlinear direct-conversion or mode-conversion process [*Filbert and Kellogg*, 1979; *Cairns and Melrose*, 1985; *Cairns*, 1988; *Yoon et al.*, 1994]. Strong Langmuir wave is still observed in the region with a distance beyond 100 R_E from the bow shock along the interplanetary magnetic field (IMF) lines tangent to the bow shock surface [cf. *Greenstadt et al.*, 1995]. Therefore, the $2f_p$ radio source have been also expected to extend far from bow shock [cf. *Lacombe et al.*, 1988].

Fortunately, GEOTAIL have frequently passed the electron foreshock with a distance of 10-30 R_E from the Earth on the Near-Tail orbit. In this study, we use data sets of plasma waves, energetic particles, and local IMF orientation obtained by the Plasma Wave Instrument (PWI) [*Matsumoto et al.*, 1992], the Low Energy Particle Experiment (LEP) [*Mukai et al.*, 1992], and the Magnetic Field Measurements (MGF) [*Kokubun et al.*, 1992] aboard the GEOTAIL spacecraft, respectively, and extensively investigate physical conditions in the electron foreshock, the most possible source of $2f_p$ radiation, by in-situ observations. First, we show spatial distribution of plasma waves and energetic particles in the foreshock region. Secondly, we show local observation of plasma waves and energetic particles along and across the tangential IMF line.

General configuration of geometry in the foreshock region is indicated in Figure 3.1. Observed waves and particles in the foreshock region strongly depend on such geometry [*Filbert and Kellogg*, 1979; *Anderson et al.*, 1979]. In this chapter, we introduce two parameters, *Diff* and *Dist*, for foreshock geometry description; *Diff* is the distance of the spacecraft from the tangential IMF line projected on the Sun–Earth line. *Dist* is the distance of the spacecraft from the contact point of IMF line tangent to the bow shock surface projected on the tangential IMF line [cf. *Filbert and Kellogg*, 1979; *Etcheto and

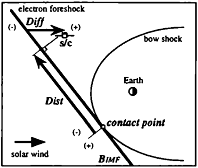

Figure 3.1: Geometry of the terrestrial foreshock [cf. *Filbert and Kellogg*, 1979; *Etcheto and Faucheux*, 1984].

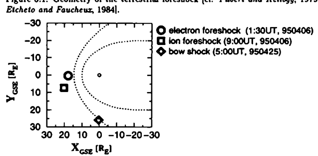

Figure 3.2: Observed locations of the electron foreshock (0.5-2.5h UT, 6 April 1995), the ion foreshock (8-10h UT, 6 April 1995), and the bow shock (4-6h UT, 25 April 1995) on the GSE coordinates. Dotted lines are nominal locations of the bow shock and the magnetopause.

Faucheux, 1984]. Positive directions of both *Diff* and *Dist* are defined as anti-sunward.

3.2 Typical plasma wave spectra in the foreshock

Previous observations have shown that the foreshock region can be divided into the electron and ion foreshocks depending on distance from the IMF line tangent to the bow shock, based on acceleration at the bow shock (magnetic reflection and upstream leakage) and propagation in the foreshock (time-of-flight process) [*Greenstadt and Fredricks*, 1979; *Gurnett*, 1985; *Fitzenreiter*, 1995]. In this section, we show typical plasma wave spectra observed at the electron foreshock, the ion foreshock, and the bow shock. Figure 3.2 shows observed locations on the Geocentric Solar Ecliptic (GSE) coordinates.

Figure 3.3 shows plasma wave spectra around the electron foreshock observed in

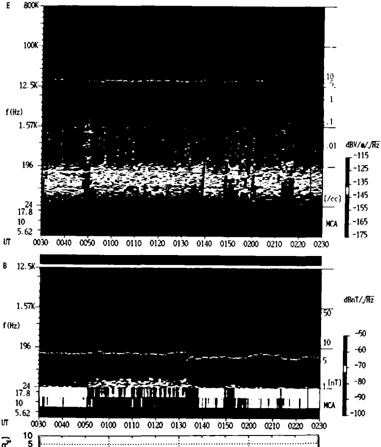

Figure 3.3: Plasma wave spectra around the electron foreshock observed by the SFA and MCA in 0:30-2:30 UT on 6 April 1995. White lines indicate electron gyrofrequency, f_g. Bottom column is *Diff* at GEOTAIL.

0:30–2:30 UT on 6 April 1995. Electron plasma frequency, electron gyrofrequency, and ion plasma frequency were ~26 kHz, ~170 Hz, and ~600 Hz, respectively. Vertical lines associated with intense Langmuir waves are artificial caused by saturation of the preamplifier of the SFA. Bottom column indicates *Diff* at GEOTAIL determined by local IMF orientation and nominal bow shock location. Before 0:48 UT, GEOTAIL generally stayed in the solar wind at upstream of the IMF line tangent to the bow shock surface, and only observed low plasma wave activities except weak quasi-thermal noise line at frequencies just above the local electron plasma frequency. At 0:48 UT, accompanied with increase of *Diff*, GEOTAIL entered the electron foreshock at just downstream of the tangential IMF line, and stayed in the electron foreshock till 1:38 UT. After that, GEOTAIL repeatedly went across the tangential IMF lines associated with variation of the IMF orientation. Figure 3.4 summarizes plasma wave activities at the some specific frequency ranges observed by the SFA (dots) with 8-second interval above 1.7 kHz and 64-second interval below 1.7 kHz, and the MCA (lines) with 0.5-second interval, respectively. Data observed by the SFA and MCA little differ because the SFA has lower background level but is easy to saturate by intense Langmuir wave, while the MCA has wider dynamic range but larger background level. Figure 3.4 suggests that the electron foreshock can be divided into two parts; leading edge and deep region. At the leading edge, intense Langmuir wave was observed in 0:48–0:52, 1:36–1:39, 1:47–1:52, and 2:12–2:17 UT, associated with thin electron beams above 1 keV [cf. *Anderson et al.*, 1979; *Anderson et al*, 1981]. At this region, we also find enhancement of electric field at $2f_p$ and below 1 kHz. Although these waves might be artificial caused by saturation and the like [cf. *Lacombe et al.*, 1988], we can suggest that the electric field below 1 kHz might indicate enhancement of ion acoustic wave associated with backscattering of Langmuir wave [cf. *Muschietti and Dum*, 1991], and the electric field at $2f_p$ might indicate enhancement of electrostatic $2f_p$ wave [cf. *Klimas*, 1983]. On the other hand, in the deep region, weak Langmuir wave accompanied with weak extended component to several kHz was observed in 0:55–1:35 UT, associated with hot electron tail below 1 keV [*Gurnett*, 1985]. In this region, we also find enhancement of magnetic field below 100 Hz. Such enhancement might indicate that of whistler wave [*Anderson et al.*, 1981] or lower hybrid wave [*Thejappa et al.*, 1995]. Based on correlation between *Diff* at GEOTAIL and plasma wave features, we can estimate that thickness of the leading edge is less than 1 R_E and that of the deep region is less than 3–4 R_E, respectively.

Figure 3.5 shows plasma wave spectra around the ion foreshock observed in 8–10h UT on 6 April 1995. Electron plasma frequency, electron gyrofrequency, and ion plasma frequency were ~28 kHz, ~140–180 Hz, and ~600 Hz, respectively. Figure 3.6 summarizes plasma wave activities at the some specific frequency ranges observed by the SFA (dots) and the MCA (lines). In 8:10–8:40 and 9:35–10:00 UT, *Diff* of GEOTAIL abruptly increase associated with rotation of IMF, and GEOTAIL entered the ion foreshock at far downstream of the tangential IMF line. In the ion foreshock, Langmuir wave, $2f_p$ wave, electric field below 1 kHz and magnetic field below 100 Hz were less active than those in the electron foreshock. On the other hand, sporadic electrostatic wave was found at several kHz, between electron plasma frequency and ion plasma frequency. Such wave is thought to be Doppler-shifted ion acoustic wave associated

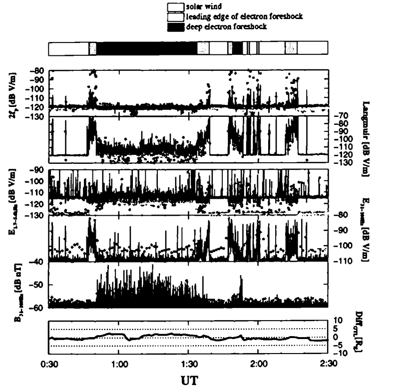

Figure 3.4: Plasma wave activities around the electron foreshock in 0:30–2:30 UT on 6 April 1995. Top column is GEOTAIL location. Middle columns are electric field at $2f_p$ at ~52 kHz, electric field at f_p at ~26 kHz, electric field in 1.7–5.6 kHz, electric field in 31–100 Hz, and magnetic field in 31–100 Hz. Dots and lines are data observed by the SFA (8-second interval above 1.7 kHz; 64-second interval below 1.7 kHz) and by the MCA (0.5-second interval). Bottom column is *Diff* at GEOTAIL.

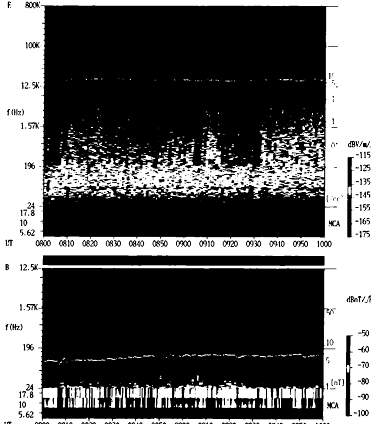

Figure 3.5: Plasma wave spectra around the ion foreshock observed by the SFA and MCA in 8–10h UT on 6 April 1995. White lines indicate electron gyrofrequency, f_g. Bottom column is *Diff* at GEOTAIL.

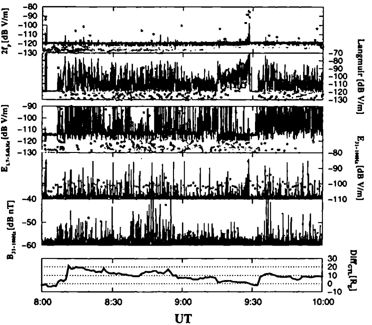

Figure 3.6: Plasma wave activities around the ion foreshock in 8-10h UT on 6 April 1995. From the top column, electric field at $2f_p$ at ~56 kHz, electric field at f_p at ~28 kHz, electric field in 1.7-5.6 kHz, electric field in 31-100 Hz, and magnetic field in 31-100 Hz are indicated. Dots and lines are data observed by the SFA (8-second interval above 1.7 kHz; 64-second interval below 1.7 kHz) and by the MCA (0.5-second interval). Bottom column is *Diff* at GEOTAIL.

with backstreaming ion beams from the bow shock [*Anderson et al.*, 1981]. General feature of this wave is similar to the narrow-band electrostatic noise (NEN) observed in the magnetosheath behind the bow shock [*Kojima et al.*, 1996], while its emission mode and mechanism are still in investigation. The Doppler-shifted ion acoustic wave have been thought to be responsible to generation of electromagnetic waves at $2f_p/f_p$ through decay of intense Langmuir wave [cf. *Anderson et al.*, 1981]. However, our observation suggests that the Doppler-shifted ion acoustic wave is only observed in the ion foreshock and at least independent of any enhancement of plasma waves at $2f_p$.

Figure 3.7 shows plasma wave spectra around the bow shock observed in 4-6h UT on 25 April 1995. GEOTAIL entered the region behind the bow shock in 4:00-4:16, 5:08-5:18, and 5:40-5:49 UT. At the bow shock crossings, we observed projection of density and magnetic field strength; electron plasma frequency and gyrofrequency increased to ~40 kHz and ~200 Hz just behind the bow shock from ~22 kHz and ~100 Hz observed in the upstream region, respectively. Figure 3.6 summarizes plasma wave activities at the some specific frequency ranges observed by the SFA (dots) and the MCA (solid lines). Just behind the bow shock, intense electrostatic and electromagnetic waves are observed accompanied with large number of energetic particles [cf. *Gurnett*, 1985]. In contrast, we also find that activity of Langmuir wave is low at the bow shock, because energetic electrons at this region are too dense or thermalized to generate strong beam-plasma instabilities.

3.3 Distributions of waves and particles

All of proposed emission mechanisms of $2f_p$ radiation suggest that its emissivity should be positively correlated with activity of local Langmuir wave. Therefore, we can assume that the most possible location of the $2f_p$ radio source is the leading edge of the electron foreshock. However, we should still pay attention to the deep region of the electron foreshock that is broader. In this section, we investigate distribution of plasma waves and energetic particles to study physical conditions in the foreshock region. Such study was first presented as the mapping of Langmuir wave by ISEE 3 [*Greenstadt et al.*, 1995]. Figure 3.9 shows mappings of the terrestrial foreshock, using normalized foreshock coordinates on a common diagram of the nominal IMF at 135° stream angle and the nominal shock. Because of relative small population of sample points, normalized plane is divided into 20×20 R_E squares overlapping one another on a 10×10 R_E grid. These data suggest that the region with high amplitude Langmuir wave extends at least to about 100 R_E from the contact point of IMF line tangent to the bow shock surface.

Compared with the study of ISEE 3, GEOTAIL observation has two advantages: The first is that we have larger sample points around the foreshock on the Near-Tail orbit at a distance of 10-30 R_E from the Earth (Figure 3.10). The second is that we can evaluate flux of $2f_p$ radiation because the PWI/SFA has better frequency resolution than the radio experiment of ISEE 3. Based on such advantages, we investigate spatial distributions of Langmuir wave at f_p (~20-50 kHz), the $2f_p$ radiation at $2f_p$(~40-100 kHz), electric field in 1.6-7.0 kHz, electric field in 31-100 Hz, magnetic field in 31-100 Hz, energetic electrons in 0.45-9.3 keV, and energetic ions in 12-25 keV, in more

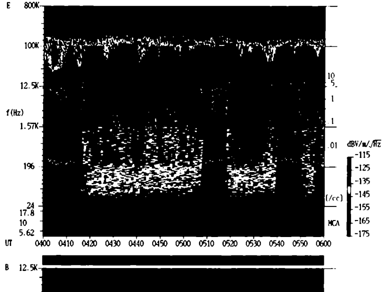

Figure 3.7: Plasma wave spectra around the bow shock observed by the SFA and MCA in 4–6h UT on 25 April 1995. White lines indicate electron gyrofrequency, f_g.

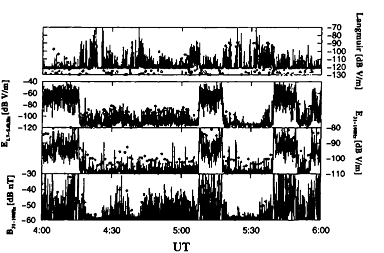

Figure 3.8: Plasma wave activities around the bow shock in 4-6h UT on 25 April 1995. From the top column, electric field at f_p, electric field in 1.7-5.6 kHz, electric field in 31-100 Hz, and magnetic field in 31-100 Hz are indicated. Dots and lines are data observed by the SFA (8-second interval above 1.7 kHz; 64-second interval below 1.7 kHz) and by the MCA (0.5-second interval).

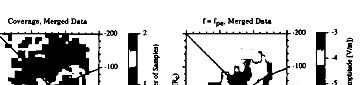

Figure 3.9: The ISEE 3 mappings of the terrestrial foreshock observed from September and December 1983: Shock diagrams are aberrate by −4° [*Greenstadt et al.*, 1995].

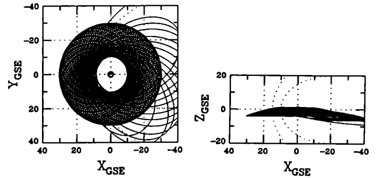

Figure 3.10: Trajectories of the GEOTAIL spacecraft on the Near-Tail orbit in the GSE coordinates, from November 1994 to April 1996. Left is projected on X-Y plane. Right is projected on X-Z plane.

detailed spatial resolution.

3.3.1 Analyzed data sets

In this analysis, we use the PWI to get strength of plasma waves and local plasma density, the LEP to get population of energetic particles and solar wind velocity, and the MGF to get orientation of IMF, respectively. We make 1-minute (~8 spins) average data sets of the SFA, LEP, and MGF from November 1994 to April 1996.

We use the SFA to examine intensity of plasma waves. Strength of Langmuir wave is automatically traced by peak searching within ±10 kHz from the electron plasma frequency estimated from local proton density observed by the LEP. On the other hand, the case of $2f_p$ radiation is more complicated because $2f_p$ radiation is not generated in the vicinity of GEOTAIL and it is necessary to estimate f_p in the distant radio source for automatic tracing. For simplification, we make two assumptions; one is that density profile in the solar wind is plane-symmetric with normal parallel to the Sun-Earth line, and the other is that $2f_p$ radio source lies around nose of the bow shock at $X_{GSE} \sim +15\ R_E$. Based on these assumptions, we automatically trace $2f_p$ radiation by peak searching within ±10 kHz from twice the electron plasma frequency at the radio source, which is estimated from local proton density and solar wind velocity observed by the LEP. Since solar wind velocity is usually about 300-600 km/s, variation of density at the $2f_p$ radio source and at GEOTAIL differs within ±5 minutes. Since automatic tracing of $2f_p$ radiation by this method fails when rapid and large density fluctuation passed, we reject such unusual cases.

On the other hand, we use the LEP to examine population of energetic particles. In order to evaluate the energetic particles going along the magnetic field line, we use distribution function of particles observed at the channels whose angle is within ±30 degree from orientation of local IMF.

In this analysis, we have to remove data contaminated by saturation effects or other natural radiations. When the SFA saturates by intense Langmuir wave, false waves are enhanced at harmonics of f_p. Therefore, we reject flux of $2f_p$ radiation observed when flux at $3f_p$ exceeds -155 dB $\mathrm{Vm^{-1}Hz^{-1/2}}$. This method is also effective to reject contamination from other natural broadband radiations such as auroral kilometric radiation, nonthermal continuum radiation and solar type III radio burst. Although among such 'saturated' artificial waves there might be local excitation of $2f_p$ waves generated by intense Langmuir wave, we do not pick them up by the present method.

We also have to get precise geometry of the foreshock region. The foreshock geometry is determined by orientation of IMF and location of the bow shock. Location of the bow shock indicated in Figure 3.1 is a rotational symmetric paraboloid about the Sun-Earth line, fitted to 188 satellite crossings of the bow shock [*Fairfield*, 1971]. The approximate location of the bow shock, $(X_{\mathrm{BS}}, Y_{\mathrm{BS}}, Z_{\mathrm{BS}})$, on the GSE coordinates is

$$\frac{X_{\mathrm{BS}}}{a_s} = 1 - \frac{Y_{\mathrm{BS}}^2 + Z_{\mathrm{BS}}^2}{b_s^2} \tag{3.1}$$

where the parameter a_s (= 14.6 R_E) and b_s (= 25.6 R_E) are standoff distance and relative diameter of the bow shock, respectively [cf. *Filbert and Kellogg*, 1979]. In this study, we correct nominal orientation of the bow shock by assumption of rotational symmetry about the solar wind flow line defined by orbital motion of the Earth and velocity vector of the solar wind measured by the LEP. In addition, we also correct a shape of the bow shock affected by solar wind ram pressure. The standoff distance a_s of the bow shock is affected by the ram pressure P_{sw} and the Mach number M in the solar wind, according to the equation $a_s = \alpha P_{sw}^{-1/6}(M^2+3)/(4M^2)$, where the ratio of specific heats γ is taken to be 5/3 [*Spreiter et al.*, 1966]. Since the Mach number in the solar wind is significantly greater than unity, a_s is roughly in proportion to $P_{sw}^{-1/6}$. In this study, we assume that both a_s and b_s is in proportion to $P_{sw}^{-1/6}$, indicated by

$$\begin{aligned} a_s &= a_{s0}(P_{sw}/P_{sw0})^{-1/6} \\ b_s &= b_{s0}(P_{sw}/P_{sw0})^{-1/6} \end{aligned} \tag{3.2}$$

where the constants a_{s0}, b_{s0}, and P_{sw0} are 14.6 R_E, 25.6 R_E, and 0.98 nPa, respectively. Figure 3.11 shows deviations between predicted and observed bow shock locations projected on the Sun-Earth line in 30 bow shock crossings of GEOTAIL. The revised bow shock locations agree well with the observed locations within ± 2 R_E in $|Y_{\mathrm{GSE}}|$ <20 R_E.

3.3.2 Global distributions

First, we investigate global distributions of plasma waves and energetic particles to study basic physical conditions in the foreshock region and at the bow shock. Figure 3.12 shows the distributions of plasma waves on the GSE coordinates. Figure 3.12 (a)-(b) show the distributions of Langmuir wave and $2f_p$ radiation. Both Langmuir wave and $2f_p$ radiation are intense in the foreshock region and weak in the downstream of the bow shock. It suggests that both waves are generated in the foreshock region filled with

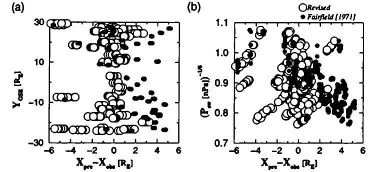

Figure 3.11: Deviation between predicted (X_{prd}) and observed (X_{obs}) locations of the bow shock projected on the Sun-Earth line in 30 bow shock crossings of GEOTAIL. X-axis is the deviation defined as ($X_{prd} - X_{obs}$). Y-axis is (a) Y_{GSE} of GEOTAIL, and (b) solar wind ram pressure, P_{sw}. Filled circles are the deviation from nominal bow shock locations [cf. *Fairfield*, 1971]. Blank circles are those from revised bow shock locations.

energetic electron beam, and the shock overshoot reflects the $2f_p$ radiation. Figure 3.12 (c)-(e) show distributions of electrostatic and electromagnetic waves below f_p. We find that the distributions of low frequency waves behind the bow shock are not uniform along the bow shock: Electric field at several kHz are active in the foot portion of the bow shock (Figure 3.12 (c)), while electrostatic and electromagnetic waves below 1 kHz are active in the nose portion of the bow shock (Figure 3.12 (d)-(e)).

Such non-uniformity is also indicated in distributions of energetic particles shown in Figure 3.13. Figure 3.13 shows the distributions of particles which have large velocities parallel to the local IMF. It is known that the compression ratio of magnetic fields is larger at the nose portion of the bow shock [cf. *Slavin et al.*, 1996]. Therefore, we can expect that the non-uniform plasma wave features might suggest the difference of energy dissipation processes associated with portions of the bow shock. In addition, since amount of magnetic overshoot at the bow shock should be positively correlated with amount of electron reflection [*Mellott and Livesey*, 1987], we also expect that physical conditions at the bow shock should affect the distributions of energetic particles in the foreshock region.

3.3.3 Spatial distributions in the foreshock

Next, we investigate the distributions of plasma waves and energetic particles in the foreshock region. In this analysis, we select only the data observed in the foreshock region based on three conditions: The first is observed location, in upstream of the bow

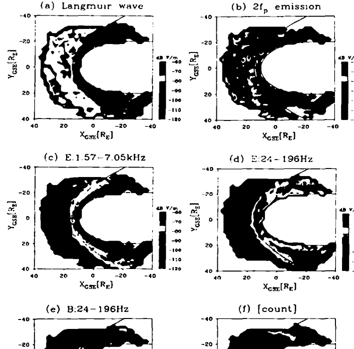

Figure 3.12: Global distributions of plasma waves. (a) Langmuir wave (dB V/m); (b) $2f_p$ radiation (dB V/m); (c) electric field in 1.57-7.05 kHz (dB V/m); (d) electric field in 31-100 Hz (dB V/m); (e) magnetic field in 31-100 Hz (dB nT); (f) number of samples.

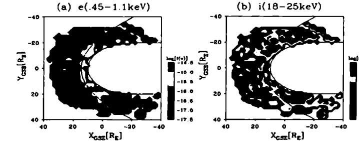

Figure 3.13: Global distributions of energetic particles with velocities parallel to the local IMF orientation. (a) electrons in 0.45-1.1 keV (s^3/m^6); (b) ions in 18-25 keV (s^3/m^6).

shock location predicted by the method which is described in the previous section. The second is plasma density at GEOTAIL, below 1.3 × N_{WIND} (N_{WIND}: proton density at WIND in upstream of the predicted bow shock location). The third is magnetic field strength at GEOTAIL, below 10 nT. These conditions are also effective to reject cases with unusual solar wind conditions. In addition, we do not use data observed when the kinetic energy flux of the solar wind is more than 4 mWm^{-2}.

Figure 3.14 and Figure 3.15 show mappings of plasma waves and energetic particles in the foreshock region. These are based on the normalized foreshock coordinates which preserve *Diff* and *Dist* values on a common diagram of the nominal IMF at 120° stream angle and nominal shock. Although the assumed azimuth angle of IMF, ϕ_B=120°, is different from that expected from Parker spiral around the Earth, 135°, we select it because the orbit of GEOTAIL can not cover the contact point when ϕ_B is close to parallel to the Sun-Earth line. Based on the accuracy of predicted bow shock location, the normalized plane is divided into 2×2 R_E squares.

In Figure 3.14 and Figure 3.15, we confirm classical views of the electron and ion foreshocks. Figure 3.14 (a) indicates that strong Langmuir wave is concentrated at the leading edge of the electron foreshock just behind the IMF line tangent to the bow shock. On the other hand, Figure 3.14 (c) also indicates that the Doppler-shifted ion acoustic wave at several kHz is distributed in the ion foreshock which is far downstream of the tangential IMF line. The distribution of each wave is well superposed on distribution of energetic electrons and ions shown in Figure 3.15, respectively. In the ion foreshock, enhancement of electric field below 1 kHz is also found. Such enhancement is whistler wave associated with either ion beam or dispersed ion distributions [*Anderson et al.*, 1981] or part of electrostatic noise associated with strong turbulence caused by dense ion beam.

Distribution of flux of $2f_p$ radiation is not concentrated along the tangential IMF line because of propagation from the source. However, we can confirm in Figure 3.14 (b) that distribution centroid of $2f_p$ radiation is well superposed on the tangential IMF

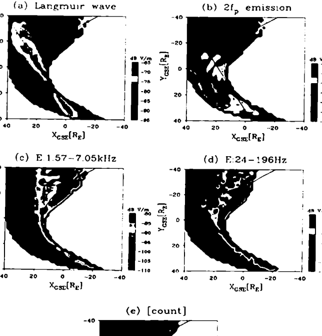

Figure 3.14: The mappings of plasma waves in the foreshock region observed from November 1994 to April 1996. Plots are using normalized foreshock coordinates on a common diagram of the nominal IMF at 120° stream angle and nominal shock. (a) Langmuir wave; (b) $2f_p$ radiation; (c) electric field in 1.57-7.05 kHz; (d) electric field in 24-196 Hz; (e) number of samples.

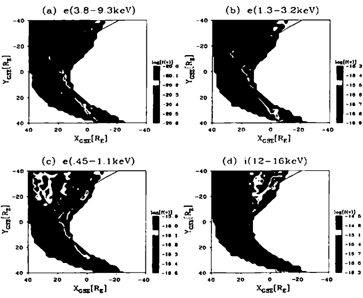

Figure 3.15: The mappings of the energetic particles with velocities parallel to the local IMF orientation in the terrestrial foreshock observed from November 1994 to April 1996. Plots are using normalized foreshock coordinates on a common diagram of the nominal IMF at 120° stream angle and nominal shock. (a) electrons in 3.8-9.3 keV; (b) electrons in 1.3-3.2 keV; (c) electrons in 0.45-1.1 keV; (d) ions in 12-16 keV.

line where intense Langmuir wave is observed. Therefore, we suggest that the $2f_p$ radio source centroid is on the IMF line tangent to the bow shock, and superposed on the electron foreshock. This indicates that the source of $2f_p$ radiation is in the region filled with Langmuir wave and electron beam. Distribution of $2f_p$ radiations also indicates that Doppler-shifted ion acoustic wave at several kHz is not responsible on generation of $2f_p$ radiation in the foreshock region.

We can also find some interesting features in Figure 3.14. Both Langmuir waves and $2f_p$ radiation are not strong in the region close to the contact point, and show gradual decrease beyond $|Dist| = 30$-$40\ R_E$. The latter is also found in the electric field in 24-196 Hz. We should compare these features with distributions of energetic electrons indicated in Figure 3.15. Figure 3.15 show that distribution peaks of Langmuir wave and $2f_p$ radiation is superposed on those of energetic electrons above 1 keV. In addition, distributions of energetic electrons seem more concentrated around the contact point than those of Langmuir wave and $2f_p$ radiation. Even lack of energetic electrons in the region close to the contact point might be not real, caused by a geometrical effect, because thickness of the electron foreshock is relatively thin.

Although a beaming effect of $2f_p$ radiation parallel to the tangential IMF line can at least explain the distribution of $2f_p$ radiation, these results agree well with the results of remote observations in Chapter 2.

3.3.4 Influences of solar wind parameters

Next, we investigate variation of plasma wave activities affected by solar wind parameters. We already suggested that spatial distribution of $2f_p$ radiation is correlated well with that of Langmuir wave and energetic electrons. This indicates that the total power of the $2f_p$ radiation is positively correlated with those of the Langmuir wave and electron beam in the electron foreshock. On this point of view, we study two parameters which can affect the foreshock electron beams: 'kinetic energy flow of the solar wind' and 'orientation of the IMF'.

Kinetic energy flow of the solar wind

First, we show evaluation of the influence of kinetic energy flow of the solar wind on the foreshock electron beams. Total energy of reflected electron beam is approximately indicated as the product of (average energy of a reflected electron) and (density of reflected electrons) Average energy of a reflected electron parallel to the IMF is proportional to $m_e v_{sw}^2/cos^2\theta_{Bn}$, where v_{sw} is the solar wind velocity and θ_{Bn} is the angle between normal of the bow shock and the IMF at the bow shock surface [*Leroy and Mangeney*, 1984], while density of reflected electrons is proportional to $n_{sw}v_{sw}$, where n_{sw} is density of the solar wind [*Wu*, 1984; *Leroy and Mangeney*, 1984]. Therefore, we can estimate the total energy of reflected electron beam $\propto n_{sw}m_e v_{sw}^3$. The value $n_{sw}m_e v_{sw}^3$ indicates the kinetic energy flow of the solar wind [*MacDowall et al.*, 1992].

Here, we investigate the correlation of activities of plasma waves and energetic particles with kinetic energy flow of the solar wind. Figure 3.16 shows correlation between plasma wave activity and kinetic energy flow of the solar wind, $n_{sw}m_e v_{sw}^3$

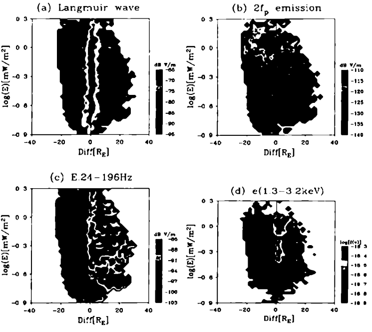

Figure 3.16: Activities of plasma waves and energetic particles correlated with kinetic energy flow in the solar wind, $n_{sw}m_e v_{sw}^3$ (mW/m^2), observed from November 1994 to April 1996. X-axis is *Diff*, and Y-axis is $\log(n_{sw}m_e v_{sw}^3)$, respectively. (a) Langmuir wave; (b) $2f_p$ radiation; (c) electric field in 24-196 Hz; (d) electrons in 1.3-3.2 keV.

(mW/m²), determined by particle data obtained by the LEP. X-axis is *Diff*, and Y-axis is $\log(n_{sw}m_e v_{sw}^3)$, respectively. In Figure 3.16 (b) and (d), we find that strength of the $2f_p$ radiation and population of energetic electrons is positively correlated with $n_{sw}m_e v_{sw}^3$. Positive correlation is also found in the electric field below 1 kHz (Figure 3.16 (c)). On the other hand, we did not confirm the same correlation in the Langmuir wave. Although it might be caused by the limitation of dynamic range of the SFA and/or rejection of saturated data, we should need further investigations.

Orientation of the interplanetary magnetic field

We already suggested that magnetic overshoot should be positively correlated with amount of electron reflection at the bow shock [*Mellott and Livesey*, 1987]. Since compression ratio of magnetic fields behind the bow shock is larger at the nose portion of the bow shock [cf. *Slavin et al.*, 1996], we can expect that population of energetic electrons show increase when the contact point is close to the nose portion of the bow shock. Since the contact point of tangential IMF line is defined by orientation of the IMF, we investigate the correlation of plasma waves and energetic electrons with orientation of the IMF.

Figure 3.17 shows correlation of activities of plasma waves and energetic particles with the azimuth angle of IMF, ϕ_B. X-axis indicates *Diff*, and Y-axis indicates ϕ_B, respectively. We should pay attention that when ϕ_B is close to 0°, the contact point is far downstream of the coverage of GEOTAIL trajectories. In these cases, free energy of observed electrons might be consumed by long trip from the contact point. However, in Figure 3.17, we can clearly find that Langmuir wave, $2f_p$ radiation, electric field below 1 kHz, and population of energetic electrons are enhanced on the tangential IMF line when ϕ_B is close to 90°. These results agree well with expectations described above.

3.4 Direct observations of plasma waves and energetic particles in the electron foreshock

In this section, we show some case studies of local observations of plasma waves and energetic particles in the electron foreshock. Although such investigations do not present general views because of large sampling errors, we can get more concrete and precise information of physical conditions in the electron foreshock. Data of plasma waves, energetic particles and simultaneous local IMF are obtained by the Plasma Wave Instrument (PWI) [*Matsumoto et al.*, 1992], the Low Energy Particle Experiment (LEP) [*Mukai et al.*, 1992] and the Magnetic Field Measurements (MGF) [*Kokubun et al.*, 1992] aboard the GEOTAIL spacecraft.
percentage

3.4.1 Physical conditions at the leading edge of the electron foreshock

First, we investigate plasma waves and energetic electrons along the tangential IMF line to study the physical conditions at leading edge of the electron foreshock. We indicate that $2f_p$ radio source is superposed on upstream and downstream wings of the electron

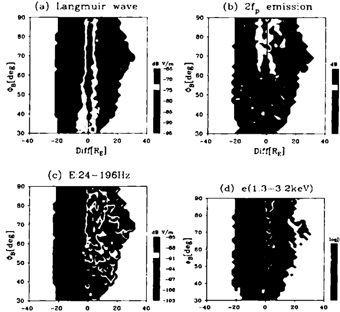

Figure 3.17: Activities of plasma waves and energetic particles correlated with the azimuth angle of IMF, ϕ_B, observed from November 1994 to April 1996. X-axis is *Diff*, and Y-axis is ϕ_B, respectively. (a) Langmuir waves; (b) $2f_p$ radiations; (c) electric field in 24-196 Hz; (d) electrons in 1.3-3.2 keV.

foreshock, while that is not concentrated around the contact point. Therefore, we can expect to find evolution of plasma waves and energetic electrons along the IMF line associated with distance from the contact point. In order to investigate the origin of such distributions, we select samples observed at leading edge of the electron foreshock along the tangential IMF line with azimuth angle of $\phi_B = 120°$, with $Dist = 0, -5, -10, -15, -20, -25, -30\ R_E$

Figure 3.18 (a) shows peak spectra of plasma waves within ±1 minute from the crossings across the leading edge of the electron foreshock. Figure 3.18 (b) shows same samples in which spectrum in the solar wind is subtracted. In this study, we use the MCA which has larger dynamic range than the SFA. Electron plasma frequency of each spectrum is normalized at 30 kHz. For clarity of presentation, we plot peak intensity of Langmuir waves and electric field in 31-100 Hz as a function of $Dist$ in Figure 3.18 (c)-(d). In Figure 3.18, we confirm the results of the spatial distributions of plasma waves. First, enhancement of Langmuir waves is observed at all crossings. However, its strength is relatively weak in the region close to the contact point, and largest in the region with $|Dist|$ beyond 10 R_E. Secondly, enhancement of low frequency electric field below ion plasma frequency ~700 Hz is observed at all crossings. However, its strength does not show clear variation depending on $|Dist|$.

We also show distribution functions of electrons simultaneously observed by the LEP in Figure 3.19. Plotted samples are 12 second values. We select these samples on a condition that the population of electrons at 30,000 km/s (= 0.1 c = 2.56 keV) is largest in the distribution function within ±1 minute from the crossings across the leading edge of the electron foreshock. Left panels indicate distribution function of electron velocity. All distribution functions have anti-symmetric component. Therefore, quasi-beam component can be defined by subtraction of the downstream component from the upstream component in the distribution functions [*Miki et al.*, 1996]. Middle panels indicate density of quasi-beam component, and right panels indicate energy of quasi-beam component. In all panels, positive direction is defined as to upstream. Unfortunately, we can not confirm clear evolution of electron beam by the time-of-flight mechanism associated with increase of $|Dist|$. It might be because the time resolution of particle measurements is relatively coarse compared with expected decay time of sharp beam components by wave-particle interactions. However, we can still find one interesting feature. Figure 3.20 shows densities and kinetic energies of quasi-beam components indicated in Figure 3.19. Thick and thin lines indicate density ratio (%) and kinetic energy (J/m^3) of quasi-beam components, respectively. Associated with increase of distance from the contact point, the density ratio of quasi-beam component decreases faster than the kinetic energy.

3.4.2 Physical conditions on the pass across the electron foreshock

Next, we investigate plasma waves and energetic electrons on the pass across the leading edge of the electron foreshock. Here, we present one of such cases observed in 1:30-2:00 UT on 6 April 1995 (Figure 3.21). In this case, GEOTAIL passed the leading edge of the electron foreshock at 1:39 and 1:47 UT. Emission lines around ~26 kHz and ~52 kHz indicate Langmuir wave and $2f_p$ radiation, respectively. Fortunately, we can

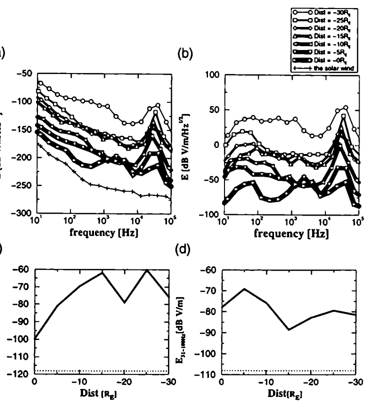

Figure 3.18: Spectra of electric field observed by the PWI/MCA at leading edge of the upstream wing of the electron foreshock along the tangential IMF line with azimuth angle of $\phi_B = 120°$. Samples are observed at *Dist* = $-30\ R_E$ (1:02 UT, 4 August 1995), $-25\ R_E$ (3:39 UT, 15 June 1995), $-20\ R_E$ (0:37 UT, 19 May 1995), $-15\ R_E$ (4:27 UT, 8 May 1995), $-10\ R_E$ (3:51 UT, 27 August 1995), $-5\ R_E$ (3:25 UT, 11 February 1995), and $0\ R_E$ (2:24 UT, 26 July 1995). (a) Peak spectra within ± 1 minute from crossings across leading edge of the electron foreshock. Lowest line is typical spectrum in the solar wind (3:00 UT, 4 August 1995); (b) Peak spectra in which the solar wind spectrum is subtracted; (c) Peak intensity of Langmuir wave; (d) Peak intensity of electric field in 31-100 Hz. In (a)-(b), the plotted data are each downshifted by 15 dB. Electron plasma frequencies are normalized at 30 kHz. In (c)-(d), X-axis is *Dist* of observed locations. Dotted line is typical field intensity observed in the solar wind.

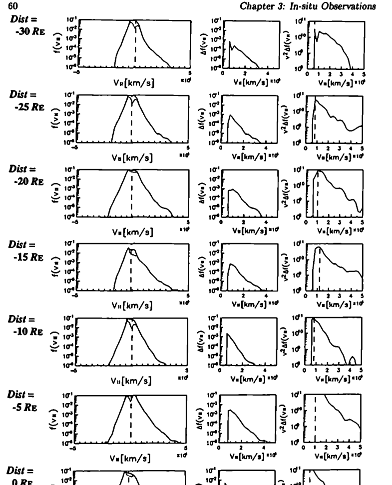

Figure 3.19: Distribution functions of electrons parallel to the IMF lines observed by the LEP at the leading edge of the electron foreshock. Left, middle and right panels are velocity distribution function, density of the quasi-beam component, and kinetic energy of the quasi-beam component.

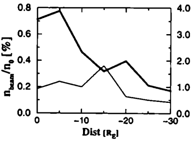

Figure 3.20: Densities (thick line) and kinetic energies (thin line) of quasi-beam components observed at leading edge of upstream wing of the electron foreshock. X-axis is *Dist* of observed locations. Left and right Y-axis indicates density ratio (%) and kinetic energy (J/m^3) of the quasi-beam component.

use the MCA at channels of 31 kHz and 56 kHz as indicators of Langmuir wave and $2f_p$ radiation, respectively. Bandwidth of both MCA channels are 7.5 % of its central frequency with cross talk from the neighbor channels less than 50 dB. We can confirm in both SFA and MCA panels that Langmuir wave is enhanced at the leading edge of the electron foreshock associated with enhancement of energetic electrons. Vertical lines in the SFA panel around 1:39 UT and 1:47 UT are caused by saturation of preamplifier by intense Langmuir waves. We can also find that waves at $2f_p$ and below 1 kHz are also intensified at the leading edge of the electron foreshock associated with enhancement of Langmuir wave.

In Figure 3.22, we show intensity of plasma waves measured by the SFA (dotted lines) and the MCA (solid lines). When GEOTAIL is at the leading edge of the electron foreshock, intensity of Langmuir waves show dramatic increase, and waves at $2f_p$ and below 1 kHz is also enhanced in both SFA and MCA. We are afraid artificial enhancement in the SFA/MCA by saturation from intense Langmuir wave and in the MCA by cross-talk between neighboring channels. However, if it is real, enhancement at $2f_p$ should be electrostatic wave [*Klimas*, 1983; *Yoon et al.*, 1994] because fast decrease and increase of this wave at the edge of the electron foreshock do not show any evidence of propagation.

We farther analyze the variations of 'local' waves at $2f_p$ and below 1 kHz indicated in Figure 3.22 observed by the MCA which is hard to be influenced by saturation. Figure 3.23 shows the correlations of the plasma wave activities at $2f_p$ and below 1 kHz with that of Langmuir wave at leading edge of the electron foreshock observed at the leading edge of the electron foreshock in 1:37-1:39 UT and 1:47-1:49 UT. Associated with the most intense Langmuir wave, we can find that typical ratio of 'local' $2f_p$ wave to Langmuir wave is less than -40 dB, while that of low frequency electrostatic wave is less than -10 dB, respectively.

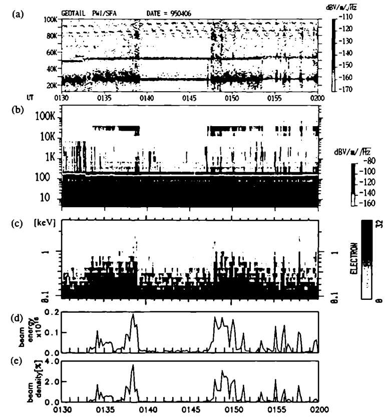

Figure 3.21: Plasma waves and electron energy distributions observed when GEOTAIL passed leading edge of the electron foreshock at 1:39 and 1:47 UT on 6 April 1996. (a) electric field above 12.5 kHz observed by the SFA; (b) electric field above 5.6 Hz observed by the MCA; (c) omni-directional electrons observed by the LEP; (d) kinetic energy (J/m^3) and (e) density ratio (%) of quasi-beam component.

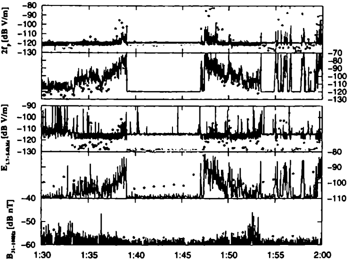

Figure 3.22: Plasma waves observed when GEOTAIL passed the leading edge of electron foreshock at 1:39 and 1:47 UT on 6 April 1995. From the top, we show strength of the $2f_p$ wave at ~52 kHz (SFA) / 56 kHz (MCA), Langmuir wave at ~26 kHz (SFA) / 31 kHz (MCA), electric field in 24-110 Hz (SFA) / 31-100 Hz (MCA), and magnetic field in 24-110 Hz (SFA) / 31-100 Hz (MCA). Solid and dotted lines are data observed by the MCA (0.5 seconds interval) and the SFA (8 seconds interval above 1.7 kHz; 64 seconds interval below 1.7 kHz), respectively.

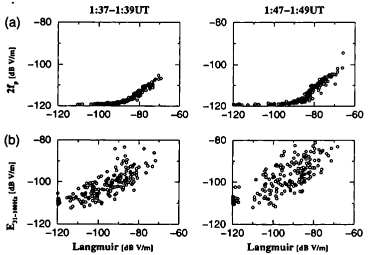

Figure 3.23: Plasma wave activities observed by the PWI/MCA in 0.5 second interval when GEOTAIL passed the leading edge of the electron foreshock at 1:39 UT (left) and 1:47 UT (right) on 6 April 1995. (a) Correlations between Langmuir wave and $2f_p$ wave; (b) Correlations between Langmuir wave and electric field in 31–100 Hz.

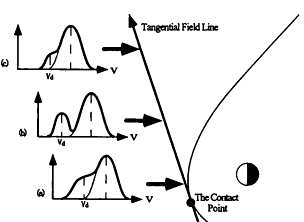

Figure 3.24: A schematic model of formation and nonlinear diffusion of electron beam along the tangential IMF line. Left panels show velocity distributions of background electrons (thin lines) and beam electrons(thick lines). Dotted lines indicate the distributions after diffusion by wave-particle interactions. (a) $|Dist| \sim 0\ R_E$; (b) $|Dist| \sim 30\ R_E$; (c) $|Dist| \gg 30\ R_E$.

3.5 Discussions

First, we evaluate the spatial distributions of plasma waves and energetic particles in the foreshock region. We find that the centroid of the $2f_p$ radio source is superposed on the IMF line tangent to the bow shock. This directly indicates that the $2f_p$ radio source is living with intense Langmuir wave and energetic electron beam, and independent of sporadic Doppler-shifted ion acoustic wave at several kHz.

We also find that the source centroid locates in the region with a distance of 5–40 R_E from the contact point, and not concentrated around the contact point. In addition, distributions of energetic electrons seem more concentrated around the contact point than those of Langmuir wave and $2f_p$ radiation. These results suggest two interpretations; First, less Langmuir wave and $2f_p$ radiation around the contact point suggest lack of a sharp electron beam in the region close to the contact point. Because we can find energetic electrons in this region, this might be because of shortage of flight time for the time-of-flight beam formation process. This idea is also supported by much population of low energy electrons in the region close to the contact point. Secondly, decrease of Langmuir wave and $2f_p$ radiation beyond $|Dist| = 30$–$40\ R_E$ suggests consumption of energetic electron beam associated with long flight along the tangential IMF line from the contact point. This idea is supported by less population of high energy electrons above 1 keV in the region distant from the contact point.

We also confirm that strength of $2f_p$ radiation and population of energetic electrons are positively correlated with solar wind kinetic flow, $n_{sw}m_e v_{sw}^3$. This supports the ideas that population of the energetic electron beams depends on kinetic energy flow of the solar wind, and the $2f_p$ radiation can describe the total power of energetic electron beams.

We also find that Langmuir wave, $2f_p$ radiation, electric field below 1 kHz, and energetic electrons show more increase on the IMF line tangent to the nose portion of the bow shock. This indicates that the population of energetic electrons is enhanced on the IMF line tangent to the nose portion of the bow shock associated with increase of reflection ratio, and that Langmuir wave and the $2f_p$ radiation are also enhanced associated with increase of kinetic energy of electron beams. These results agree well with our expectations.

Secondly, we evaluate local observations of plasma waves and energetic particles on and across leading edge of the electron foreshock. We confirm that plasma wave activities are most intense beyond $|Dist > 10R_E$. Unfortunately, we can not find clear beam components evolved by the time-of-flight mechanism, However, we find that density ratio of quasi-beam component shows faster decrease of their kinetic energy. This indicates decrease of dense low energy component along the trip of quasi-beam components. Such evolution feature favors the beam formation process by lack of low energy component through the time-of-flight effect. Although including large ambiguities caused by sampling method, those results are also consistent well with the results in previous sections.

At the leading edge of the electron foreshock, we also find clear increase of plasma waves at $2f_p$ and below 1 kHz in both SFA and MCA, associated with dramatic increase of Langmuir wave and high energy electrons. Although we should be conscious of artificial contamination, we can evaluate upper limit of strength of locally generated waves at $2f_p$ and below 1 kHz. Upper limit of intensity ratio of 'local' waves at $2f_p$ to the Langmuir wave is -40 dB, while that of low frequency electrostatic wave is -10 dB. These values give strong limitation when we evaluate generation mechanisms of the $2f_p$ radiation.

Based on those results, we can show a schematic model of formation and nonlinear diffusion of electron beam in the electron foreshock (Figure 3.24). At the region close to the contact point, reflected electrons form a initial bump in their distribution functions. However, since such bump includes lower energy electrons, induced perturbations of beam-plasma instability are not large enough to generate strong Langmuir waves and $2f_p$ radiation. On the way along the tangent IMF line, accelerated electrons gradually forms a thin beam at the leading edge of the electron foreshock by dropping out of low energy component through the time-of-flight effect. Such beam can induce strong beam-plasma instability and generates intense Langmuir wave, low frequency electrostatic wave, and the $2f_p$ radiation. High energy electrons are gradually consumed through such wave-particle interactions, and emissivity of the $2f_p$ radiation smoothly decrease in the region far from the contact point.

3.6 Conclusion

In this chapter, we investigate the spatial distributions and local observations of plasma waves and energetic particles in the foreshock region. In summary, our current conclusion is as follows:

(1) The centroid of the $2f_p$ radio source is on the IMF line tangent to the bow shock. This indicates that the $2f_p$ radiation is associated with intense Langmuir wave and energetic electron beam, and independent of Doppler-shifted ion acoustic wave.

(2) The source centroid locates at the distance of 5-40 R_E from the contact point, and not concentrated around the contact point. This suggests formation and consumption of sharp electron beams through time-of-flight effect and wave–particle interactions.

(3) Strength of the $2f_p$ radiation is positively correlated with solar wind kinetic flow, $n_{sw}v_{sw}^3$. Therefore, the $2f_p$ radiation can describe the population of energetic electron beams which also depends on solar wind kinetic energy flow.

(4) Langmuir wave and the $2f_p$ radiation seem to be more intense on the IMF line tangent to the nose portion of the bow shock. This should be because of non-uniform overshoot at the bow shock which affects reflection ratio of electrons.

(5) We can not confirm clear evolution of electron beams by the time-of-flight mechanism. However, we confirm that density ratio of quasi-beam component shows faster decrease than the kinetic energy. This favors the beam formation process through the time-of-flight effect.

(6) We find clear increase of plasma waves at $2f_p$ and below 1 kHz at the leading edge of the electron foreshock, associated with dramatic enhancement of Langmuir wave and energetic electrons. Upper limit of typical ratio of 'electrostatic' $2f_p$ wave to the Langmuir wave is -40 dB, while while that of low frequency electrostatic wave is -10 dB.

In addition, we propose a schematic model of formation and nonlinear diffusion of electron beam in the electron foreshock. Such model can explain distribution of emissivity of $2f_p$ radiation. This model will be tested by careful observations of particle distributions and beaming of $2f_p$ radiations. These results also give strong guide lines to reproduce the $2f_p$ radiation via numerical experiments presented in next chapter.

In addition, we have still an unsolved problem. We do not definitely define which is the favorable $2f_p$ radio source, 'the leading edge of the electron foreshock' or 'the deep electron foreshock'. The former has more intense Langmuir wave and low frequency electrostatic wave, and the latter has broader volume and low frequency electromagnetic wave. Although the distribution of $2f_p$ radiation which indicates evolution effect of electron beams favors leading edge of the electron foreshock, we need to know generation process of $2f_p$ radiation and role of low frequency waves to solve this problem.

Chapter 4

Numerical Simulations of $2f_p$ radiation

We study self-consistent nonlinear evolution of electron plasma waves excited by electron beams for investigation of $2f_p$ radiation generated in the electron foreshock. Numerical simulations are executed by electromagnetic particle code, KEMPO, in 1D and 2D periodic systems.

In 1D periodic systems, we generate electrostatic $2f_p$ waves at $k \sim 2k_L$, where k_L is wave number of beam-excited Langmuir waves. The electrostatic $2f_p$ waves are generated after the end of initial stage. Growth of electrostatic $2f_p$ waves are strongly correlated with peak amplitude of Langmuir waves in ω-k space, and independent of amplitude of backscattered Langmuir waves. Such features support the generation process of wave–wave coupling of two of beam-excited Langmuir waves. Typical amplitude ratio of electrostatic $2f_p$ waves to Langmuir waves is below -40 dB, which is consistent with the value observed at the leading edge of the electron foreshock presented in Chapter 3.

In a 2D periodic system, we also generate electrostatic $2f_p$ waves and confirm the results in 1D systems. In addition, we generate electromagnetic $2f_p$ waves at $k \sim \pm 2\Pi_e/c$. Growth of electromagnetic $2f_p$ waves are strongly correlated with that of backscattered Langmuir waves and independent of the electrostatic $2f_p$ waves. Such features support the classical generation process of wave-wave coupling of beam-excited and backscattered Langmuir waves. Typical growth time of electromagnetic $2f_p$ wave is about 200-$400/\Pi_e$, which does not contradict to thickness of the electron foreshock. Typical amplitude ratio of electromagnetic $2f_p$ waves to Langmuir waves is below -80 dB, which is too weak to detect local enhancement at the electron foreshock.

4.1 Introduction: Generation process of $2f_p$ radiation in the electron foreshock

In the previous chapter, we showed by in-situ observations that the leading edge of the electron foreshock is the most possible location of $2f_p$ radio source. However, in order to interpret various features studied by both remote and in-situ observations, we need to know precise generation processes of $2f_p$ radiation based on activities of plasma waves and energetic electrons in this region.

In the past, several mechanisms have been proposed to explain generation of $2f_p$ radiation by intense Langmuir waves in the electron foreshock. Although strong instability processes have been proposed [cf. *Gurnett and Anderson*, 1977], intensity of observed Langmuir waves is generally too weak to produce electromagnetic waves by these mechanisms [cf. *Kellogg et al.*, 1996]. Therefore, we concentrate to present overview of weak instability theories; conversion from Langmuir waves through wave-wave interactions.

The most major theory of conversion from Langmuir waves is based on three-wave process. *Filbert and Kellogg* [1979] proposed that beam-excited Langmuir waves lead to the oscillating-two-stream instability which induces the radiation at $2f_p$ through the three-wave nonlinear process [*Tsytovich*, 1970];

$$L + L \rightarrow T \tag{4.1}$$

where L denotes the Langmuir wave and T denotes the transverse wave. The process (4.1) requires the following matching conditions to conserve wave momentum and energy;

$$\begin{aligned} \mathbf{k}_L + \mathbf{k}_L &= \mathbf{k}_T \\ \omega_L + \omega_L &= \omega_T \end{aligned} \tag{4.2}$$

where $\mathbf{k}$ is wave number vector and ω is wave frequency, respectively. The electromagnetic field strength, E_{em}^2, generated by this mechanism in a slab is evaluated as

$$E_{em}^2(2\omega_p) = \frac{\pi}{3} E_{es}^4(\omega_p) \frac{r_e R}{mc^2} \frac{k^2}{(\Delta k)^3} \tag{4.3}$$

where R is the thickness of the slab, r_e is the classical electron radius ($=e^2/mc^2$), k is the average wave number of the electrostatic waves, Δk is the volume in k space occupied by these waves, E_{es} is their field strength, and ω_p is their approximate frequency. When parameters are assumed by foreshock values as $\Delta k \sim \pi k^3/16$, $k = \omega_p/v_b$ with $v_b =$ 50,000 km/s, $E_{es} = 0.02$ V/m, and R is above 500 km, estimated electromagnetic field strength is about 3×10^{-5} V/m. *Cairns and Melrose* [1985] and *Cairns* [1988] also propose the generation of the radiation through the three-wave process including the presence of ion acoustic waves in the source region;

$$\begin{aligned} L \pm S &\rightarrow L' \\ L + L' &\rightarrow T \end{aligned} \tag{4.4}$$

where S, L, and T denote ion acoustic, Langmuir, and transverse waves, respectively. In the process (4.4), a secondary backscattered Langmuir wave L' is produced by the scattering of the primary Langmuir wave L off the ion acoustic wave S. The secondary backscattered Langmuir wave L' can also be produced by scattering off of background ions. However, the predicted growth rate of these three-wave processes are linearly proportional to time rather than exponential, and proportional to the product of field

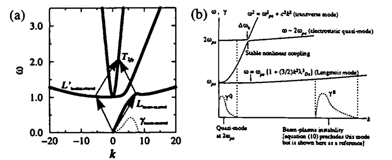

Figure 4.1: A schematic representation of $2f_p$ wave. (a) electromagnetic $2f_p$ wave; (b) quasi-mode of electrostatic $2f_p$ wave [*Yoon et al.*, 1994].

strength of two Langmuir waves Therefore, characteristic growth time is expected to be too long compared with time-scale constrained by physical dimensions of the electron foreshock [*Yoon et al.*, 1994].

Mode conversion from $2f_p$ electrostatic wave have been also presented. *Klimas* [1983] presented excitation of electrostatic harmonics of Langmuir wave generated by bump-on-tail instability. At the first linear growing phase, beam-excited Langmuir wave grow exponentially at field modes with phase velocities on positive slope of initial electron velocity distributions, while other modes decay exponentially by Landau damping. When the growing modes become very large compared to the decaying modes, quadratic wave-particle coupling terms in the Vlasov equation become non-negligible and pumps m-th order harmonic waves with large wave number $k \sim mk_L$, where k_L is wave number of beam-excited Langmuir waves. These electrostatic harmonics might nonlinearly be converted to electromagnetic waves in the region with spatial perturbations. *Yoon et al.* [1994] proposed other mechanism through the electrostatic quasi-mode at $2f_p$ with smaller wave number. Basic configuration of this theory is shown in Figure 4.1. Electrostatic $2f_p$ quasi-mode is excited by a thin energetic electron beam modulated by the large amplitude backscattered Langmuir waves, and efficiently coupled with electromagnetic mode. Order of growth rate of the quasi-mode is $\gg 10^{-3}\omega_e$, and electric field strength of electromagnetic wave is expected to same order of that of Langmuir waves when k-space width of backscattered Langmuir waves is narrow.

On the other hand, numerical simulations have been executed to produce $2f_p$ radiation in the computer space. There are two cases which succeed to reproduce electromagnetic $2f_p$ waves. *Pritchett and Dawson* [1983] employed a 2-1/2D electromagnetic particle simulation with a continuous inflow of thin beam ($n_b/n_0 \sim 1\%$) with open-boundary conditions. They produced the radiation near the plasma frequency. This radiation is emitted preferentially perpendicular to the beam, and is polarized with **E** parallel to the beam direction. They also produced much weaker second harmonic radiation. The production mechanism is found to be the scattering of Langmuir waves from ion-acoustic fluctuations through the three-wave process. *Akimoto et al.* [1988] also investigate electromagnetic radiation by strong Langmuir turbulence by 2-1/2D electromagnetic fluid simulation with periodic boundary conditions. They use a system with 200x200 λ_e (64x64 grid) with the turbulence parameter $W = E^2/4\pi n_0 T_e = 0.2$, the electron to ion mass ratio $m_e/m_i = 1/100$, the electron to ion temperature ratio $T_e/T_i = 1.0$, and electron thermal velocity $V_e = c/12.65$. During the first linear stage, electrostatic wave at Π_e is evolving from an initial linear wave packet into a planar soliton. During the second stage, electromagnetic waves at harmonics of Π_e are present from transverse instabilities of the soliton with quadrupole patterns.

There are also two cases of numerical simulations which succeed to reproduce electrostatic $2f_p$ waves. *Klimas* [1983] investigated the generation of electrostatic harmonics of the plasma frequency by numerical integration of the 1D Vlasov-Maxwell equation. They reproduce electrostatic turbulence of m-th harmonic wave with the wave number of mk_L. The mechanism for excitation of the electrostatic second harmonic wave is shown to be second-order wave-wave coupling of beam-excited Langmuir waves. *Nishikawa and Cairns* [1991] also investigated the self-consistent nonlinear evolution accompanied with thin electron beams by quasi-1D electrostatic particle code with periodic boundary conditions. They used three species of charged particles: background electrons, background ions and beam electrons with Maxwellian distribution functions. They used a system with 2048x4 λ_e, and the number of particles in a cell is 36. They studied three sets of parameters: $n_b = 0.05n_0$ and $V_d = 20.0V_e$, $n_b = 0.01n_0$ and $V_d = 20.0V_e$, and $n_b = 0.05n_0$ and $V_d = 0.09V_e$. Other parameters are $m_i/m_e = 1836$, $\Omega_e/\Pi_e = 1/3$, $T_i/T_e = 1.0$, and $T_b/T_e = 0.1$. Electrostatic waves near multiples of plasma frequency is generated by wave-wave coupling during the nonlinear stage of the simulations, thereby confirming the suggestions of *Klimas* [1983].

In this chapter, we try to reproduce physical processes at the electron foreshock in the computer space by full electromagnetic particle code. For this trial, we need large systems to produce both plasma waves with wave number from c/Π_e to $1/\lambda_D$ where c is light speed and λ_D is Debye length. In addition, we need long run with large number of particles to reproduce weak waves with small growth rate. First, we show 1D numerical simulations to investigate beam-plasma interactions with various plasma conditions expected in the electron foreshock. Next, we extend these results into 2D numerical simulations to investigate the generation process of $2f_p$ radiation in the electron foreshock.

4.2 1D simulations

In this section, we use a electromagnetic particle code, KEMPO [*Matsumoto and Omura*, 1985] for a one-dimensional periodic system with three species of charged particles; background electrons, background ions, and thin beam electrons whose densities are n_e, n_i, and n_b, respectively ($n_e + n_b = n_i$). Based on in-situ observations in the electron foreshock, we assume that the velocity distribution of each component is Maxwellian of the same temperature. Therefore, thermal velocities of these components, V_e, V_i, and V_b, satisfy the condition of $m_e V_e^2 = m_i V_i^2 = m_e V_b^2$. All simulation

Parameter	Values
Grid spacing Δx	0.02
Time step Δt	0.01
Number of grid points N_x	4096
Number of time steps N_t	32768
Number of background electrons per cell	64, 32
Number of background ions per cell	0, 32
Number of beam electrons per cell	16, 8
Light speed c	1.0
Electron plasma frequency Π_e	1.0
Electron gyrofrequency Ω_e	$0.01\Pi_e$
Electron thermal velocity V_e	$0.02c$
Beam thermal velocity V_b	V_e
Electron to Ion mass ratio $R_m = m_e/m_i$	0, 1/1600, 1/100
Ion plasma frequency $\Pi_i = (m_e/m_i)^{-1/2}\Pi_e$	0, 0.025, 0.1
Ion thermal velocity $V_i = (m_e/m_i)^{-1/2}V_e$	0, 0.0005c, 0.002c
Beam drift velocity ratio $R_v = V_d/V_e$	5, 10, 20
Beam density ratio $R = n_b/(b_e + n_i)$	0.02, 0.04, 0.08

Table 4.1: Parameters for 1D simulations

parameters are listed in Table 4.1. We set the thermal velocity of background electrons as $V_e \sim 0.02c$. Although this value is too large compared with real value in the solar wind, $V_e < 0.005c$, we need higher thermal velocity to enlarge the Debye length λ_D of background electrons for saving memory size and length of simulation run. Since length of system and simulation run is 81.92 (4,096 grids) and 327.68 (32,768 counts), we can produce plasma waves with wave number below 157 (resolution: 0.077) and frequency below 314 (resolution: 0.019), respectively.

In the following simulation runs, we control three parameters; electron to ion mass ratio $R_m = m_e/m_i$, beam drift velocity ratio $R_v = V_d/V_e$, and beam density ratio $R_n = n_b/(n_e + n_b)$. First, we present a standard system with $R_m = 1/1600$, $R_v = 10.0$, $R_n = 0.02$. Next, we vary R_m from 0 to 1/100 keeping R_v and R_n constant, R_v from 5.0 to 20.0 keeping R_m and R_n constant, and R_n from 0.005 to 0.16 keeping R_m and R_v constant.

4.2.1 Standard case

First, we investigate the standard system with $R_m = m_e/m_i = 1/1600$, $R_v = V_d/V_e = 10.0$, and $R_n = n_b/(n_e + n_b) = 0.02$. These values are based on the condition observed at leading edge of the electron foreshock, except relative large beam density.

Figure 4.2 (a) shows phase diagrams for particles in the x-v_x space to indicate evolution of instability in particle distributions. At $t = 41$, we find formation of vortices by trapping of beam electrons in the initial stage. Later, these structures are gradually disordered and finally disappear via a quasi-linear diffusion process, and effective velocity of beam electrons gradually decreases. Background electrons are strongly modulated accompanied with formation of vortices at the initial stage.

Figure 4.2 (b) and (c) shows variation of total energy and spatial structure of electric

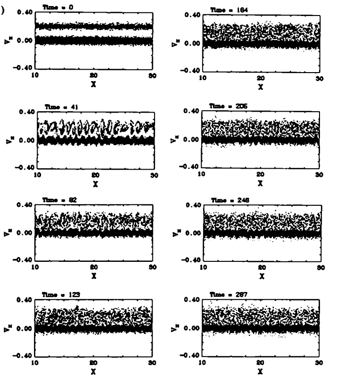

Figure 4.2: Evolution of particles and electric field in the standard run with R_m = 1/1600, R_v = 10.0, R_n = 0.02. (a) Phase diagrams of particles in x–v_x; (b) Total energy of electric field; (c) Spatial structure of electric field E_x along X-axis.

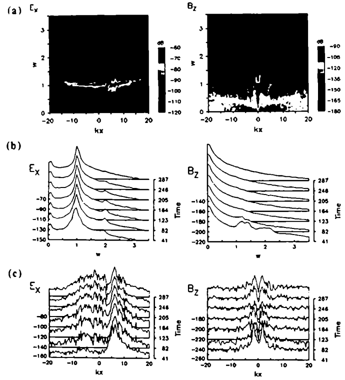

Figure 4.3: Plasma waves in E_x (left) and B_z (right) in the standard run with $R_m = 1/1600$, $R_v = 10.0$, $R_n = 0.02$. (a) the ω-k_x diagram in t = 82-246; (b) evolution of plasma waves in ω space; (c) that in k_x space with ω = 0.5-2.5 in E_x and ω = 1.75-2.25 in B_z. Electric and magnetic field is indicated in dB.

field. At the initial stage till t = 50, total energy of electric field shows exponential growth and electric field forms periodic potential wells, associated with formation of vortices. In t = 50-150, the total energy shows oscillation caused by exchange of energy with electrons and the potential wells gradually vary associated with broadening of beam velocity width. After t = 150, the total energy shows monotonous decrease by heating of particles via scattering by background ions and the potential wells is gradually destroyed, associated with decrease of modulation in the distribution function of background electrons.

Figure 4.3 shows evolution of plasma waves in electric field E_x (left) and in magnetic field B_z (right) generated in these processes. Figure 4.3 (a) shows the ω-k_x diagram of electric field in t = 82-246, obtained by Fourier transforming in space and time. We can find intense electrostatic waves at $\omega \sim 1.0 = \Pi_e$ and $k_x \sim +5.0(=\Pi_e/V_d)$ - +10.0, and weaker electrostatic waves at $\omega \sim 1.0 = \Pi_e$ and $k_x \sim -10.0$ - 0.0. Former waves are primary generated Langmuir waves by the weak beam instability, and latter waves are secondary generated Langmuir waves by backscattering off of background ions. In addition, we can also find weaker second harmonic waves at $\omega \sim 2.0 = 2\Pi_e$ and $k_x \sim +10.0{=}2\Pi_e/V_d)$ - +20.0. These are electrostatic $2f_p$ waves which satisfy the condition of $k_x \sim 2k_L$ where k_L is the wave number of Langmuir wave [cf. *Klimas*, 1983]. On the contrary, we can not find electromagnetic $2f_p$ waves at $\omega \sim 2\Pi_e$ and $k_x \sim 2.0 = 2\Pi_e/c$ in any plots in Figure 4.3.

Figure 4.3 (b) shows evolution of plasma wave spectrum in ω space obtained by Fourier transforming in time with time width of 82 of its central time. In Figure 4.3 (b), we can find that amplitude of the electrostatic $2f_p$ waves is enhanced in t = 82-205, just after the initial linear stage, and gradually decreases after t = 205 associated with decrease of beam-excited Langmuir waves. Typical ratio of amplitude of the $2f_p$ waves to that of Langmuir waves is below −40 dB, which is consistent with in-situ observations of local $2f_p$ waves at leading edge of the electron foreshock presented in Chapter 3.

Figure 4.3 (c) shows evolution of plasma wave spectrum in k_x space obtained by Fourier transforming in space. In Figure 4.3 (c), wave number of beam-excited Langmuir wave increases after the initial stage by broadening of velocity distributions of beam electrons. On the other hand, backscattered Langmuir waves show gradual increase after the initial stage. Since such increase does not show any influences on the electrostatic $2f_p$ waves, backscattered Langmuir waves is not responsible to generation of the electrostatic $2f_p$ waves at large wave number. In addition, we can not find low-k electrostatic quasi-mode at $2f_p$ induced by intense back-scattered Langmuir waves [cf. *Yoon et al.*, 1994].

4.2.2 Contribution of electron to ion mass ratio

Next, we vary the electron to ion mass ratio, $R_m = m_e/m_i$, to study contribution of ions in the beam-plasma process. We change R_m = (0, 1/1600, 1/100), keeping R_v = 10.0 and R_n = 0.02. Since we already showed the case with R_m = 1/1600 as the standard case, we show two cases: R_m = 0 and 1/100. In the former case ion mass is infinity to suppress the contribution of ions in the system, while in the latter case ion mass is lighter than realistic to enhance the responsibility of ions in the backscattering and destruction of beam-excited Langmuir waves.

Although initial evolution in both cases are basically common with the standard case, consequent evolution features are different. Figure 4.4 (a) shows phase diagrams for particles in the x-v_x space. At the initial stage, we found formation of vortices by trapping of beam electrons in both cases. After that, in the case of $R_m = 0$ modulation of background electrons is not destroyed till the end of the simulation run, while the modulation shows faster destruction in the case of R_m = 1/100. Such difference also

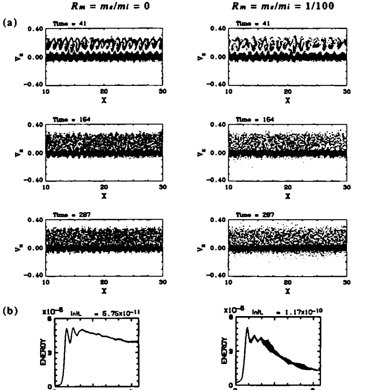

Figure 4.4: Evolution of particles and electric field in the simulation runs with $R_m = m_e/m_i = 0$ (left) and 1/100 (right), keeping $R_v = 10.0$ and $R_n = 0.02$. (a) Phase diagrams of particles in x-v_x; (b) Total energy of electric field; (c) Spatial structure of electric field E_x along X-axis.

appears in evolution of total energy and spatial structure of electric field indicated in Figure 4.4 (b) and (c). In both cases, total energy of electric field shows exponential growth at the initial stage till $t = 50$ and oscillation in t = 50–150, accompanied with formation of periodic potential wells. After that, in the case of $R_m = 0$, the total energy shows slower decrease and the potential wells are not destroyed till the end of the simulation run. On the other hand, in the case of $R_m = 1/100$, the total energy and the potential wells show faster decay than the standard case.

Figure 4.5 shows evolution of plasma waves in electric field E_x generated in both cases. In the case of $R_m = 0$, we can find sharp beam-excited Langmuir waves and clear enhancement of electrostatic $2f_p$ waves, while backscattered Langmuir waves are very weak (Figure 4.5 (a) and (c)). Amplitude of beam-excited Langmuir waves and electrostatic $2f_p$ waves are stable till the end of the simulation run which do not interact with background ions (Figure 4.5 (b)). On the other hand, in the case of $R_m = 1/100$, beam-excited Langmuir waves and electrostatic $2f_p$ waves are weak and not sharp, while backscattered Langmuir waves are very strong (Figure 4.5 (a) and (c)). Amplitude of beam-excited Langmuir waves and electrostatic $2f_p$ waves show faster decay than the standard case, especially after the end of initial stage through the generation of backscattered Langmuir waves with broad distribution in k_x space (Figure 4.5 (b)).

These results indicate that backscattering off of thermal ions is essential to decay of beam-excited Langmuir waves, and amplitude of intense beam-excited Langmuir waves is strongly correlated with that of electrostatic $2f_p$ waves.

4.2.3 Contribution of beam drift velocity ratio

Next, we vary the beam drift velocity ratio, $R_v = V_d/V_e$, to study contribution of velocity separation of beam electrons from background electrons which divide physical processes of wave–particle interactions into the bump-on-tail instability and the thin beam-plasma instability. We change R_v = (5.0, 10.0, 20.0), keeping $R_m = 1/1600$ and $R_n = 0.02$. Since we already show the case with $R_v = 10.0$ as the standard case, we show two cases: $R_v = 5.0$ and 20.0. The former indicates bump-on-tail instability in which beam component is partially mixed with background electrons in velocity distribution, while the latter shows thin beam–plasma instability in which beam component is clearly separated from background electrons.

Between both cases, initial evolution of the instability is rather different. Figure 4.6 (a) shows phase diagrams of particles in x–v_x space. In the case of $R_v = 5.0$, initial velocity distributions of particles show bump-on-tail structure in which background particles and beam electrons are partially mixed. Clear vortices of beam electrons and modulations of background electrons are not formed even at the initial stage. On the other hand, in the case of $R_v = 20.0$, velocity distributions show clear beam-plasma system like the standard case with $R_v = 10.0$. Such differences also appear in evolution of total energy and spatial structure of electric field indicated in Figure 4.6 (b) and (c). In the case of $R_v = 5.0$, total energy of electric field does not show exponential growth, and becomes stable after the end of initial stage. Large potential well is not formed in the spatial distribution of electric field. On the other hand, in the case of R_v = 20.0, basic features are common with the standard case, except much larger electric

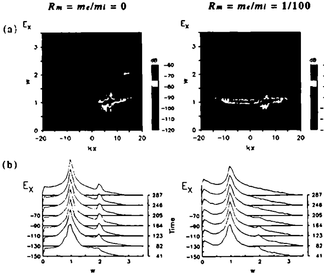

Figure 4.5: Plasma waves in E_x (dB) in the simulation runs with $R_m = m_e/m_i$ = 0 (left) and 1/100 (right), keeping R_v = 10.0 and R_n = 0.02. (a) the ω-k_x diagram in t = 82–246; (b) evolution of plasma waves in ω space; (c) that in k_x space with ω = 0.5–2.5 in E_x and ω = 1.75–2.25 in B_z.

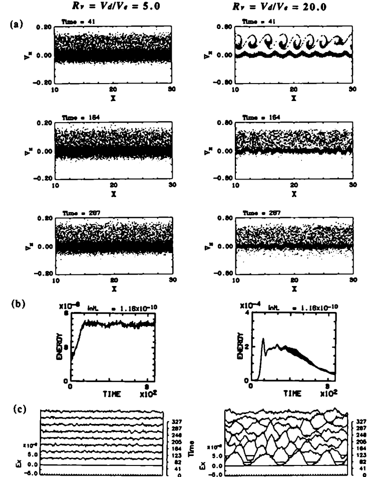

Figure 4.6: Evolution of particles and electric field in the simulation runs with $R_v = V_d/V_e = 5.0$ (left) and 20.0 (right), keeping $R_m = 1/1600$ and $R_n = 0.02$. (a) Phase diagrams of particles in x–v_x; (b) Total energy of electric field; (c) Spatial structure of electric field E_x along X-axis.

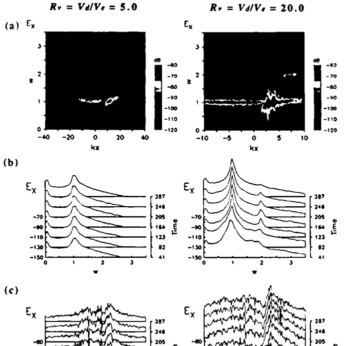

Figure 4.7: Plasma waves in E_x (dB) in the simulation runs with $R_v = V_d/V_e =$ 5.0 (left) and 20.0 (right), keeping $R_m = 1/1600$ and $R_n = 0.02$. (a) the ω-k_x diagram in t = 82–246; (b) evolution of plasma waves in ω space; (c) that in k_x space with ω = 0.5–2.5 in E_x and ω = 1.75–2.25 in B_z.

field. Total energy of electric field reaches 10 times of that of the standard case, while kinetic energy of beam components is only 4 times.

Figure 4.7 shows evolution of plasma waves in electric field E_x generated in both cases. In the case of R_v = 5.0, there is only weak beam-excited Langmuir waves on the Langmuir branch $\omega^2 = \Pi_e^2 + (3/2)k^2V_e^2$, at $k_x > +10.0 = \Pi_e/V_d$ with broad bandwidth. Amplitude of Langmuir wave is generally constant till the end of the simulation run. Electrostatic $2f_p$ waves are not found in any plots. On the other hand, in the case of $R_v = 20.0$, we can find strong enhancement of beam-excited Langmuir waves at $k_x > +2.5 = \Pi_e/V_d$ with sharp bandwidth, and clear electrostatic $2f_p$ waves at $k_x \sim 2k_L$. These results support the idea which is already suggested that amplitude of intense beam-excited Langmuir waves is strongly correlated with that of electrostatic $2f_p$ waves,

4.2.4 Contribution of beam density ratio

Finally, we vary the beam density ratio, $R_n = n_b/(n_e + n_b)$, to study contribution of density of beam electrons which divide physical process of wave–particle interaction into the thin-beam instability and the two-stream instability. We change $R_n = (0.005, 0.01, 0.02, 0.04, 0.08, 0.16)$, keeping $R_m = 1/1600$ and $R_v = 10.0$. Since the case with $R_n = 0.02$ was already indicated as the standard case, we show the cases with $R_n = 0.04$ and 0.08. The former shows upper limit of the thin-beam approximation, and while the latter shows lower limit of the two-stream approximation [cf. *Kainer et al.*, 1977].

Between both cases, evolution of the instability is rather different. Figure 4.8 (a) shows phase diagrams of particles in x-v_x space. In the case of $R_n = 0.04$, periodic vortices of beam electrons are formed at the initial stage. On the other hand, in the case of $R_n = 0.08$, the vortices are rather random. Differences also appear in evolution of total energy and spatial structure of electric field indicated in Figure 4.8 (b) and (c). In the case of $R_n = 0.04$, total energy of electric field is about the twice of that of the standard case with half beam density, and growth and decay features are similar in both cases. On the other hand, in the case of $R_n = 0.08$, total energy of electric field is about the twice of the case with $R_n = 0.04$, but the decay is much faster than the case of $R_n = 0.02$ and $R_n = 0.04$.

Figure 4.9 shows evolution of plasma waves in electric field E_x generated in both cases. In the case of $R_n = 0.04$, intense beam-excited Langmuir waves are found on Langmuir branch $\omega^2 = \Pi_e^2 + (3/2)k^2V_e^2$, and electrostatic $2f_p$ waves are also found at $k_x = 2k_L$. On the other hand, in the case of $R_n = 0.08$, beam-excited Langmuir waves are merged with electrostatic waves extending below and above the plasma frequency of background electrons. Therefore, electrostatic waves around plasma frequency have broad distributions in both ω and k_x spaces. Peak amplitude of Langmuir wave becomes lower than the case of $R_n = 0.04$ (Figure 4.9 (b) and (c)). Related with such broad distributions, electrostatic $2f_p$ waves are not found in all plots, which is because of lower amplitude of Langmuir wave and/or contamination of large perturbations of electric field above Π_e.

These results indicate that sharp and strong Langmuir waves excited by relative thin beam component is essential for excitation of high-k_x electrostatic $2f_p$ waves.

4.3 2D simulations

In 1D systems, we can not find excitation electromagnetic $2f_p$ waves. This suggests that numerical simulation on 2D systems is essential to produce electromagnetic $2f_p$

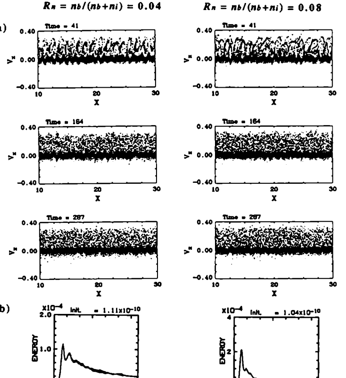

Figure 4.8: Evolution of particles and electric field in the simulation runs with $R_n = n_b/(n_e + n_b) = 0.04$ (left) and 0.08 (right), keeping $R_m = 1/1600$ and R_v = 10.0. (a) Phase diagrams of particles in x-v_x; (b) Total energy of electric field; (c) Spatial structure of electric field E_x along X-axis.

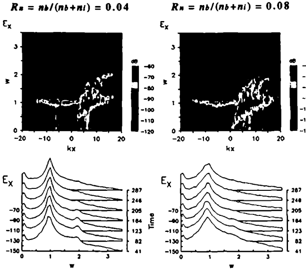

Figure 4.9: Plasma waves in E_x (dB) in the simulation runs with $R_n = n_b/(n_e+n_b)$ = 0.04 (left) and 0.08 (right), keeping $R_m = 1/1600$ and $R_v = 10.0$. (a) the ω-k_x diagram in t = 82-246; (b) evolution of plasma waves in ω space; (c) that of k_x space.

Parameter	Values
Grid spacing Δx, Δy	0.04
Time step Δt	0.02
Number of grid points $N_x \times N_y$	1024×256
Number of time steps N_t	16384
Number of background electrons per cell	16
Number of background ions per cell	16
Number of beam electrons per cell	4
Light speed c	1.0
Electron plasma frequency Π_e	1.0
Electron gyrofrequency Ω_e	$0.01\Pi_e$
Electron thermal velocity V_e	$0.04c$
Beam thermal velocity V_b	V_e
Electron to ion mass ratio $R_m = m_e/m_i$	1/1600
Ion plasma frequency $\Pi_i = (m_e/m_i)^{-1/2}\Pi_e$	0.025
Ion thermal velocity $V_i = (m_e/m_i)^{-1/2}V_e$	$0.001c$
Beam drift velocity ratio $R_v = V_d/V_e$	10
Beam density ratio $R = n_b/(b_e + n_i)$	0.02

Table 4.2: Parameters for 2D simulations

waves in the computer space because radiation pattern of $2f_p$ radiation is not necessarily parallel to the electron beams. However, 2D simulations require a number of computational compromises, even on a large supercomputer. For limitation of memory space and length of run time, we need to decrease scale of system and number of particles in a cell.

In this section, we use electromagnetic particle code, KEMPO [*Matsumoto and Omura*, 1985], for a two-dimensional periodic system with three species of charged particles; background electrons, background ions, and thin beam electrons whose densities are n_e, n_i, and n_b, respectively ($n_e + n_b = n_i$). All simulation parameters are listed in Table 4.2. For enlargement of Debye length to save memory size and length of simulation run, we further increase thermal velocity of background electrons, $V_e \sim 0.04c$. We set X-axis parallel to the magnetic field and drift velocity of beam electrons, as $1024\lambda_D$ with 1024 grid points, and Y-axis as $256\lambda_D$ with 256 grid points. Since length of system and simulation run is 40.96×10.24 (1024×256 grids) and 327.68 (16384 counts), we can produce plasma waves with wave number along X-axis below 79 (resolution: 0.154), wave number along Y-axis below 79 (resolution: 0.616), and frequency below 157 (resolution: 0.019), respectively.

In the simulation run, we select as electron to ion mass ratio $R_m = m_e/m_i = 1/1600$, beam drift velocity ratio $R_v = V_d/V_e = 10.0$, and beam density ratio $R_n = n_b/(n_e + n_b) = 0.02$.

Figure 4.10 shows velocity distributions of particles and total energy of electric field to indicate evolution of instability in particle distributions. Basic evolution of particle distributions and electric field are generally common with results of the standard case in 1D simulation. We find that vortices are formed by trapping of beam electrons at the initial stage. These structures are gradually disordered, and effective velocity of beam electrons gradually decreases. Background electrons are modulated accompanied with

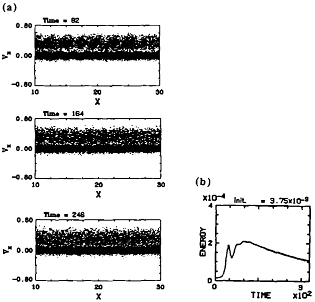

Figure 4.10: Evolution of particles and electric field in the 2D simulation run with $R_m = 1/1600$, $R_v = 10.0$, $R_n = 0.02$. (a) Phase diagrams of particles in x-v_x; (b) Total energy of electric field;

formation of vortices at the initial stage. On the other hand, total energy of electric field shows exponential growth at the initial stage till $t = 50$, and oscillation caused by exchange of energy with electron in $t = 50$–150. After $t = 150$, the total energy shows monotonous decrease by heating of particles via scattering by background ions.

Figure 4.11 shows evolution of plasma waves in electric field E_x (left) and magnetic field B_z (right) generated in these processes. Figure 4.11 (a) and (b) shows the ω-k_x diagram along X-axis and Y-axis in $t = 82$–246, obtained by Fourier transforming in space and time. We can find enhancement of beam-excited Langmuir waves at $\omega \sim 1.0 = \Pi_e$ and $k_x \sim +2.5(=\Pi_e/V_d)$ - $+5.0$, and weaker backscattered Langmuir waves at $\omega \sim 1.0 = \Pi_e$ and $k_x \sim -5.0$ - 0.0. We can also find weaker electrostatic $2f_p$ waves at $\omega \sim 2.0 = 2\Pi_e$ and $k_x \sim 2k_L$, where k_L is the wave number of Langmuir wave [cf. *Klimas*, 1983]. Since these electrostatic waves are concentrated to the region close to $k \sim 0$ in left panel of Figure 4.11 (b), we can conclude that the k vectors of these electrostatic waves are generally along the X-axis. In addition, We do not identify electrostatic $2f_p$ quasi-mode at low-k_x predicted by *Yoon et al.* [1994].

On the other hand, we can identify electromagnetic $2f_p$ waves in B_z of Figure 4.11 (a) and (b), at frequency of 2Π and at wave number from -2 to $+2$. Such components can be superposed on electromagnetic branch propagating on the X-Y plane. This is electromagnetic $2f_p$ radiation generated in the computer space by full electromagnetic particle code. We should compare relation between electrostatic and electromagnetic $2f_p$ waves generated in this system. Figure 4.11 (c) and (d) show evolution of plasma waves in ω and k_x space, respectively. We confirm the results of 1D simulations that amplitude of electrostatic $2f_p$ waves in E_x is enhanced after the end of initial stage and decreases after $t \sim 200$, associated with decay of beam-excited Langmuir waves. On the contrary, amplitude of electromagnetic $2f_p$ waves in B_z is gradually enhanced after $t \sim 100$, and do not show decrease till the end of simulation run. We should pay attention that such growth feature is similar to that of backscattered Langmuir waves indicated in Figure 4.11 (d). This favors the theory of direct conversion mechanisms of electromagnetic $2f_p$ waves by three-wave process.

4.4 Discussions

We summarize the results of 1D simulation runs in Figure 4.12. Although we can not generate the electromagnetic $2f_p$ waves in 1D systems, we generate the electrostatic $2f_p$ waves in the computer space. Such electrostatic $2f_p$ waves are generated at wave number of $k_x \sim 2k_L$ [*Klimas*, 1983]. Typical ratio of the amplitude of electrostatic $2f_p$ waves to that of Langmuir waves in our simulation runs is below -40 dB. This is consistent with in-situ observations of local enhancement of $2f_p$ waves observed at leading edge of the electron foreshock presented in Chapter 3. We also found that intensity of electrostatic $2f_p$ waves are strongly correlated of amplitude of Langmuir waves. Therefore, backscattering of Langmuir waves, too small beam drift velocity, and too large beam density do not favor generation of electrostatic $2f_p$ waves since these conditions suppress peak amplitude of beam-excited Langmuir waves. Namely, thin and high energy beam component thrown into the cold plasma is the most favorable

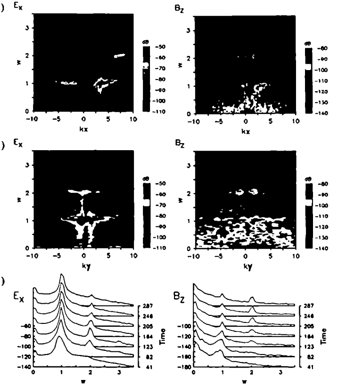

Figure 4.11: Plasma waves in E_x (left) and B_z (right) in the 2D simulation run with $R_m = 1/1600$, $R_v = 10.0$, $R_n = 0.02$. (a) the ω-k_x diagram along X-axis in t = 82-246; (b) the ω-k_y diagram along Y-axis in t = 82-246; (c) evolution of plasma waves in ω space; (d) that in k_x space with ω = 0.5-2.5 in E_x and ω = 1.75-2.25 in B_z.

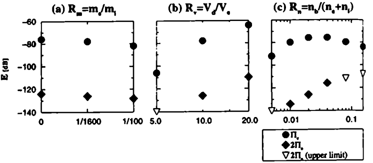

Figure 4.12: Electric field amplitude in dB of Langmuir waves at Π_e (circle) and electrostatic $2f_p$ waves at $2\Pi_e$ (diamond) in 1D simulation runs. Triangle-down indicates upper limit of electrostatic $2f_p$ waves. (a) Dependence on $R_m = m_e/m_i$; (b) Dependence on $R_v = V_d/V_e$; (c) Dependence on $R_n = n_b/(n_e + n_i)$.

to enhance the electrostatic $2f_p$ waves. Such condition is satisfied at leading edge of the electron foreshock, we need careful investigation of the plasma wave features at this region to search enhancement of the electrostatic $2f_p$ waves by instruments with larger dynamic range. On the other hand, we can not find any $2f_p$ mode at smaller wave numbers. This might be because distribution of backscattered Langmuir waves in k space is not narrow, which is required to produce such quasi-mode at $2f_p$ [*Yoon et al.*, 1994].

In 2D system, we succeed to generate electromagnetic $2f_p$ waves. We found that amplitude of electromagnetic $2f_p$ waves is enhanced associated with growth of backscattered Langmuir waves. This favors the theory of direct conversion mechanism of electromagnetic $2f_p$ waves by three-wave process. Here, we evaluate typical growth time and amplitude of electromagnetic $2f_p$ waves. First, we evaluate typical growth time of the electromagnetic $2f_p$ waves, about 200-400/Π_e. In the solar wind, plasma frequency is typically ~30 kHz, and $1/\Pi_e \sim 10^{-5}$ sec. Therefore, expected growth time of electromagnetic $2f_p$ waves suggested by this simulation run is about 2-4 msec in the solar wind condition. Since typical velocity of beam electrons at leading edge of the electron foreshock is about 3000-30000 km/s, typical scale length for generation of electromagnetic $2f_p$ waves is less than 0.02 R_E. This value does not contradict to thickness of the electron foreshock, $\ll 1$ R_E, suggested in Chapter 3, and favors the idea that the $2f_p$ radio source is at leading edge of the electron foreshock. Next, we evaluate typical ratio of amplitude of electromagnetic $2f_p$ waves to that of Langmuir waves, below -80 dB. Such weak waves is not large enough to contribute to local enhancement of $2f_p$ waves observed at leading edge of the electron foreshock. Here, we roughly estimate the coefficient of direct conversion of electromagnetic $2f_p$ waves by wave–wave coupling between beam-excited Langmuir waves and backscattered Langmuir waves. Proposed three-wave processes suggests positive correlation between amplitude of generated $2f_p$ radiation and product of amplitudes of beam-excited and backscattered Langmuir waves. For simplification, we define the conversion coefficient, α, by

$$E(2f_p) = \alpha E(L_{beam}) \times E(L_{back}) \quad (4.5)$$

where $E(2f_p)$, $E(L_{beam})$, and $E(L_{back})$ are electric field of electromagnetic $2f_p$ waves, beam-excited Langmuir waves, and backscattered Langmuir waves, respectively. Figure 4.11 shows that at $t = 287$, $E(2f_p)$, $E(L_{beam})$, and $E(L_{back})$ are -160, -80, and -110 dB, respectively. (Since ϵ_0 and μ_0 are unity in our simulation runs, energy scale of electric field and magnetic field are same in electromagnetic waves.) In this case, the conversion coefficient α is $\sim 10^3$. However, since our simulation system is periodic, electromagnetic waves in a frequency above f_p are trapped in the system. Therefore, local amplitude of electromagnetic waves is the sum of locally generated waves and propagated waves from distant source. We need to refine the simulation systems by free boundary systems to evaluate the correct efficiency to examine existing theories of generation mechanism of $2f_p$ radiation.

4.5 Conclusion

In this study, we execute numerical simulations in 1D and 2D periodic systems to generate electrostatic and electromagnetic $2f_p$ waves by the electromagnetic particle code, KEMPO.

In the 1D periodic systems, we generate electrostatic $2f_p$ waves at $\omega \sim 2\omega_L$ and $k \sim 2k_L$ where ω_L and k_L are frequency and wave number of beam-excited Langmuir wave. The electrostatic $2f_p$ waves are generated after the end of initial stage, and independent of Langmuir waves backscattered off by thermal ions. Since amplitude of electrostatic $2f_p$ waves is strongly correlated with peak amplitude of Langmuir waves in ω-k space, dense beam with $n_b > 0.04n_e$ and slow beam with $V_d < 5.0V_e$ do not favor the generation. Such features support the generation process of electrostatic $2f_p$ waves by wave–wave coupling of two of beam-excited Langmuir waves. Typical intensity ratio of electrostatic $2f_p$ waves to Langmuir waves is below -40 dB, which is consistent with values observed at leading edge of the electron foreshock presented in Chapter 3.

In the 2D periodic system, we also generate electrostatic $2f_p$ waves, and confirm the results obtained in the 1D systems. In addition, we generate electromagnetic $2f_p$ waves at $\omega \sim 2\omega_L$ and $k \sim \pm 2\Pi_e/c$. Amplitude of electromagnetic $2f_p$ waves are strongly correlated with growth of backscattered Langmuir waves and independent of electrostatic $2f_p$ waves. Such features support the generation process of electromagnetic $2f_p$ waves by wave–wave coupling of beam-excited and backscattered Langmuir waves through three-wave process. Typical growth time of electromagnetic $2f_p$ wave is about 200–400/Π_e. This value does not contradict to thickness of the electron foreshock. On the other hand, typical intensity ratio of electromagnetic $2f_p$ waves to Langmuir waves is below -80 dB. This value is too weak to detect enhancement of $2f_p$ waves at the leading edge of the electron foreshock.

We need to refine numerical simulations executed in this chapter, especially in 2D system. We should improve our works at four points; increase of time scale to follow variation of waves with small growth rate, increase of number of particles to suppress noise level and numerical heating, parameter survey of 2D systems which are executed in 1D systems, and introduction of spatial fluctuations to investigate mode-conversion processes. In order to evaluate these results, we need to introduce free boundary systems to evaluate correct efficiency of generation of electromagnetic $2f_p$ waves.

Chapter 5

Remote Observations of Nonthermal Continuum Radiation

We study continuum enhancement, short-lived enhancement of nonthermal continuum radiation, observed by the GEOTAIL spacecraft from November 1994 to December 1995. This radiation is generated at the nightside plasmapause by electrons injected into the local midnight zone associated with substorms. We use this radiation as a remote sensing probe for physical processes around the plasmapause during substorms.

We find that classical continuum generated at the dayside plasmapause is sometimes observed following the continuum enhancement. This indicates that both are generated by a series of injected electrons associated with the same substorm. Typical interval between the onset of both radiations is ~1 hour, which is consistent with the time lag expected from gradient and curvature drift motion of injected electrons. We also find that some of the continuum enhancement consist of 'fast' and 'main' components, which are distinguished by duration time and rising rate in frequency. We suggest that the fast component is generated first at the plasmapause in the local midnight zone by lower energy electrons, while the main component is later generated at the dawnside plasmapause by higher energy electrons.

On the other hand, we find that radial distance of the source on the plasmapause, estimated from spacing of banded frequency structure of the continuum enhancement, generally decreases with $-0.5 \sim -1.0R_E$/h for the first 1 hour after each substorms. Furthermore, we also find that radial distance of the source sometimes increases with $+0.1 \sim +0.5$ R_E/h for the next 1 hour associated with isolated substorms in relative quiet phase. The former suggests that long-term decrease of radius of the plasmapause can be separated into fast ones associated with substorms, while the latter suggests that short-term variations of radius of the plasmapause during each substorms is caused not only by the peeling off but also by compression and recovery of the plasmasphere.

5.1 Introduction: The continuum enhancement

Nonthermal continuum radiation is electromagnetic emission at frequencies from local plasma frequency to several hundred kHz, characterized by smooth variation in intensity and frequency continuing for several hours, and generated at geomagnetic equator of the plasmapause in 4-14h LT zone [*Gurnett and Shaw*, 1973; *Brown*, 1973; *Gurnett*, 1975]. 'Trapped component' below the solar wind plasma frequency, which is reflected at the magnetopause and confined to the magnetosphere, shows conglomerate broad band spectrum with low modulation index. 'Escaping component' above the solar wind plasma frequency, which can propagate outside of the magnetopause, shows banded frequency structure with large modulation index. [*Kurth et al.*, 1981]. Activity of the continuum radiation is positively correlated with large-scale geomagnetic storms for several days [*Gurnett and Frank*, 1976]. Here, we call this radiation as 'classical continuum'.

Classical continuum is believed to be generated through the linear mode-conversion process from electrostatic wave near upper hybrid frequency, f_{UHR} in a region with a large density variation [*Gurnett and Frank*, 1976; *Jones*, 1976; *Jones*, 1985]. At the plasmapause, electron plasma frequency, f_p, drops rapidly with increase radial distance, so that both production and propagation is favorable for the electromagnetic wave generated around f_{UHR}. Figure 5.1 (a) shows a magnetospheric model of the qualitative radial variation. At the plasmapause, f_{UHR} is close to f_p. Thus the frequency range of generated radiation indicates density in the source. On the other hand, at the plasmapause, electrostatic waves at f_{UHR} is enhanced with similar spacing of electron gyrofrequency, f_g, by strong upper-hybrid resonance at $(n+1/2)f_g$. Therefore, spacing of banded frequency structure of electromagnetic waves generated from such electrostatic waves indicates magnetic field strength in the source.

On the other hand, as shown in Figure 5.1 (b), there is other type of nonthermal continuum radiation associated well with each substorms. Here, we call this radiation as 'continuum enhancement'. Although the continuum enhancement is observed in the same frequency range with broad band or banded frequency structure as the classical continuum, this radiation has shorter duration for about few hours, and generated from the strong electrostatic waves driven by electrons injected into the local midnight zone associated with each substorms [*Gough*, 1982; *Filbert and Kellogg*, 1989]. This radiation is also thought to be generated at the plasmapause by the same mechanism as the classical continuum, so that its frequency and spacing of banded structure of should indicate density and magnetic field strength in the source illuminated by injected electrons. Furthermore, since magnetic field strength at the geomagnetic equator correlates well to radial distance from the Earth, the continuum enhancement can indicate radius of the source during substorms.

Actually, some of continuum enhancement show increase of frequency range and spacing of the banded structure. Such variation suggests increase of density and magnetic field strength at the plasmapause illuminated by injected electrons. There are two kinds of interpretation. One is inward motion of the plasmapause during each substorms as shown in Figure 5.2 (a) [*Gough*, 1982]. This is supported by steepening of the plasmapause associated with substorms. The other is dawnward motion of the source

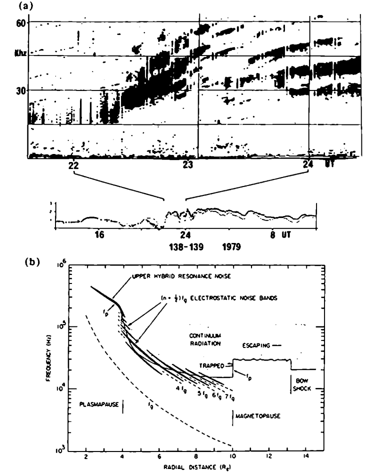

Figure 5.1: (a) A magnetospheric model showing the qualitative radial variation and region of occurrence of the electrostatic noise band and the continuum radiation at $(n+1/2)f_g$ [*Gurnett and Frank*, 1976]. (b) Spectrum of the continuum enhancement. Below is the count rate on logarithmic scales for electrons with 30–37 keV in perpendicular (circle) and parallel (dot) to local magnetic field [*Gough*, 1982].

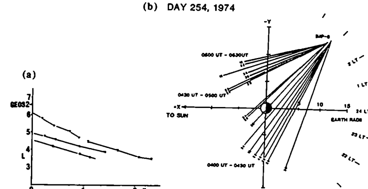

Figure 5.2: (a) Radial variation of the source deduced by the gyrofrequency at the source as a function of time after the energetic flux increases [*Gough*, 1982]. (b) Continuum source directions for three time intervals of the 0400 UT event on day 254, 1974. The small numbers at the end of the line segments label the frequency (kHz) [*Filbert and Kellogg*, 1989].

caused by gradient and curvature drift of injected electrons as shown in Figure 5.2 (b) [*Filbert and Kellogg*, 1989]. This is supported by asymmetry of radial profile of the plasmapause, i.e., smaller radius on the dawnside zone [cf. *Carpenter*, 1966].

Fortunately, we have large number of plasma wave data from November 1994 to December 1995 obtained by GEOTAIL, and find 138 events of the continuum enhancement. In this study, we analyze frequency-time structure and direction of the source of continuum enhancement, to get physical conditions in and motions of the source of the continuum enhancement by remote satellite observations. Furthermore, we try to get a concrete model of physical processes going around the plasmapause associated with substorms.

5.2 Analyzed data sets

The data sets analyzed in the present study are obtained from the PWI/SFA aboard GEOTAIL [*Matsumoto et al.*, 1994]. Since the continuum enhancement is observed above f_p (~5 kHz in the lobe, and ~30 kHz in the solar wind), we use the SFA Band-3 (1.67-12.5 kHz), Band-4 (12.5-100 kHz), and Band-5 (100-800 kHz) electric field data. Each receiver has the frequency resolution of 1/128 of its bandwidth (84.6 Hz in Band-3, 684 Hz in Band-4, and 5.47 kHz in Band-5) and the time resolution of 8 seconds.

The PWI is connected to two sets of electric dipole antenna systems, a wire dipole antenna (WANT) and a pair of top-hat probe antennas (PANT). Both antennas have 100 m tip-to-tip length, and are extended on the spin plane of the spacecraft which

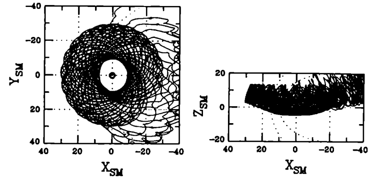

Figure 5.3: The Near-Tail orbit of the GEOTAIL spacecraft in the solar magnetic (SM) coordinates from November 1994 to December 1995. Left is a projection on X-Y plane. Right is a projection on X-Z plane.

is stabilized close to the ecliptic plane. During our observations the electric SFA has generally been connected to the PANT system. The spin period is ~3 seconds, and we can define k-vector of the electromagnetic waves projected on the ecliptic plane by spin modulations of observed electric field strength.

We use data set observed from November 1994 to December 1995. Figure 5.3 shows trajectories of GEOTAIL in the solar magnetic (SM) coordinates. In this term, GEOTAIL is on the Near-Tail orbit which covers whole hours in MLT and $+40° \sim -40°$ in magnetic latitude. This orbit has an apogee of ~30 R_E, a perigee of ~10 R_E, and the orbital period of ~7 days after February 1995.

In Figure 5.4, we summarize observed locations of analyzed samples of the classical continuum and the continuum enhancement by two methods. Figure 5.4 (a) shows observed locations of both radiations at 1-hour intervals on the SM coordinates. Figure 5.4 (b) shows number of occurrence of both radiations classified by observed magnetic local time. Samples are picked out from frequency-time diagrams of the PWI/SFA from November 1994 to December 1995. Figure 5.4 shows that the classical continuum is mainly observed on the late dawnside or dayside zone, while the continuum enhancement is mainly observed on the nightside or early dawnside zone. Both types are observed on the dawnside zone.

5.3 Correlation with the classical continuum

In this section, we pay attention to correlation between the classical continuum and the continuum enhancement. In Figure 5.5 (a)-(c), we show typical frequency-time diagrams of the classical continuum and the continuum enhancement observed by the PWI/SFA. X-axis is observed time in UT, and Y-axis is frequency in kHz in a quasi-

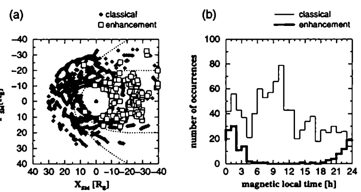

Figure 5.4: (a) Observed locations of the classical continuum and the continuum enhancement on the SM coordinates identified in 1-hour intervals from November 1994 to December 1995. Diamonds is the classical continuum, and squares is the continuum enhancement. (b) The number of occurrence classified by observed magnetic local time (MLT). Thin and thick lines are the number of occurrence of the classical continuum and the continuum enhancement, respectively.

linear format with two linear diagrams divided at 100 kHz. above 100 kHz constructed by Band-5 data and below 100 kHz constructed by Band-3/4 data, respectively. Each observed locations is also indicated in (d).

Figure 5.5 (a) shows the classical continuum observed in 0-2h and 5-10h UT on 6 April 1995 when GEOTAIL is on the dayside zone. The classical continuum generally covers from local f_p to 100-500 kHz, and lasts for 2-12 hours with smooth variation in intensity and frequency. This radiation sometimes looses lower frequency component below 2-4f_p in solar wind. It seems to be caused by reflection and refraction at the magnetopause and the bow shock.

Figure 5.5 (b) shows the continuum enhancement observed in 13-14h, 15-16h, and 19-21h UT on 31 December 1995 when GEOTAIL is on the nightside zone. The continuum enhancement generally covers from local f_p to 50-100 kHz, and only lasts for 1-3 hours. Frequency range of the continuum enhancement is common with low frequency AKR (LFR) [*Filbert and Kellogg*, 1989] and the LF band radio bursts [*Kaiser et al.*, 1996]. Because activities of these radiations are also correlated well with substorms, continuum enhancements are frequently contaminated by them. However, since LFR and the LF bursts have much shorter duration, we can independently trace power flux of the continuum enhancement with longer duration and smooth variation.

On the other hand, We can sometimes observe the classical continuum following the continuum enhancement when GEOTAIL is in the dawnside zone. Figure 5.5 (c) shows such case observed in 3-9h UT on 23 January 1995. In this case, the continuum enhancement beginning at 3h UT is naturally connected with the classical continuum

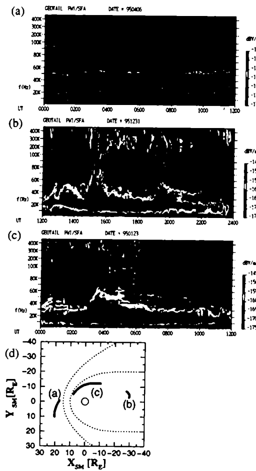

Figure 5.5: Frequency-time diagrams observed by the PWI/SFA: (a) Classical continuum observed in 0–2h and 5–10h UT on 6 April 1995; (b) Continuum enhancement observed in 13–14h, 15–16h, and 19–21h UT on 31 December 1995; (c) Mixed type observed in 3–9h UT on 23 January 1995; (d) Observed locations on the SM coordinates.

in both intensity and frequency. Such cases suggest that the continuum enhancement and the classical continuum are a series of same phenomena.

Simultaneous observation of the two spacecraft staying in the nightside and dayside zone provides a good example describing relation between both radiations. Figure 5.6 shows frequency-time diagrams observed by GEOTAIL PWI and WIND WAVES on 17 November 1994, when GEOTAIL stayed in the early morning zone and WIND stayed in the late morning zone, respectively. GEOTAIL observed beginning of a continuum enhancement at ~4h UT and end at ~7h UT. On the other hand, WIND observed beginning of a classical continuum at ~5-6h UT just following disappearance of the continuum enhancement in the upper panel. Such a relation suggests an idea that GEOTAIL and WIND observed the former half and the latter half of a series of the same event occurred at the nightside and dayside plasmapause, respectively.

Features shown in Figure 5.4, Figure 5.5, and Figure 5.6 indicate that the continuum enhancement and the classical continuum are a series of a same events generated at opposite sides of the plasmapause. The most possible origin of such relation is that both radiations are generated by the a group of electrons which is injected into the nightside zone during the same substorm and shows dawnward drift motion. A part of injected electrons first arrives at nightside of the plasmapause and generates the continuum enhancement, while the other part later arrives at dawnside/dayside of the plasmapause and generates the classical continuum. Typical interval between the onset of both radiations is about 1 hour, which is consistent with time lag expected from gradient and curvature drift of injected electrons [cf. *Filbert and Kellogg*, 1989].

5.4 Correlation with geomagnetic activities

Next, we investigate correlation between the continuum enhancement and geomagnetic activity. Because we are not able to use auroral electrojet (AE) index in 1994-1995, we use AKR index, flux of AKR normalized at a distance of 25 R_E from the Earth in 1-minute interval as an indicator for geomagnetic activity [*Murata*, 1995; *Murata et al.*, 1997]. Figure 5.6 shows that beginning of the continuum enhancement at ~4h UT and peak of AKR index is generally at the same time. Since rapid increase of AKR index is well correlated with the onset of each substorms, correlation between the continuum enhancement and AKR index is well consistent with the idea that the continuum enhancement is generated by electrons injected at the onset of each substorms. Such mechanism suggests that power flux of the continuum enhancement reflects amount of injected particles with each substorms [cf. *Filbert and Kellogg*, 1989].

In Figure 5.7, we compare the maximum flux of the continuum enhancement and peak of AKR index in each continuum enhancement events. We normalize flux of the continuum enhancement at a distance of 25 R_E from the Earth by an r^{-2} law, in the same definition as that of AKR index. We traced power flux of the continuum enhancement with relative smooth variation, and avoid contamination of AKR, LFR, and LF bursts with more rapid variation.

In spite of large scattering, which is partly caused by intense AKR not accompanied the continuum enhancement as shown by an event at ~6h UT in Figure 5.6, AKR index

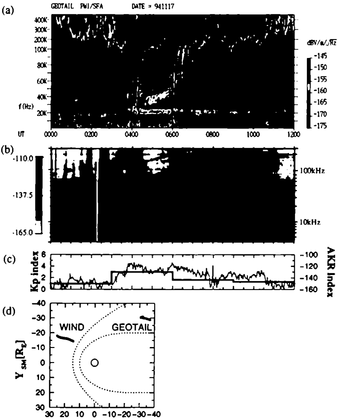

Figure 5.6: Continuum enhancement and classical continuum simultaneously observed by GEOTAIL and WIND on 17 November 1994: (a) Frequency-time diagram observed by GEOTAIL PWI/SFA; (b) Frequency-time diagram observed by WIND WAVES/TNR; (c) Kp index (thick line) and AKR index (thin line); (d) Observed location on the SM coordinates.

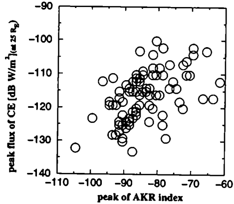

Figure 5.7: Peak of AKR index and the maximum flux of the continuum enhancement normalized at a distance of 25 R_E from the Earth, in each continuum enhancement.

and power flux of the continuum enhancement is positively correlated. Regression line is indicated by

$$F_{CE} = -0.46(I_{AKR} + 86.1) - 116.6 \tag{5.1}$$

where I_{AKR} is peak of AKR index and F_{CE} is the maximum flux of the continuum enhancement normalized at a distance of 25 R_E from the Earth. Correlation coefficient of (5.1) is 0.50. Taking account of lack of the best way to get gross amount of injected electrons, power flux of the continuum enhancement might be able to provide valuable information.

5.5 Variation of frequency range

Next, we analyze frequency range of the continuum enhancement to investigate density in the source. In Figure 5.8 and Figure 5.9, we show typical spectra of the continuum enhancement observed on 2 September and 8 December 1995. Figure 5.8 and Figure 5.9 show two typical components which have different duration and rising rate in frequency; 'fast component' and 'main component'. The fast component has duration of ~30 minutes and rising rate in frequency of 50-100 kHz/h. The main component has duration of ~1-3 hours and rising rate in frequency of 10-20 kHz/h. Since spacing of banded frequency structure, f_{sp}, is generally continuous in both components, electron gyrofrequency in both sources are not seriously different. This means that radial distances of the sources of both components are common, and that both components are generated at regions close to each other especially in the beginning phase. On the other hand, we should mention that all the continuum enhancement do not always have both components. For example, although components are divided clear at an event from 12h

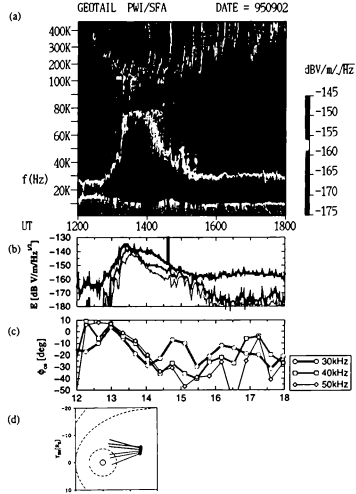

Figure 5.8: Continuum enhancement in 13-16h UT on 2 September 1995: (a) Frequency-time diagram of the PWI/SFA; (b) Flux and (c) azimuth angle (ϕ_{ce}) at 30, 40, and 50 kHz in 20-minute interval. Origin of ϕ_{ce} is direction of the Earth; (d) Observed location and azimuth angle ϕ_{ce} at 40 kHz from 13-15h UT on the SM coordinates.

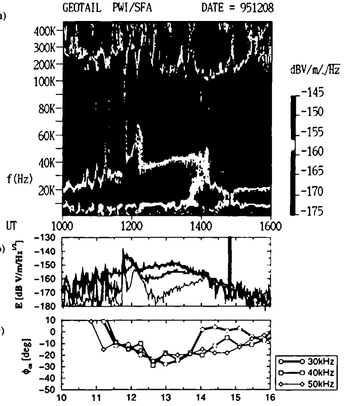

Figure 5.9: Continuum enhancement observed in 12–15h UT on 8 December 1995. (a) Frequency-time diagram of the PWI/SFA; (b) Flux and (c) azimuth angle (ϕ_{ce}) at 30, 40, and 50 kHz in 20-minute interval. Origin of ϕ_{ce} is direction of the Earth; (d) Observed location and azimuth angle ϕ_{ce} at 40 kHz from 12–14h UT on the SM coordinates.

UT in Figure 5.9, both are not clear at an event from 13h UT in Figure 5.8. There are also many events which have only one of the fast or main components.

In order to identify motion of the source associated with spectral variation, we evaluate direction of the source in each continuum enhancement events. Majority of the continuum enhancement show distinct spin modulation of received signals above f_p in the solar wind (~30 kHz). Therefore, we can define direction of the source projected on the ecliptic plane by direction finding methods with standard Fourier techniques [cf. *Manning and Fainberg*, 1980]. Here, we get azimuth angle of direction of the source, ϕ_{cc}, at 30, 40, and 50 kHz in 20-minute intervals. Origin of ϕ_{cc} is defined as Earthward direction. Decrease of ϕ_{cc} after the onset in both Figure 5.8 (d) and Figure 5.9 (d) show dawnward rotation of the source. Although variation of the power flux is rather different with frequencies, Figure 5.8 and Figure 5.9 show that the dawnward rotation at all frequencies are in the same manner converged within ±10°. At the beginning of the continuum enhancement, ϕ_{cc} is generally close to 0°, so that whole radiation comes from the local midnight zone of the plasmapause. In first 0.5-1 hours after the onset, the bright fast component is dominant with gradual dawnward rotation of ϕ_{cc} at 30-50 kHz. In next 1-3 hours, the dimmer main component is dominant with continuous dawnward rotation of ϕ_{cc}. No abrupt gap of ϕ_{cc} between the fast and main components suggests that both components seem a series of the same phenomena occurred at the source showing continuous motion. This is also consistent with continuous variation of spacing of banded structure between both components. Such rotational motion of ϕ_{cc} is explained by Earthward motion caused by steepening of the plasmapause [*Gough*, 1982] or by dawnward motion caused by gradient/curvature drift [*Filbert and Kellogg*, 1989]. In our observation, observed rotation of ϕ_{cc} is usually dawnward without no clear relation with location of the spacecraft, in the nightside and dawnside zone at a distance of 10-30 R_E from the Earth. This favors the latter explanation, by dawnward motion of the source.

In Figure 5.10, we summarize variations of ϕ_{cc} at 40 kHz classified by Kp index; (a) $Kp < 2$, (b) $2 \leq Kp < 3$, (c) $3 \leq Kp < 4$, and (d) $4 \leq Kp$. X-axis is time after the onset of each substorms which is defined by peak of AKR index. Y-axis is the apparent distance of the source from the Earth, R_a, which is defined by

$$R_a = R_G sin(-\phi_{cc}) \tag{5.2}$$

where R_G is the distance of GEOTAIL from the Earth. We plot 48 samples observed in the local midnight zone (20h<MLT<2h) which show continuous variations of ϕ_{cc} for >1 hour after the onset. Therefore, R_a indicates the apparent distance of the source projected on Y-Z plane of the SM coordinates. Decrease/increase of R_a means duskward/dawnward motion of the source regions. Figure 5.10 shows that dawnward motion of the source is common in various Kp. Typical duration of dawnward motion is about 1 hour. However, we should pay attention to the fact that some R_a reach 10-20 R_E, fur outside of the plasmapause with a distance of about 5 R_E. The most possible cause is mixing of the classical continuum, which sometimes appears after the continuum enhancement, reflected at the dawnside magnetopause or the bow shock. Actually, it seems supported by some cases with small dawnward motion (3-5 R_E) especially in small Kp, when activity of the classical continuum is weak enough. On

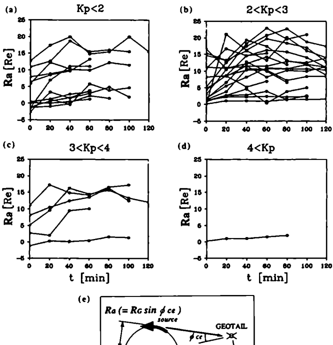

Figure 5.10: Variations of azimuth angle (ϕ_{ce}) classified by Kp index; (a) $Kp < 2$, (b) $2 \leq Kp < 3$, (c) $3 \leq Kp < 4$, and (d) $4 \leq Kp$. X-axis is time after the onset of each substorms. Y-axis is the apparent distance of the source (R_a) defined from ϕ_{ce}. Concept of relation between R_a and ϕ_{ce} is indicated in (e).

the other hand, we can not reject the possibility of some radiations generated at the dawnside magnetopause.

5.6 Variation of banded frequency structure

Next, we analyze banded frequency structure of the continuum enhancement to investigate magnetic field strength in and radial distance of the source. Figure 5.5 (b)-(c), Figure 5.8 and Figure 5.9 indicate that spacing of banded frequency structure, f_{sp}, is independent to variation of general frequency range. We assume that f_{sp} approximately indicates f_g in the source. Therefore, we can convert f_{sp} to the radial distance of the source on the magnetic equator, R_s in R_E, based on an assumption of dipole-like magnetic field by

$$R_s = (f_{g0}/f_{sp})^{1/3} \tag{5.3}$$

where $f_{g0} = 870$ kHz is electron gyrofrequency on the surface of Earth at the equator.

Figure 5.11 and Figure 5.12 show two samples of variation of f_{sp} observed by the PWI/SFA on 14 November and 5 December 1994. Kp/AKR index, ϕ_{cc}, and R_s are also indicated. Series of the continuum enhancements are found at 15-16h, 17-18h, 21-22h UT in Figure 5.11, and at 9-11h, 12-14h, 15-17h UT in Figure 5.12. In Figure 5.11 (d) and Figure 5.12 (d), R_s not only decreases associated with each substorms with $-0.5 \sim -1$ R_E/h for the first 1 hour after the onset of the continuum enhancement, but also continuously decreases through the subsequent events. In Figure 5.11 (c) and Figure 5.12 (c), each continuum enhancements comes from a region close to the local midnight zone at the beginning phase, so that we suggest that the radial distance of the plasmapause at local midnight gradually decreases for at least several hours On the other hand, we also point out that decrease of R_s is sometimes accompanied with decrease of ϕ_{cc}, i.e., dawnward motion of the source. Since radius of the plasmapause is smaller at dawnside than at the local midnight, dawnward motion of the source along the plasmapause may also contribute to decrease of the radius. Here, we call them as 'the shrinking case'.

On the other hand, we sometimes find increase of R_s for the next 1 hour. Figure 5.13 and Figure 5.14 show two samples observed by the PWI/SFA on 22 January and 9 May 1995. Kp/AKR index, ϕ_{cc}, and R_s are also indicated. Series of continuum enhancements are also found at 12-13h, 13-16h UT in Figure 5.13, and at 6-7h, 7-10h UT in Figure 5.14. In Figure 5.13 (d) and Figure 5.14 (d), R_s decreases associated with each substorms with $-0.5 \sim -1$ R_E/h for the first 1 hour after the onset of the continuum enhancement, and inversely increases with $+0.1 \sim +0.5$ R_E/h for the next $\sim$1 hour. In Figure 5.13 (c) and Figure 5.14 (c), ϕ_{cc} shows continuous variation between the end of the first decreasing phase and the beginning of the next increasing phase. Here, we call them as 'the oscillating case'.

Difference between 'the shrinking case' and 'the oscillating case' seems to be caused by duration and scale of geomagnetic activity. Actually, in the former case, Figure 5.11 and Figure 5.12 show that duration of AKR activities are over 7 hours and AKR index exceeds -140 dB. In contrast, in the latter case, Figure 5.13 and Figure 5.14 show that duration of AKR activities are less than 4 hours and AKR index generally does not

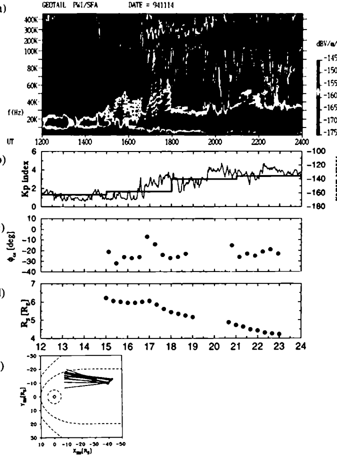

Figure 5.11: Continuum enhancement observed on 14 November 1994: (a) Frequency-time diagram of the PWI/SFA; (b) Kp index (thick line) and AKR index (thin line); (c) Azimuth angle (ϕ_{cc}) at 40 kHz; (d) Radial distance of the source (R_s); (e) Observed location and ϕ_{cc} at 40 kHz from 15-19h/21-23h UT on the SM coordinates.

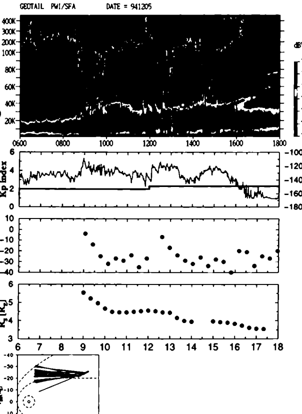

Figure 5.12: Continuum enhancement observed on 5 December 1994: (a) Frequency-time diagram of the PWI/SFA; (b) Kp index (thick line) and AKR index (thin line); (c) Azimuth angle (ϕ_{cc}) at 40 kHz; (d) Radial distance of the source (R_s); (e) Observed location and ϕ_{cc} at 40 kHz from 9–18h UT on the SM coordinates.

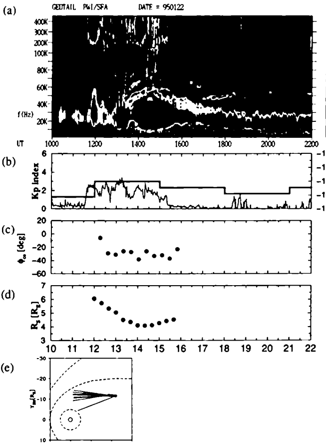

Figure 5.13: Continuum enhancement observed on 22 January 1995. (a) Frequency-time diagram of the PWI/SFA; (b) Kp index (thick line) and AKR index (thin line); (c) Azimuth angle (ϕ_{cc}) at 40 kHz; (d) Radial distance of the source (R_s); (e) Observed location and ϕ_{cc} at 40 kHz from 12-16h UT on the SM coordinates.

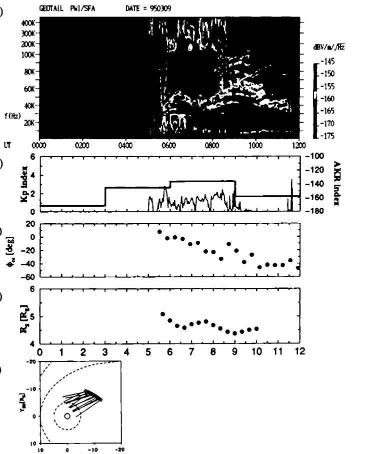

Figure 5.14: Continuum enhancement observed on 9 March 1995. (a) Frequency-time diagram of the PWI/SFA; (b) Kp index (thick line) and AKR index (thin line); (c) Azimuth angle (ϕ_{cc}) at 40 kHz; (d) Radial distance of the source (R_s); (e) Observed location and ϕ_{cc} at 40 kHz from 6–10h UT on the SM coordinates.

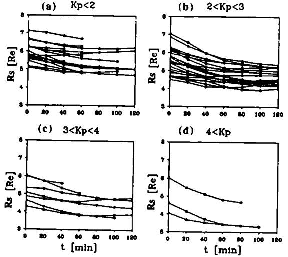

Figure 5.15: Variations of radial distance of the source from the Earth (R_s) classified by Kp index; (a) $Kp < 2$, (b) $2 \le Kp < 3$, (c) $3 \le Kp < 4$, and (d) $4 \le Kp$. X-axis is time after the onset of each substorms, and Y-axis is distance of the source from the Earth (R_s).

exceed ~ -140 dB. These features suggest that radius of the plasmapause is controlled by the average geomagnetic activities in long time scale, and fluctuated with each substorms in short time scale.

In Figure 5.15, we summarize variations of R_s classified by Kp index; (a) $Kp < 2$, (b) $2 \le Kp < 3$, (c) $3 \le Kp < 4$, and (d) $4 \le Kp$. We plot 52 samples that show clear banded structure. X-axis is time after the onset of each substorms which is defined by peak of AKR index. Y-axis is distance of the source from the Earth, R_s, defined from f_{sp}. Figure 5.15 indicates that R_s generally decreases at the first 1 hour from the onset. This is independent to scale of magnetic activity and value of R_s at the onset. After that, some with relative large radius show continuous decrease, while others with relative small radius show reversal increase. Typical scale of R_s variations is $-0.5 \sim -1.0$ R_E/h in the first 1 hour and $+0.5 \sim -0.5$ R_E/h in the next 1 hour. As things turned out, R_s settles to specific value related with average geomagnetic activity; 5-6 R_E in $Kp < 2$, 4.5-5.5 R_E in $2 \le Kp < 3$, 4-5 R_E in $3 \le Kp < 4$, and 3.5-4.5 R_E in $4 \le Kp$.

Before the finish of this section, we should add a comment on the continuum enhancement without banded structure. In Figure 5.16, we show number of occurrence of the continuum enhancement classified by Kp index (left Y-axis). Thin line indicates the

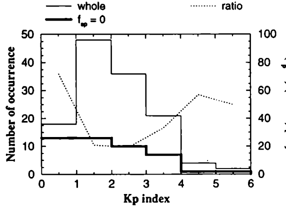

Figure 5.16: The occurrence of the continuum enhancement without banded structure. Left Y-axis is number of occurrence of the continuum enhancement classified by Kp index. Thin line indicates the whole samples. Thick line indicates events without banded structure. Right Y-axis is occurrence ratio of events without banded structure to the whole samples (dotted line).

whole samples, and thick line indicates events without banded structure. We also show occurrence ratio of events without banded structure to whole samples by dotted line (right Y-axis). Figure 5.16 indicates that the continuum enhancement without banded structure is evident in quiet phase ($Kp < 1$) or highly disturbed phase ($Kp > 4$). In quiet phase, it is probable that f_g in the source region is smaller than frequency resolution of the PWI/SFA because average radius of the plasmapause is large enough. When f_g at the plasmapause is lower than twice of the frequency resolution of Band-4, ~1.4 kHz (corresponding $R_s = 8.5\ R_E$), we should observe the continuum enhancement with no-banded structure. On the other hand, in the highly disturbed phase, radiations with different f_{sp} seem to be mixed because continuous electron injections simultaneously generate the continuum enhancements at different position of the plasmapause, whose radius is disturbed by continuous substorms. As a result, mixture of various radiations should erase clear banded structure if it exists in each radiations.

5.7 Discussions

In Figure 5.17, we summarize schematic models of the continuum enhancement presented by our observations. In order to interpret the observations, we need to know trajectories of electrons injected to the local midnight zone associated with each substorms. A injected electron moves to earthward by **E**×**B** drift proportional to dawn-to-dusk electric field and to dawnward by gradient/curvature drift proportional to kinetic

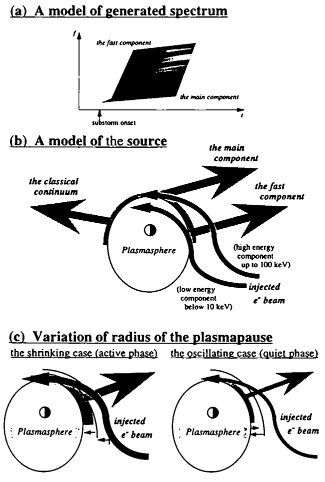

Figure 5.17: Models of observed features of the continuum enhancement. (a) A model of generated spectrum; (b) A model of the source; (c) A model of radial variation of the plasmapause indicated by the continuum enhancement.

energy of particles, so that typical azimuthal drift rate of injected electrons is positively correlated with kinetic energy of particles. Therefore, trajectories and arrival time of injected electrons are filtered by their kinetic energies: Lower energy electrons with small azimuthal drift velocity first arrive the plasmapause at a region close to the local midnight zone, while higher energy electrons with large azimuthal drift velocity later arrive the plasmapause at a more dawnward region [cf. *Maeda et al.*, 1978].

First, we examine the correlation between the classical continuum and the continuum enhancement. We can simultaneously observe the classical continuum and the continuum enhancement in two cases. In the first case, the classical continuum sometimes follows the continuum enhancement when the spacecraft stays in the dawnside zone. In the second case, the classical continuum observed by the spacecraft stayed in the dayside zone sometimes follows the continuum enhancement observed by the other spacecraft stayed in the nightside zone. We suggest as shown in Figure 5.17 (b) that a series of injected electrons associated with the same substorm generates the continuum enhancement first at the nightside/dawnside plasmapause and the classical continuum later at the dawnside/dayside plasmapause, respectively. In our observation, typical interval of the onset between both radiations is about 1 hour, which is consistent with the expected value by gradient and curvature drift motion of the injected electrons from the midnight to the dawnside zone [*Filbert and Kellogg*, 1989], Long duration of the classical continuum also agree with our model, because arrival time and position of these electrons to the plasmapause should be converged in the midnight zone but widely scattered in the dawnside/dayside zone.

Next, evaluate the variation of frequency range of the continuum enhancement, shown in Figure 5.17 (a), with the trajectories of injected electrons. At the onset of each substorms, electrons injected into the local midnight zone move to Earthward by **E**×**B** drift motion and dawnward by gradient/curvature drift. We propose as shown in Figure 5.17 (b) that the fast component of the continuum enhancement can be generated by lower energy electrons arrived first at the plasmapause in a region close to the local midnight zone, while the main component can be generated by higher energy electrons arrived later at the plasmapause in a more dawnward region, respectively. At the local midnight, lower energy electrons with small dawnward drift velocity can climb a density wall at the plasmapause in shorter time, so that f_p at the radiation source on the plasmapause illuminated by these electrons can increase rapidly. Therefore, radiation generated at such source can be identified as the fast component with short duration and fast rising rate in frequency. On the other hand, electrons with higher kinetic energy arrives the plasmapause later and at a more dawnward region, so that the brightest source of the continuum radiation shows slow dawnward motion. Therefore, radiation generated at such source can be identified as the main component with long duration and slow dawnward motion. There are three possible origins of its slow rising in frequency, i.e., slow rising of f_p at the source: The first is small earthward velocity of electrons. Trajectory of electrons in the dawnside zone is generally parallel to the plasmapause [cf. *Ejiri*, 1978], so that f_p at the electron cloud slowly increase associated with slow passage of electron cloud across the plasmapause. The second is larger density of the dawnward plasmapause, associated with decrease of radius in the dawnside hemisphere [cf. *Chappell et al.*, 1971]. At the source on the plasmapause, slow increase of f_p might be expected associated with its dawnward motion. The third is steepening of the plasmapause associated with each substorms [cf. *Chappell et al.*, 1970]. Since density at the plasmapause should increase associated with steepening of the plasmapause, slow increase of f_p might be expected at the source on the plasmapause. On the other hand, we should pay attention to a problem that this model does not indicate observed separation between the fast and main components. Such a feature might tell us depression of injected electrons at specific energy, biased distribution of trajectories of the injected electrons, or some irregularities of structure at the plasmapause.

Finally, we examine the variation of radial distance of the source, R_s, indicated by spacing of banded frequency structure, f_{sp}. Variations of R_s indicate that radius of the plasmapause illuminated by injected electrons decreases for the first 1 hour after the onset of each substorms, and is converged to specific values which is inversely correlated with average geomagnetic activities. It is known that density profile of the plasmapause is generally controlled by peeling off by magnetospheric convection and refilling by up-welling from the sub-auroral F-layer. The peeling off and the refilling in the outer plasmasphere occurs in a time scale of several hours and of several days, respectively. Therefore, the profile of the plasmapause contains the recent prehistory of the peeling off and the long prehistory of the refilling [cf. *Galperin et al.*, 1996]. An empirical L parameter of the plasmapause, L_{pp}, at 0–15h MLT is indicated by

$$L_{pp} = 5.6 - 0.46Kp' \quad (5.4)$$

where Kp' is maximum Kp value in last 24 hours [*Carpenter and Anderson*, 1992]. This equation indicates that radius of the plasmapause in long time scale is inversely correlated well with maximum Kp value in last 24 hours. Converged radius of the plasmapause shown in Figure 5.15 is 5-6 R_E at $Kp < 2$, 4.5-5.5 R_E at $2 \leq Kp < 3$, 4-5 R_E at $3 \leq Kp < 4$, and 3.5-4.5 R_E at $4 \leq Kp$, and agrees well with (5.4) though we use values of Kp index at observed time.

On the other hand, we find shorter variations of radius of the plasmapause associated with each substorms. Our observation suggests that radial distance of the source generally decreases with $-0.5 \sim -1$ R_E/h for the first 1 hour after the onset of each substorms independently, even in disturbed phase when substorms occurs one after another, as shown in Figure 5.11, Figure 5.12 and Figure 5.17 (c). This indicates the typical duration of strong peeling off of thermal plasma caused by magnetospheric convection associated with each substorms, so that long-term decrease of radius of the plasmapause in disturbed phase can be separated into each fast decrease during each substorms. Furthermore, we also find that radial distance of the source in the next 1 hour increases inversely associated with isolated substorms in relatively quiet phase, as shown in Figure 5.13, Figure 5.14 and Figure 5.17 (c). The increasing rate, $+0.1 \sim +0.5$ R_E/h, is slower than the decreasing rate in the first 1 hour, while this value is far larger than that expected from refilling rate of plasma up-welling from the sub-auroral F-layer. Therefore, we suggest that short-term variations of radius of the plasmapause during substorm is caused not only by the peeling off, but also by a compression and recovery of the plasmasphere associated with pressure variation in the inner magnetosphere. Confirmation and further investigation of such fast variations of the plasmasphere will be one of problems for future in-situ and imaging observations.

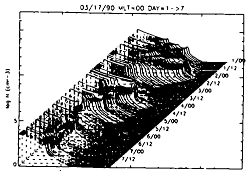

Figure 5.18: Empirical radial profiles of electron density in 0h MLT, calculated by CDPDM model with one hour step during a large magnetic storm on 17-23 March 1990 [*Galperin et al.*, 1996]. Day 1 is 17 March 1990.

5.8 Conclusion

In this study, we study the continuum enhancement and examine the possibility to use this radiation as a remote sensing tool for physical processes around the plasmapause during substorms. Summary of our observations is as follows:

(1) The continuum enhancement and following the classical continuum are generated by a series of injected electrons associated with the onset of the same substorm. Typical interval between the onset of both radiations is ~1 hour, which is consistent with the time lag expected from gradient and curvature drift motion of injected electrons.

(2) Some of the continuum enhancement consist of the fast and main components distinguished by duration time and rising rate in frequency. We suggest that the fast component is generated first at the plasmapause in the local midnight zone by lower energy electrons, while the main component is generated later on the dawnside plasmapause by higher energy electrons.

(3) Radial distance of the source on the plasmapause generally decreases with $-0.5 \sim -1.0 R_E$/h for the first 1 hour after each substorms. This suggests that long-term decrease of radius of the plasmapause can be separated into fast ones associated with each substorms. On the other hand, radial distance of the source sometimes increases with $+0.1 \sim +0.5$ R_E/h for the next 1 hour associated with isolated substorms in relative quiet phase. This indicates that short-term variations of radius of the plasmapause associated with each substorms is caused not only by the peeling off, but also by compression and recovery of the plasmasphere.

In this study, we show that the continuum enhancement can describe real-time global information around the plasmapause. For confirmation and further studies of present results, we hope simultaneous observations with other satellites or ground-based sites, and comparisons with empirical and MHD models. Since imaging techniques for the plasmasphere are not established yet, the continuum enhancement must function as a new tool to study global, fast and turbulent phenomena around the plasmapause during substorms.

Chapter 6

Remote Observations of Auroral Kilometric Radiation

We examine spectral variation and angular distribution of auroral kilometric radiation (AKR) for evaluation of the distribution of energetic electrons and the structure of the auroral plasma cavity above the auroral zone through remote satellite observations. We use a 38-month data set of plasma wave observations by the GEOTAIL spacecraft and mainly analyze AKR at 200 kHz and 500 kHz which are representative of radiation at low and high frequency ranges, respectively.

We confirm that a frequency of occurrence of AKR strongly depends on the magnetic local time and magnetic latitude of the spacecraft. On the other hand, we find three new results: First, the illumination region of AKR extends duskward as geomagnetic conditions become more disturbed especially for the low frequency range. Secondly, the frequency of occurrence of AKR depends on observed time in UT which approximately corresponds to longitude, especially for the high frequency range. Thirdly, AKR is more active on the winter hemisphere, especially for the high frequency range.

We propose that possible origins of these dependences are not only the population of energetic electrons on the auroral field lines, but also the structure of the auroral plasma cavity which should be sensitive to plasma density in the surrounding plasmasphere.

6.1 Introduction: The auroral kilometric radiation

The auroral kilometric radiation (AKR) is generated in a region above the nightside auroral zone on the field lines of discrete aurorae. Typical location of the source is around ~22h of magnetic local time (MLT), ~70° of invariant latitude, and 1.5~3 R_E of altitude [*Gurnett*, 1974; *Kurth et al.*, 1975; *Benson and Calvert*, 1979; *Benson and Akasofu*, 1984; *Huff et al.*, 1988].

AKR originates at frequencies close to the local electron gyrofrequency, f_g [*Alexander and Kaiser*, 1976; *Benson and Calvert*, 1979; *Bahnsen et al.*, 1987]. The generation mechanism of AKR is believed to be the electron cyclotron maser instability [*Wu and Lee*, 1979] induced by energetic electrons supplied from the inverted-V acceleration region on the auroral field lines [*Ackerson and Frank*, 1972; *Benson et al.*, 1980]. It

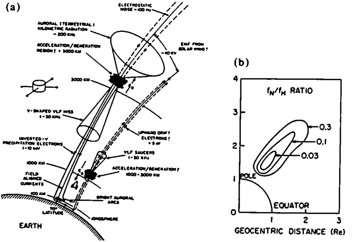

Figure 6.1: A model of the auroral zone. (a) Conceptual view of auroral zone [cf. *Shawhan*, 1982]; (b) The ratio of electron plasma frequency (f_N) and gyrofrequency (f_H) in the auroral plasma cavity [*Calvert*, 1981].

is known that the electron cyclotron maser instability becomes effective only in the auroral plasma cavity shown in Figure 6.1 where plasma frequency, f_p, is less than f_g (typically, $f_p/f_g < 0.2$–0.3) [*Calvert*, 1981; *Wu*, 1985]. On the auroral field lines, f_g is inversely correlated with altitude (e.g. $f_g \sim 500$ kHz at 1.5 R_E and $f_g \sim 200$ kHz at 2 R_E) so that the observed spectrum of AKR indicates the altitude of distribution of energetic electrons and structure of the auroral plasma cavity to distant observers.

However, it is not so simple because the observed spectrum is also affected by propagation. Radiation at each frequency has its own propagation path determined by the source location and density profile in the plasmasphere [*Green et al.*, 1977; *Hashimoto*, 1984]. As shown in Figure 6.2 [*Gurnett*, 1974], propagation of AKR is prevented by the plasmasphere and it is relatively hard for AKR to propagate to a region close to the magnetic equatorial plane or to the dayside zone. Thus the observed spectra of AKR also depend on the location of the spacecraft.

Unfortunately, it is hard to divide contributions of both factors to observed spectra. Furthermore, geomagnetic activity simultaneously affects not only generation but also propagation of AKR. The former is evident in the positive correlation between power flux of AKR and the auroral electrojet index *AE* [*Kurth et al.*, 1975; *Voots et al.*, 1977; *Murata*, 1995] while the latter is expected from the inverse correlation between radius of the plasmasphere and Kp index [cf. *Carpenter and Anderson*, 1992]. Actually, it is known that the frequency of the flux peak in the spectrum appears to vary inversely with AE index from a maximum near 300 kHz during very quiet times to a minimum

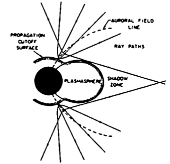

Figure 6.2: Qualitative sketch of the ray paths of AKR at low altitudes and fixed frequency along an auroral field line. Because the refractive index goes to zero at the propagation cutoff, there is a strong tendency for the ray paths to be refracted upward, away from the propagation cutoff surface [*Gurnett*, 1974].

below 200 kHz during very disturbed times (Figure 6.3 (a)) [*Kaiser and Alexander*, 1977], but we can not easily distinguish how both generation and propagation factors contribute to such spectral variations.

For solving this problem, we will evaluate the dependence of the angular distribution of AKR shown in Figure 6.3 (b) [cf. *Green et al.*, 1977] on various factors which may affect the generation and/or propagation of AKR. In this study, we analyze spectra and angular distributions of AKR using the 38-month plasma wave data sets from the GEOTAIL spacecraft. We investigate contributions of some possible factors expected to affect generation and/or propagation of AKR, and evaluate the distribution of energetic electrons and the structure of the auroral plasma cavity above the auroral zone through remote satellite observations.

6.2 Analyzed data sets

We use the 38-month data sets of Band-5 (100-800 kHz) of electric field receivers of the PWI/SFA aboard GEOTAIL from January 1993 to February 1996. Before October 1994, GEOTAIL was on the Distant-Tail orbit and mainly stayed in the 20–4h MLT zone. Since November 1994, GEOTAIL has been on the Near-Tail orbit and uniformly covers all MLT zones. On both orbits, GEOTAIL has stayed in a region close to the ecliptic plane and covered $+40° \sim -40°$ of magnetic latitude (Figure 6.4).

In Figure 6.5, we show typical variations of AKR spectra in (a) 6 hours, (b) 3 days, (c) 1 month, and (d) 1 year. Figure 6.5 (a) shows variation of AKR spectrum in a few hours associated with each substorm. Frequency of AKR decreases for ~0.5-1 hour associated with enhancement of its power flux, and inversely increases after that. This feature agrees well with inverse correlation of the frequency of the peak flux with AE index indicated in Figure 6.3 (a) [*Kaiser and Alexander*, 1977]. Figure 6.5 (b) shows

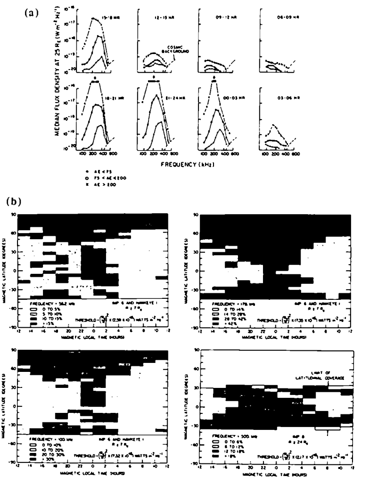

Figure 6.3: Previous observations of AKR spectra. (a) AKR spectra normalized at a distance of 25 R_E observed by IMP-6 grouped according to magnetic local time and AE index [*Kaiser and Alexander*, 1977]. (b) The frequency of occurrence diagram of AKR as a function of MLT and magnetic latitude at 56.2 kHz, 100 kHz, 178 kHz, and 500 kHz observed by IMP-6 and Hawkeye-1. [*Green et al.*, 1977].

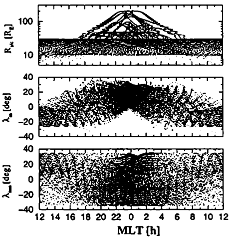

Figure 6.4: Trajectories of GEOTAIL from January 1993 to February 1996. (a) MLT and radial distance of GEOTAIL, $R_{s/c}$; (b) MLT and magnetic latitude of GEOTAIL, λ_m; (c) MLT of GEOTAIL and magnetic latitude of sub-solar point, λ_{sun}.

variation of AKR spectrum with 1 day periodicity. This is caused by variation of magnetic latitude of the spacecraft associated with rotation of the Earth, while there might also be possible contributions of longitude of the source or angle between geomagnetic axis and the Sun–Earth line. Figure 6.5 (c) shows variation of AKR spectrum for 0.5-1 month periodicity positively correlated with geomagnetic disturbance. Since variation of Kp index is positively correlated with kinetic energy flow of solar wind, this variation supports the idea that the solar wind is one of driving forces of AKR activity. Figure 6.5 (d) shows seasonal variation of AKR spectrum in which frequency range of AKR is higher in summer/winter than in spring/autumn. This is caused by variation of magnetic latitude of the spacecraft associated with revolution of the Earth around the Sun, while there might also be possible contributions of angle between the geomagnetic axis and the Sun-Earth line.

In this study, we analyze the angular distribution of AKR and investigate contributions of some factors suggested above; 'the magnetic disturbance', 'the longitude of the source', and 'the angle between the geomagnetic axis and the Sun–Earth line'.

6.3 Statistical analysis: Results

In this study, we normalize AKR flux at a reference distance of 1 R_E with expected $1/R^2$ radial variations of the power flux [cf. *Green et al.*, 1977]. Threshold flux judged as AKR detection is chosen as -148 dB $\mathrm{Wm^{-2}Hz^{-1}}$ in mean value for 3 minutes. We do not use data measured at a distance of <10 R_E to avoid uncertain effects of near-earth propagation.

Figure 6.6 shows the frequency of occurrence of AKR as a function of MLT and magnetic latitude (λ_m) of the spacecraft at 100, 200, 300, 400, 500, and 600 kHz. We use blocks of 2/3-hour increments in MLT and 5° increments in λ_m. The frequency of occurrence in each block is calculated by dividing the total number of detections above the threshold flux by the total number of observations. Blocks with shaded lines indicate lack of observations. Although the total number of detections is contaminated by strong type III solar radio bursts, the effect is negligible because type III bursts have much shorter duration time than AKR above 100 kHz.

It is not possible to define the solid angle of the AKR illumination region from our analysis because of insufficient coverage of data points in magnetic latitude. However, we can find in Figure 6.6 that the illumination region is generally evident in the nighttime hemisphere (18-6h MLT) at each frequency. Northern and southern parts of the illumination region are divided at the magnetic equator and illuminated from sources in the northern and southern auroral zones, respectively. Below 300 kHz, the northern and southern illumination regions are merged at 22–0h MLT. This indicates that the source of AKR is centered on 22-0h MLT [cf. *Green et al.*, 1979]. On the other hand, the illumination region above 400 kHz has less extent, especially on the duskside hemisphere. This result suggests two ideas: One is that duskward propagation of AKR is more favorable below 300 kHz than above 400 kHz. The other is that the source of AKR extends more duskward below 300 kHz than above 400 kHz.

Here after, we concentrate on analyzing data at 200 kHz and 500 kHz which are

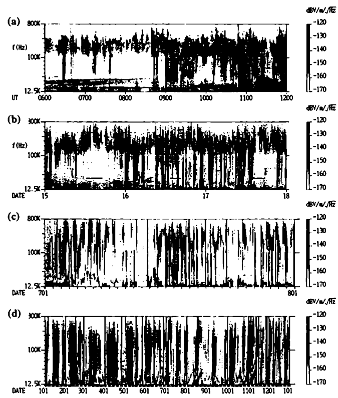

Figure 6.5: Frequency-time spectrogram obtained by the PWI/SFA: (a) 6 hours plot in 1 November 1993; (b) 3 days plot from 1 to 3 November 1993; (c) 1 month plot from 1 to 30 November 1993; (d) 1 year plot in 1993.

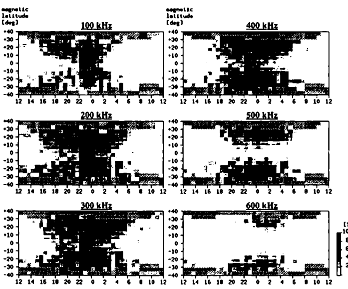

Figure 6.6: The frequency of occurrence of AKR as a function of magnetic local time (MLT) and magnetic latitude (λ_m) of the spacecraft at 100, 200, 300, 400, 500, and 600 kHz. X-axis is MLT, and Y-axis is λ_m. We use blocks of 2/3-hour increments in MLT and 5° increments in λ_m. Blocks with oblique lines indicate lack of observations.

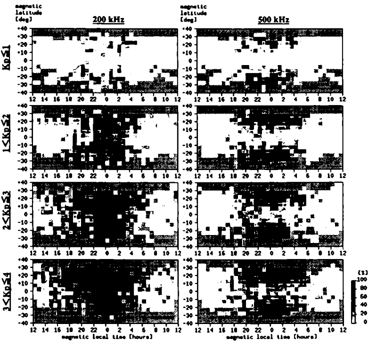

Figure 6.7: The frequency of occurrence of AKR at 200 kHz and 500 kHz as a function of MLT and λ_m of the spacecraft classified by Kp indices at observed time. From the top panels, data observed at $Kp \leq 1$, $1 < Kp \leq 2$, $2 < Kp \leq 3$, and $3 < Kp \leq 4$ are indicated.

representative of AKR at low and high frequency ranges, respectively. They are enough to describe the general results of our analyses.

6.3.1 Dependence on magnetic disturbance

Next, we investigate the illumination region classified by Kp indices at observed time in order to search for the influence of magnetic disturbances upon the observed spectrum of AKR. Figure 6.7 shows the frequency of occurrence at 200 kHz and 500 kHz observed at $Kp \leq 1$, $1 < Kp \leq 2$, $3 < Kp \leq 3$, and $3 < Kp \leq 4$, respectively. We exclude data observed at $Kp > 4$ because there are not enough samples for statistical analysis. Coordinates and parameters are the same as those in Figure 6.6.

When Kp index is small, AKR is more active at 500 kHz. The illumination regions at

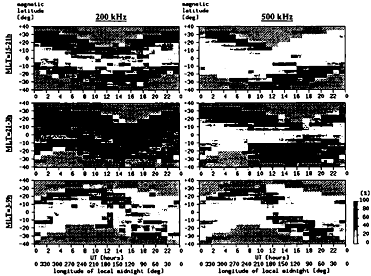

Figure 6.8: The frequency of occurrence of AKR at 200 kHz and 500 kHz as a function of observed time (UT) and λ_m, classified by observed MLT. From the top panels, data observed in 15-21h MLT, 21-3h MLT, and 3-9h MLT zone are indicated. X-axis is UT and corresponding longitude at local midnight. Y-axis is λ_m. We use blocks of 1-hour increments in UT and 5° increments in λ_m.

both frequencies are limited to 20-4h MLT. With increase of Kp index, the illumination regions at 200 kHz and 500 kHz extend to duskward, dawnward, and equatorward but in different ways. At 500 kHz, the illumination region symmetrically extends both duskward and dawnward, to the 18-6h MLT zone. On the other hand, the illumination region at 200 kHz extends more duskward and reaches to the dayside hemisphere. These features should be one of the causes of the difference in the shape of the illumination region at 200 kHz and 500 kHz, shown in Figure 6.6.

6.3.2 Dependence on longitude of the source region

Next, we investigate the dependence of the illumination region on the observed time in UT in order to study the influence of the longitude of the source region upon the observed spectrum of AKR. If the source of AKR is small enough and can be assumed to be located at a specific magnetic local time, we can use the observed time as an approximate indicator for longitude of the source region. Figure 6.8 shows the frequency of occurrence as a function of observed time (UT) and magnetic latitude (λ_m) of the spacecraft at 200 kHz and 500 kHz, classified by observed magnetic local time at 15-21h MLT, 21-3h MLT, and 3-9h MLT, respectively. In these diagrams, we use blocks of 1-hour increments in UT and 5° increments in λ_m.

At 500 kHz, Figure 6.8 indicates clear correlation between the frequency of occurrence and observed time corresponding to longitude of the source. Active time (longitude) of AKR at 500 kHz is asymmetric between the northern and southern hemispheres; 2-14h UT (30°W-150°E at local midnight) on the northern hemisphere, and 10-22h UT (150°E-30°E at local midnight) on the southern hemisphere, respectively. This is generally independent of observed magnetic local time. On the other hand, we can not find such clear dependence at 200 kHz except at 3-9h MLT. Only at 3-9h MLT are there weak dependences in the same manner as at 500 kHz.

6.3.3 Dependence on angle between the geomagnetic axis and the Sun-Earth line

Finally, we investigate the dependence of the illumination region on the magnetic latitude of the sub-solar point, λ_{sun}, in order to study the influence of the angle between the geomagnetic axis and the Sun-Earth line upon the observed spectrum of AKR. Parameter λ_{sun} correlates with season at the source region: The southern hemisphere is winter when $\lambda_{sun} > 0°$, and the northern hemisphere is winter when $\lambda_{sun} < 0°$, respectively. Figure 6.9 shows the frequency of occurrence of AKR at 200 kHz and 500 kHz observed in $\lambda_{sun} > +15°$, $+15° > \lambda_{sun} > 0°$, $0° > \lambda_{sun} > -15°$, $-15° > \lambda_{sun}$, respectively. Coordinates and parameters are the same as those of Figure 6.6.

At 500 kHz, Figure 6.9 indicates clear correlation between the frequency of occurrence and λ_{sun}: AKR is more active on the southern hemisphere when $\lambda_{sun} > 0°$ and on the northern hemisphere when $\lambda_{sun} < 0°$, even at same MLT and $| \lambda_m |$ This indicates that AKR is more active on the winter hemisphere. On the other hand, we can also find the same dependence at 200 kHz, while there is also the weak activity even on the summer hemisphere. We also find that extent of the illumination region in MLT and λ_m is not seriously affected by λ_{sun} at both frequencies. This indicates that propagation conditions, such as the source locations and density profiles in the plasmasphere, are not strongly affected by λ_{sun}.

6.4 Discussions

Results of our analyses are summarized in Table 6.1. Based on the results described above, we evaluate generation and propagation properties of AKR, and try to estimate the distribution of energetic electrons and the structure of the auroral plasma cavity above the auroral zone.

First, we discuss general features of the illumination region of AKR indicated in Figure 6.6. We find that the illumination region extends more for the low frequency range than for the high frequency range. Such difference is basically explained by propagation. Since altitude of the source depends on generated frequency, we can reproduce the observed illumination regions by ray tracing studies based on an adequate

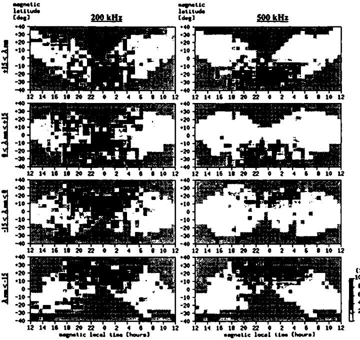

Figure 6.9: The frequency of occurrence of AKR at 200 kHz and 500 kHz as a function of magnetic local time (MLT) and magnetic latitude (λ_m) of GEOTAIL, classified by the magnetic latitude of the sub-solar point (λ_{sun}). From the top panels, data observed at $\lambda_{sun} > +15°$, $+15° > \lambda_{sun} > 0°$, $0° > \lambda_{sun} > -15°$, and $-15° > \lambda_{sun}$ are indicated.

	low-frequency (ex. 200 kHz)	high frequency (ex. 500 kHz)
General	The illumination region is inclined duskward. Its boundary is at 5-7h MLT in dawnside, 16–18h MLT in duskside, and ±5–10° in λ_m.	The illumination region is centered on local midnight. Its boundary is at 4-6h MLT in dawnside, 18–20h MLT in duskside, and ±10–20° in λ_m.
Kp index	AKR is evidently active in disturbed time. The illumination region especially extends to duskward.	AKR is moderately active in disturbed time. The illumination region moderately extends.
Observed time	There is no clear dependence in 15–21h MLT and 21-3h MLT, and weak dependence in 3-9h MLT.	AKR is active in 2-14h UT on the northern hemisphere and in 10–22h UT on the southern hemisphere.
λ_{sun}	AKR is slightly active in the winter hemisphere.	AKR is evidently active in the winter hemisphere.

Table 6.1: Summary of observed features of AKR activity

density model [cf. *Green et al.*, 1977; *Hashimoto*, 1984]. This means that our results can provide useful information to evaluate density profiles in the plasmasphere.

On the other hand, we also find in Figure 6.6 that the duskward extension of the illumination region is more evident for the low frequency range. It is known that density of the plasmasphere is not symmetric on the geomagnetic equatorial plane. Namely, it is more dense in duskside than in dawnside due to up-welling of photo-ionized particles in the dayside ionosphere [cf. *Chapman*, 1931] and by asymmetry of convection pressure in the magnetosphere [cf. *Chappell et al.*, 1971]. This suggests that dawnward propagation of AKR might be easier than duskward propagation. However, our results are against the idea, and we should reject such simple interpretation based only on propagation. Since extension of the illumination region is not prominent in high-frequency AKR generated at a lower altitude, we should suggest that the source of AKR extends more duskward only at a higher altitude. We will verify this idea later.

Next, we evaluate the dependence of the illumination region on geomagnetic disturbances indicated in Figure 6.7. We suggest that the equatorward extension of the illumination region in large Kp is caused by the equatorward shift (~5 degree) of the auroral plasma cavity in the disturbed phase indicated in Figure 6.10 [*Persoon et al.*, 1988]. Since the equatorward edge of the auroral plasma cavity is close to the magnetic field line of the plasmapause, the origin of such motion should be the inward motion of the plasmapause for 1 hour just after the onset of substorms shown in Chapter 5. We also suggest that the inverse correlation of the frequency of the peak flux associated with enhancement of AKR indicated in Figure 6.3 (a) [*Kaiser and Alexander*, 1977] and Figure 6.5 (a) might also be related to the the equatorward shift of the auroral plasma cavity: Since f_g is lower in a region of lower magnetic latitude at the same altitude, the equatorward shift might be well correlated with decrease of f_g in the auroral plasma cavity.

On the other hand, we find that the illumination region is limited to 20-4h MLT for small Kp at all frequencies, and shows duskside extension for large Kp especially for the low frequencies. We originally expected to find influence of geomagnetic disturbances because geomagnetic activity affects propagation conditions of AKR through variation of density profile in the plasmasphere. However, latitudinal and dawnward extensions

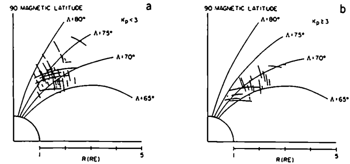

Figure 6.10: The cavity intervals in both hemispheres for (a) $Kp < 3$ and (b) $Kp \geq 3$ [*Persoon et al.*, 1988]. The equatorward shift of the auroral cavity with increasing geomagnetic activity is evident.

of the illumination regions are relatively small in both 200 kHz and 500 kHz, so that the propagation path of AKR only shows small variation associated with geomagnetic disturbances. Since extension of the illumination region is not prominent in the high-frequency AKR generated at lower altitude, we get an interpretation that the source of AKR originally lies in a region close to local midnight, and extends to duskward as geomagnetic conditions becomes more disturbed only at higher altitude. We should pay attention that enhancement of low-frequency AKR and optical auroral activity in the duskside hemisphere suggests presence of energetic electrons on the auroral field lines. Therefore, lack of AKR activity in high frequency on the duskside hemisphere suggests that generation of the high-frequency AKR should be prevented even on the auroral field lines filled with energetic electrons because the auroral plasma cavity is difficult to form at a lower altitude in the duskside hemisphere. It is possible because we already described that density in the duskside hemisphere is larger due to up-welling of photo-ionized particles in the dayside ionosphere [cf. *Chapman*, 1931]. Since formation of the auroral plasma cavity needs large depression of electron density on the auroral field lines, formation of the auroral plasma cavity might be sensitive to density in the surrounding plasmasphere and easily blocked on the duskside hemisphere.

Next, we evaluate the dependence of the illumination region on longitude of the source indicated in Figure 6.8. Although the longitudinal dependence of AKR activity is first reported in this study, we expected this discovery because the similar dependence has been already found in Jovian/Saturnian radio activities [cf. *Kaiser*, 1989] and in optical auroral activities [*Rycroft*, 1987]. Figure 6.11 shows that optical aurora on the northern hemisphere is most active at ~10h UT (150°W longitude at local midnight) where the strength of geomagnetic field strength is relatively weak. This feature is explained by the altitude of magnetic mirror point: More energetic electrons are supplied in a region with weak the geomagnetic field strength where the altitude of the magnetic mirror point decreases [*Stenbaek-Nielsen et al.*, 1973]. The longitudinal

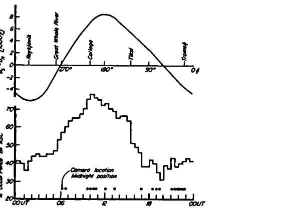

Figure 6.11: The upper plot gives difference in magnetic field strength at 300 km at conjugate points along 65° invariant latitude. The lower plot gives occurrence of aurora observed on all-sky camera from auroral stations located between 64° and 70°N geomagnetic latitude [*Stenbaek-Nielsen et al.*, 1971].

dependence of AKR at 500 kHz indicated in Figure 6.8 is generally consistent with such dependence of the optical auroral activities, so that generation of AKR at lower altitude is also inversely correlated with altitude of the magnetic mirror point. On the other hand, we also show that the longitudinal dependence is less clear for the low frequency range. In order to explain this feature, we propose two ideas: One is that altitude of the magnetic mirror point is generally lower than the source of AKR for the low frequency range. In this case, energetic electrons are always supplied to the auroral plasma cavity above the magnetic mirror point so that the activity of AKR for the low frequency range has nothing to do with the altitude of the magnetic mirror point and longitude of the source. The other is that the source of AKR for the low frequency range is not concentrated to a region at a specific magnetic local time. In this case, AKR from the extended regions at different longitudes can cancel out the longitudinal dependence even if it really exists, so that we can not expect a clear dependence on observed time. The latter idea might be more applicable because we already suggested that the source of AKR should seriously extend duskward for the low frequency range especially in the disturbed phase. The weak dependence on observed time at 200 kHz in 3-9h MLT zone also supports this idea. Since AKR observed in 3-9h MLT zone includes less component from the duskside hemisphere, the apparent source seems to be concentrated to a specific magnetic local time and weak longitudinal dependence can be expected.

Finally, we evaluate the dependence of the illumination region on the angle between the geomagnetic axis and the Sun-Earth line indicated in Figure 6.9. Although the

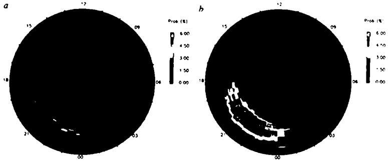

Figure 6.12: The probability of observing the accelerated electrons as a function of magnetic latitude(60°–90°) and local time [*Newell et al.*, 1996]. All events above 5.0 erg cm^{-2}s^{-1} from December 1983 to November 1992. (a) Under sunlit conditions (solar zenith angle<85°): (b) in darkness (solar zenith angle>110°).

seasonal dependence of AKR activity is first reported in this study, such kind of dependences was once reported for Saturnian kilometric radiation [*Warwick et al.*, 1982]. It is hard to explain the dependence on λ_{sun} by propagation because it requires a large asymmetry of the density profile on the northern and southern hemispheres of the plasmasphere. This idea is rejected because boundaries of the illumination region are not clearly affected by λ_{sun}. There is an asymmetry in the population of precipitating electrons on the summer and winter hemisphere, i.e., there is a larger population on the winter hemisphere indicated in Figure 6.12 [*Newell et al.*, 1996]. This is a powerful candidate to explain the seasonal variation of AKR. However, we should pay attention to the lack of such dependence for AKR for the low frequency generated at higher altitudes. This indicates that the population of energetic electrons on the auroral field lines should not show clear seasonal variation at higher altitude. Here, we propose a complementary idea, asymmetry of structure of the auroral plasma cavity, which is already used to explain the dependence on geomagnetic disturbances: It is known that electron density of the summer hemisphere generally increases due to up-welling of photo-ionized particles, especially at a lower altitude. Therefore, generation of AKR on the summer hemisphere should be easy to be blocked especially for the high frequency.

6.5 Conclusion

In this study, we successfully evaluated the distribution of energetic electrons and the structure of the auroral plasma cavity above the auroral zone through only remote observations. Analyses of the spectra and angular distributions of AKR have led to the following conclusions:

(1) The extension of the illumination region of AKR should basically be explained by propagation which is determined by the source locations and the density profile

in the plasmasphere. Therefore, our results can provide useful information to evaluate density profiles in the plasmasphere.

(2) In the disturbed geomagnetic conditions, the illumination region extends to duskward especially for the low frequency. This suggests that the source of AKR extends to duskward especially at high altitude. We also suggest that such extension is not evident at lower altitude because the formation of the auroral plasma cavity should be blocked on the duskside hemisphere by increase of electron density.

(3) We find the dependence of AKR activity on longitude of the source especially for the high frequency, to be in the same manner as shown in the optical auroral activity. This suggests that populations of energetic electrons at a lower altitude are controlled by the altitude of the magnetic mirror point. The weak dependence of AKR activity for the low frequency should be caused by duskward extension of the source region.

(4) We find that AKR is more active on the winter hemisphere, especially for the high frequency range. Asymmetry of the population of precipitating electrons is a possible candidate, while we also propose another possible origin, asymmetry of structure of the auroral plasma cavity. We suggest that formation of the auroral plasma cavity should be blocked on the summer hemisphere by large electron density, especially at a lower altitude.

In these conclusions, we suggest that the observed AKR spectrum should be controlled by not only the population of energetic electrons but also the structure of the auroral plasma cavity. The latter is suggested to be sensitive to density in the surrounding plasmasphere. Density of the plasmasphere is also expected to be correlated with solar activity with 11-year periodicity, so that we expect to find a variation of AKR spectrum with the same periodicity. Needless to say, we also need further analyses by remote/in-situ observations and numerical studies. The most important target is formation of the auroral plasma cavity because its generation mechanism is not established yet. We expect to confirm and understand the features presented in this study through collaborations with AKEBONO satellite which can do in-situ observation in the auroral plasma cavity and POLAR satellite which can cover high magnetic latitudes.

Chapter 7

Applications to Planetary Explorations

In previous chapters, we showed advantages of the combination of remote/in-situ observations and numerical simulations of low frequency radio waves. They can provide real-time information around the sources and on the propagation paths to distant observers. These powerful tools are also able to contribute to the future planetary explorations.

In this chapter, we show an example of such investigations, a survey for Jovian hectometric and kilometric radiations by the GEOTAIL spacecraft before, during, and after the impacts of Comet Shoemaker-Levy 9 (SL-9). We did not find clear enhancement of the Jovian radiation activity in the whole period nor around each impact time. With regard to the Jovian magnetospheric activity, synchrotron radiation increased during the week of the impacts, and X-ray radiation was clearly detected just around K impact time at the magnetic conjugate footprint of the impact site. These results suggest that a strong perturbation at the impact sites has given non negligible change in the inner magnetosphere. On the other hand, our results suggest that such activities were limited in the inner magnetosphere, and that there was only small amount of direct coupling between the cometary fragments and the Jovian outer magnetosphere. This is consistent with no significant change of the decametric radiations during the SL-9 event.

In addition, we also show a short review of planned space missions and possible space studies which will affect the whole area of human activities.

7.1 Introduction: The planetary magnetospheres

Other planets, satellites, and comets also have the magnetospheres which is accompanied with plasma wave activities. These planetary magnetospheres are predicted by observations of radio and optical features, and directly confirmed by spacecraft observations. Table 7.1 shows scales of the planetary magnetospheres of strong-magnetized (Earth and Jupiter) and weak-magnetized (Venus and Mars) planets. Here, we present an overview of structures and radio activities in planetary magnetospheres.

Figure 7.1 summarizes four models of interaction between the solar wind and a

	D	R_p	B_{eq}	R_m
Earth	1.000AU	6378km(1.00R_E)	0.31G	11R_E
Jupiter	5.203AU	71400km(11.2R_E)	4.2G	45R_J(500R_E)
Venus	0.723AU	6052km(0.95R_E)	0.0003G	2R_V(1.9R_E)
Mars	1.524AU	3397km(0.53R_E)	0.0006G	2R_M(1.1R_E)

Table 7.1: Scales of planetary magnetospheres of strong-magnetized (Earth and Jupiter) and weak-magnetized (Venus and Mars) planets. D is distance from the Sun. R_p is equatorial radius of the planet. B_{eq} is magnetic field strength on the equator surface. R_m is radius of the magnetosphere on the section perpendicular to the solar wind flow.

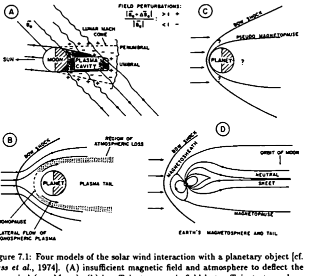

Figure 7.1: Four models of the solar wind interaction with a planetary object [cf. *Ness et al.*, 1974]. (A) insufficient magnetic field and atmosphere to deflect the solar wind (ex. Moon). (b) insufficient magnetic field but sufficient atmosphere (ex. Venus, Mars). (c) insufficient atmosphere but weak magnetic field (ex. Mercury). (d) sufficient magnetic field (ex. Earth, Jupiter, Saturn, Uranus, Neptune).

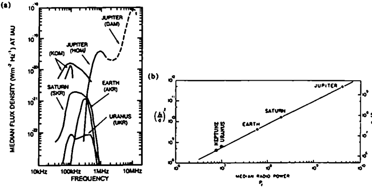

Figure 7.2: Planetary AKR-like radio emissions. (a) The median flux density observed by Voyager PRA instrument from a distance of 1 A.U. from each planet [*Kaiser*, 1989]; (b) The "radiometric Bode's law", the relation between the total solar wind input power into the magnetospheres and the total radio power of planetary AKR-like radio emissions. Efficiency of energy conversion is about 5×10^{-6} [*Desch and Kaiser*, 1984].

planetary object [cf. *Ness et al.*, 1974]. Model A shows the weakest interaction case, with insufficient magnetic field nor atmosphere to deflect the solar wind flow. In this case, only plasma wake is formed in downstream of the object, like Moon. Model B shows the case without magnetic field but with sufficient atmosphere. In this case, plasmasphere is formed without large magnetosphere, like Venus and Mars. Model C shows the case without atmosphere but with weak magnetic field. Such magnetic field is intrinsic component or secondary one induced by interaction between the solar wind flow and the conducting planetary interior. In this case, small magnetosphere is formed, like Mercury. Model D shows the case with sufficient magnetic field to deflect the solar wind flow, like all of Jovian type planets, Jupiter, Saturn, Uranus, and Neptune. Our Earth has both magnetic field and atmosphere, and is the only terrestrial type planet to be included in this case.

These features strongly influence the planetary radio activities. Since energy source of activities in the planetary magnetospheres is the intercepted solar wind kinetic energy, scale of planetary radio activities is also affected by that of the planetary magnetospheres. The most remarkable case is the AKR-like auroral emission. Although the AKR-like auroral emission is only active in magnetized planets because of necessity of large magnetic field for excitation, this type of emissions is very intense and already detected from whole the magnetized planets. Figure 7.2 (a) shows the median spectrum observed by Voyager PRA instrument from each magnetized planet [*Kaiser*, 1989]. It must be remembered that the Voyager measurements were made from limited ranges of local times and magnetic latitudes, i.e., beaming is probably very important. However,

	Frequency Range	Radiated Power	Source Location
DIM	80 MHz - 300 GHz	2 GW	radiation belts
DAM	2 - 40 MHz	400 GW	Io torus field line
HOM	0.2 - 2 MHz	1 GW	auroral field line
bKOM	10 - 1000 kHz	500 MW	Io torus or auroral
nKOM	40 - 200 kHz	100 MW	Io torus
Continuum	0.1 - 30 kHz	100 GW	outer magnetosphere
Fast drift	1 - 500 kHz	large	?

Table 7.2: Characteristics of Jovian nonthermal radio components [cf. *Kaiser*, 1993]

there is a remarkably constant scaling factor relating the total solar wind input power into each planetary system and the AKR-like auroral emissions. Figure 7.2 (b) shows the "radiometric Bode's law" where solar wind input is plotted against observed total radio power [*Desch and Kaiser*, 1984]. All the planetary AKR-like emissions fall on a straight line indicating a constant "efficiency" factor of 5×10^{-6}.

On the other hand, foreshock activities are expected in all type of planetary magnetospheres which surely have the bow shock. Therefore, activity of the $2f_p$ radio emission should normally appear in upstream of the planetary bow shocks [cf. *MacDowall et al.*, 1992]. Actually, however, clear $2f_p$ radiation has been only observed in the terrestrial foreshock. This is because flux of the $2f_p$ radiation is not strong enough to be detected at the planets with only small-scale magnetospheres or concealed by other stronger planetary emissions at the planets with large magnetospheres.

Nonthermal continuum radiation is expected in Model B and D, with relative dense plasmaspheres. Actually, active nonthermal continuum radiation has been observed from the Earth, Jupiter, and Saturn. Since excitation of nonthermal continuum radiation is not so difficult in the region with large density inclination like the plasmapause, there are large possibilities of detection of them from the all magnetospheres.

7.2 The Jovian radiation during the impact of Comet Shoemaker-Levy 9

Large magnetic field strength gives Jupiter the largest magnetosphere in the solar system. Because of fast rotation of Jupiter, Jovian magnetosphere is characterized by rather flat shape compared with the terrestrial magnetosphere. Jovian magnetosphere also has a peculiar feature characterized by large amount of gas cloud ejected from Galilean satellite Io by strong volcanic activities. The expelled gas cloud is ionized and forms ring-shape plasma cloud named 'Io plasma torus' on the trajectories of Io. General structure of the Jovian magnetosphere is shown in Figure 7.3.

These features make Jupiter a brightest radio source exceeding the Sun in the low frequency range. Jovian nonthermal radio emission appears in several wavelength bands; decimetric wavelength (DIM), decametric wavelength (DAM), hectometric wavelength (HOM), and kilometric wavelength (KOM) [cf. *Carr et al.*, 1983; *Kaiser*, 1989] (Figure 7.4; Table 7.2). DIM radiation is synchrotron emission generated by relativistic particles trapped in the Jovian radiation belt. DAM and HOM radiation are thought to

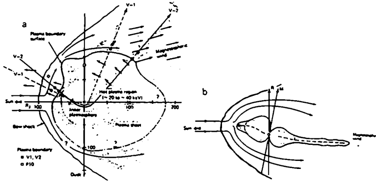

Figure 7.3: Structure of the Jovian magnetosphere on (a) the equatorial and (b) meridional plane [*Krimigis et al.*, 1979]

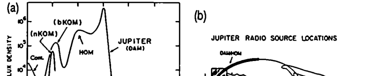

Figure 7.4: (a) Spectrum of Jovian magnetospheric radio emissions normalized to an observer at a constant distance [cf. *Carr et al.*, 1983]. The usual acronyms for each component are shown. (b) Schematics of the 'best guess' at some of the source locations shown in the meridian plane projection [cf. *Kaiser*, 1989]

	Rotation	Io	Solar Wind
DIM	strong	none?	maybe
DAM	strong	strong	moderate
HOM	strong	none	moderate
bKOM	strong	none?	moderate
nKOM	strong	strong?	none?
Continuum	moderate	none	strong
Fast drift	moderate	none	moderate

Table 7.3: Drivers of Jovian radio variability [cf. *Kaiser*, 1993]

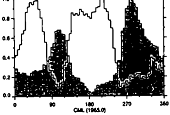

Figure 7.5: Normalized occurrence probability histogram showing the anti-correlation of the longitude occurrences of HOM (shaded) and bKOM (full line) components within the Jovian rotation [*Lecacheux et al.*, 1992].

be produced by the electron cyclotron maser mechanism like the terrestrial AKR. KOM radiation which consists of broadband (bKOM) and narrowband (nKOM) components is thought to be produced by the linear mode-conversion mechanism like the terrestrial nonthermal continuum radiation or the $2f_p$ emission. However, precise mechanisms and source locations of DAM, HOM, and KOM radiations are not well understood even today. There are also nonthermal continuum radiation and fast drift component which are thought to correspond to the terrestrial continuum radiation and the LF radio burst, respectively.

Although the driving forces of variability in these radiations are clear, the driving mechanism is unknown for a surprisingly large number. Table 7.3 shows a summary of current knowledge of these driving forces [cf. *Kaiser*, 1993]. As the our results on AKR in Chapter 6, the planetary rotation and the solar wind influence the radio emission (cf. Figure 7.5) [cf. *Lecacheux et al.*, 1992]. Io also induces a 42.5 hour periodicity for DAM and nKOM. This suggests that motion of Io accompanied with plasma cloud induces strong turbulence in the Jovian magnetosphere.

Comet Shoemaker-Levy 9 (SL-9) was tidally disrupted during its own close fly-by of Jupiter on 8 July 1992, and these fragments collided with Jupiter on 16-22 July 1994 (Figure 7.6; Table 7.4). There were predictions that large electric and magnetic turbulence of the Jovian magnetosphere would be created by continuous mass loading [*Herbert*, 1994], dust-plasma and electrodynamical interactions along the trajectory

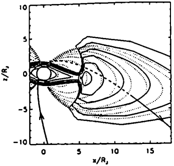

Figure 7.6: The trajectory of SL-9 (thick and dashed line) in the meridian plane projection [*Horányi*, 1994]. Plasma density contours (thin lines) mark the values of $n_p = 10^{-2}, 10^{-1}, 10^0, 10^1, 10^2, 10^3$ cm^{-3} and the magnetic field lines shown (dotted lines) pierce the magnetic equator at L = 2, 4, 6,... R_J.

	date	time(UT)		date	time(UT)		date	time(UT)
A	16	20:13:00	H	18	19:31:59	R	21	05:35:05
B	17	02:53:00	K	19	10:24:14	S	21	15:16:00
C	17	07:12:00	L	19	22:16:48	T	21	18:11:00
D	17	11:54:00	N	20	10:29 17	U	21	21:56:00
E	17	15:12:00	P2	20	15:23:00	V	22	04:23:00
F	18	00:33:00	Q2	20	19:44:00	W	22	08:06:17
G	18	07:33:32	Q1	20	20:13:52			

Table 7.4: Best estimated impact times of fragments of Comet Shoemaker-Levy 9 in July 1994 [*Yeomans and Chodas*, 1996].

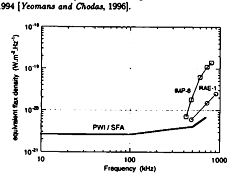

Figure 7.7: Sensitivity of the PWI/SFA determined by background level. Jovian radio flux from the Earth observed by IMP-6 [*Brown*, 1974] and RAE-1 [*Desch and Carr*, 1974] are also indicated.

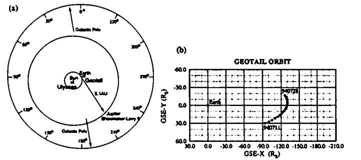

Figure 7.8: Location of each object concerned with our observation in July 1994. (a) Location of Sun, Earth, and Jupiter in the heliographic coordinates. Earth is in the center, and the direction of Jupiter from Earth was almost perpendicular to that of Sun (102° in July 11, and 86° in July 28). The location of ULYSSES is also shown (−73° in heliographic latitude). (b) Location of GEOTAIL in the GSE coordinates. GEOTAIL stayed in distant magnetotail in the whole period.

of the comet [*Ip and Prangé*, 1994; *Bolin and Brenning*, 1994; *Farrell et al.*, 1994; *de Pater*, 1994], and/or ionized shocks from the impact sites [*Kellogg*, 1994]. These predictions also suggested long and/or short enhancement of the Jovian nonthermal radio activity. Therefore, observation of these radio activity variations provides not only valuable information to study the feature of the magnetospheric turbulence under such extraordinary conditions but also new clues for the study of these Jovian radio emissions.

The primary mission objective of the PWI aboard GEOTAIL is to investigate plasma waves and wave–particle interactions in the terrestrial magnetotail. However, it also has a sufficient capability to detect the Jovian HOM and KOM radiation if these radiations are intense enough (Figure 7.7). At the same frequency range, ULYSSES URAP instrument [*Stone et al.*, 1992] also made observations on these events from very different perspectives to Jupiter; ULYSSES was located at the southern solar hemisphere, while GEOTAIL stayed in the ecliptic plane at the whole period of the impacts.

In this study, we made inquiry into the possible HOM and KOM radiation from Jupiter before, during, and after the period of the impacts. We also compared our results with other observations in various wavelengths.

7.2.1 Analyzed data sets

For the observation of the Jovian HOM and KOM radiation, we use Band-4 (12.5-100 kHz) and Band-5 (100-800 kHz) of the PWI/SFA electric field data. Figure 7.8 (a) shows the Jovian location in July 1994 in the heliographic coordinates. Earth is placed in the center of this figure. The distance from Earth to Jupiter was about 5 AU. The

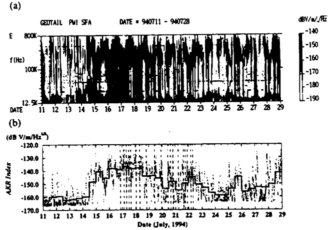

Figure 7.9: GEOTAIL PWI/SFA data in 11-28 July 1994. (a) Frequency-Time spectrogram. (b) AKR index. Thick line shows the average over 12-hour intervals, and dashed vertical line shows the impact time of each fragment.

Jovian direction was almost perpendicular to that of Sun (102° in July 11, and 86° in July 28). Figure 7.8 (b) shows the location of GEOTAIL in the Geocentric Solar Ecliptic (GSE) coordinates. GEOTAIL stayed in the distant magnetotail. Since the direction of Jupiter from GEOTAIL was almost perpendicular to that of Sun and Earth, we can easily distinguish the Jovian radiation from the solar and terrestrial radiation by the direction finding analysis.

Figure 7.9 (a) is the SFA frequency-time spectrogram showing the terrestrial radiations in 11-28 July 1994. Below 50 kHz, terrestrial continuum radiation was intense. Auroral kilometric radiation (AKR) was very intense from 100 kHz to 500 kHz. Figure 7.9 (b) shows the AKR index. Thick line indicates the average over 12-hour intervals. In Figure 7.9 (a), the lower cutoff frequency of the continuum radiation increases up to above 40 kHz on July 14. This indicates increase of the solar wind density. Following this density increase, the AKR index was enhanced and continued until July 21. These large geomagnetic disturbances might have given substantial interference on observation of Jovian decametric radio waves on the ground.

In order to remove contamination from AKR and the terrestrial continuum radiation, we analyze the SFA data at 712-800 kHz for the survey of the HOM radiation and at 89-100 kHz for that of the KOM radiation. On the other hand, we should also pay attention to other background radiation in these frequency ranges before the detailed analysis. Figure 7.10 shows k-vector directions of weak radio waves below −175 dB $Vm^{-1}Hz^{-1/2}$ from January 1993 to March 1994. K vector direction is determined by

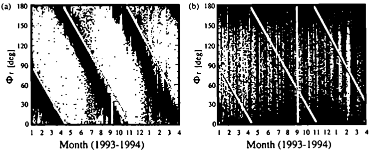

Figure 7.10: The azimuth angles of k vector directions of background radio waves below -175 dB $Vm^{-1}Hz^{-1/2}$ background radio waves observed by the PWI/SFA with 1-minute interval from January 1993 to March 1994. (a) Radiation at 712-800 kHz (HOM); (b) Radiation at 89-100 kHz (KOM). Gray lines indicate the Jovian direction.

direction finding analysis based on spin modulation of electric field strength [*Manning and Fainberg*, 1980]. In Figure 7.10 (a), K vector direction in 712-800 kHz shows systematic variation of half year periodicity, which does not agree with any directions of Jupiter, Sun, Earth, or other planets. This radiation is the galactic background radiation which comes from the region around the northern and southern galactic pole [*Brown*, 1973]. On the other hand, in Figure 7.10 (b), K-vector direction in 89-100 kHz shows no systematic variation except direction of the Earth. This indicates that flux observed in 89-100 kHz is complex of weak terrestrial radiations and instrumental noise. Here after in this chapter, both galactic background and instrumental noise are subtracted from data points by standard Fourier techniques [*Manning and Fainberg*, 1980].

7.2.2 Observation during the SL-9 impacts period

Figure 7.11 shows the radiation flux of (a) 712-800 kHz (average of the 16 frequency components) and (b) 89-100 kHz (average of the 16 frequency components). All the SFA wave data at these two frequency bands were examined at every 1 minute to seek for their propagation direction. The examination was carefully carried out after subtracting the background noise for the whole period mentioned above. Only those with the propagation direction within $\pm 15°$ from Jupiter were selected and plotted by solid dots in Figure 7.11. Thick lines indicate the average over 12-hour intervals. Horizontal dashed lines show the background noise intensity, which is dominated by the galactic background radiation at 712-800 kHz and instrumental noise at 89-100 kHz. From this figure, we can recognize some systematic decrease of flux of the HOM and KOM radiation during the week of the impacts. However, since both radiations are weaker than background noise level, we do not remove the possibilities of contamination from some natural or artificial effects.

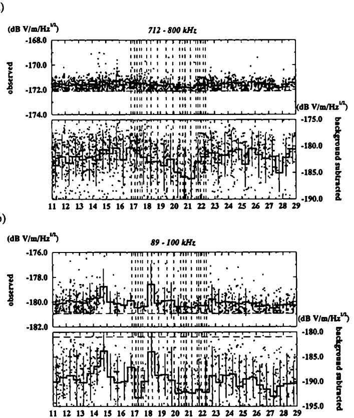

Figure 7.11: Background-noise subtracted fluxes from the Jovian direction in July 11–28, 1994. They are the 1-minute averaged values, Y-axis is radiation flux (dB $Vm^{-1}Hz^{-1/2}$). Only the data in which the k vector direction is within ±15° from the Jovian direction are indicated. Thick line shows the average over 12-hour intervals. 1 σ value at every 12 hours is overlaid by thin vertical lines. Dashed vertical line shows the impacts time of all fragments. Long dashed horizontal line shows the background noise level. (a) Radiation flux at 712–800 kHz (HOM). Upper panel shows the observed data, and lower panel shows the background subtracted data. (b) Radiation flux at 89–100 kHz (KOM). Upper panel shows the observed data, and lower panel shows the background subtracted data.

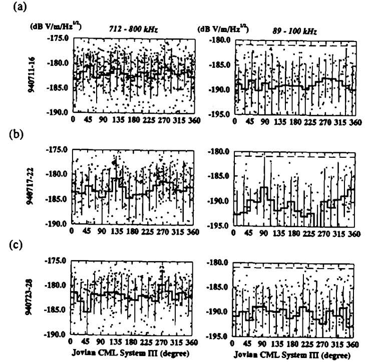

Figure 7.12: Correlation between the radiation flux from the Jovian direction and the Jovian CML System III. Y-axis is radiation flux (dB $Vm^{-1}Hz^{-1/2}$). The data points show the background subtracted data at 1-minute intervals. Thick line shows the average over 30° intervals. 1 σ value at every 30° is overlaid by a thin vertical line. (a) Correlation on 11-16 July 1994. (b) Correlation on 17-22 July 1994. (c) Correlation on 23-28 July 1994.

The Jovian HOM and KOM radiation are strongly modulated as a function of the planetary longitude with 10 hour periodicity. Figure 7.5 shows that the HOM radiation has an emission gap around CML~ 200° (CML: Central Meridian Longitude in System III), and the KOM radiation has an occurrence peak around CML~ 200°, respectively. For confirmation of these features, we searched the correlation between the Jovian CML and the radiation flux from the Jovian direction in 11-16, 17-22, and 23-28 July 1994 (Figure 7.12). All the data points are the results after the background noise being subtracted, and selected with the same method as used in Figure 7.11. Thick line

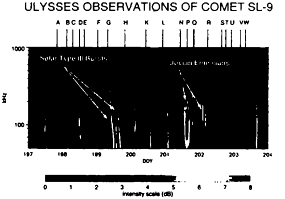

Figure 7.13: Radio spectrum from the ULYSSES/URAP experiment covering the period from July 16 (day 197) to July 23 (day 204) [*Desch et al.*, 1995]. The times of the fragment impacts are indicated by letter. Most of the emission observed is Jovian in origin. Typical examples of solar type III bursts and of Jovian emission events are indicated.

indicates the average over 30-degree intervals. In the case of the HOM radiation, there seems to be a weak occurrence peak around CML∼ 120° and ∼280°, agree with previous results indicated in Figure 7.5 [cf. *Lecacheux et al.*, 1992]. On the other hand, there are no systematic modulation in the KOM radiation. This suggests that the Jovian KOM radiation is not clearly detected in our data.

From Figure 7.11 and Figure 7.12, we can not find clear variation of the Jovian HOM and KOM radiation with exception of the small decrease in the HOM radiation before, during, and after the impacts' period. Observed Jovian radiation in the whole period was weaker than ~ -180 dB $Vm^{-1}Hz^{-1/2}$ (3×10^{-21} $Wm^{-2}Hz^{-1}$) in the HOM radiation, and ~ -185 dB $Vm^{-1}Hz^{-1/2}$ (1×10^{-21} $Wm^{-2}Hz^{-1}$) in the KOM radiation. This is consistent with expected Jovian radiation flux level in its normal activity, $\sim 10^{-21}$ $Wm^{-2}Hz^{-1}$ which is calculated from ULYSSES observation [cf. *Reiner et al.*, 1993].

ULYSSES also made observation during this period [*Desch et al.*, 1995]. Figure 7.13 shows dynamic spectra of ULYSSES/URAP in 16-23 July 1994. They did not get enhancement in the HOM radiation, either. On the other hand, they observed 15 dB enhancement of the KOM radiation during the P/Q fragment impacts on July 20. However, we detected strong AKR enhancement coincidentally and could not confirm this event. (They conclude this as "association with unusual high pressure solar wind streams", and not linked with the impact events.)

7.2.3 Observation with each impact time

Next, we investigate shorter term variation of Jovian radio activities. Around the K impact time, ROSAT detected a large X-ray enhancement (Figure 7.16) [*Waite et al.*, 1995]. Figure 7.14 (a) shows the corresponding frequency-time diagram around the K impact time (10:24UT, 19 July 1994). There is very clear enhancement at about 800 kHz immediately after the K impact time. Figure 7.14 (b) shows the SFA flux-time diagram around the K impact time. Small and large dots indicate the radiation flux from the omni-direction and from the Jovian direction, respectively. In Figure 7.14 (b), the enhancement in Figure 7.14 (a) is also shown in the radiation from omni-direction, but not shown in the radiation from the Jovian direction. Since this enhancement turns out to be a solar type III radio burst by the k vector direction, we can not find any clear enhancement of Jovian radiation associated with K impact.

Figure 7.14 (c) shows the flux-time diagram around the impact times of six large fragments (G, H, K, L, Q1, and S). From Figure 7.14 (b)-(c), radiation flux from the Jovian direction stayed almost at same level during the whole period. The HOM radiation from the Jovian direction was distinguished more frequently at 0.5~1.5 hours before the time of each impact event. This might suggest the existence of the precursor radiation. However, we have no confidence about this conclusion because it was not accompanied by any clear enhancement.

7.2.4 Discussions

We can not identify any clear enhancement of the HOM or KOM radiation activity related to the impacts, except for small variation in the HOM radiation. For enhancement of the Jovian HOM and KOM radiation, large electromagnetic turbulence would be needed in their source locations or on the magnetic field lines penetrating through their generation region. The source location of the HOM radiation is at ~3 R_J from the planet, and on the L ~4-6 shells [*Reiner et al.*, 1993], and the source location of the KOM radiation is thought to be in the Io torus or above the polar ionosphere [cf. *Kaiser*, 1989]. Our data suggest that there were few turbulences in these locations.

By ground-based Jovian radio observation, the enhancement of the DIM synchrotron radiation was reported during the week of impacts (Figure 7.15) [cf. *Dulk et al.*, 1995; *Leblanc and Dulk*, 1995; *Klein et al.*, 1995; *Bolton et al.*, 1995]. The DIM radiation occurred near the Jovian magnetic equator at ~1-2 R_J from the planet, and is generated by relativistic electrons trapped in the Jovian magnetic field [cf. *Kaiser*, 1989]. These observations suggest that population of energetic electrons in the Jovian radiation belt increased in this term. On the other hand, ROSAT detected soft X-ray enhancement at the magnetic conjugate footprint of impact site just around K impact time (Figure 7.16) [*Waite et al.*, 1995]. It seems that bremsstrahlung X-ray radiation is produced by energetic electrons, which were accelerated at the impact site or precipitated from the radiation belt after being scattered with the ionized shock [cf. *Kellogg*, 1994]. These processes also account for the enhancement of synchrotron radiation through electron heating in the radiation belt. The impact sites are distributed on low L shells (L ~1.5-3). Therefore, we conclude that these turbulence were caused at or near these impact sites, and did not affect the outer magnetosphere on large L shells.

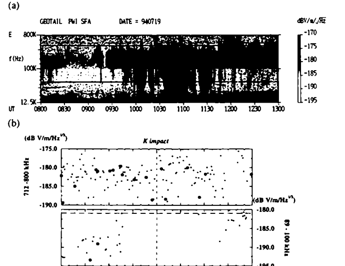

Figure 7.14: Radiation flux from the Jovian direction around the each impact time. (a) Frequency-Time spectrogram of 8-13 UT on July 19, around the K impact time (10:24 UT). Two faint enhancements around 800 kHz (10:26 UT, 10:55 UT) are solar type III radio bursts. (b) Radiation flux from the Jovian direction around the K impact time. Y-axis is radiation flux (dB $Vm^{-1}Hz^{-1/2}$). Upper and lower panels show the data at 712-800 kHz and 89-100 kHz, respectively. Small and large circles show the data from the omni-direction and from the Jovian direction, respectively. Dashed vertical line shows the K impact time. Long dashed horizontal line shows the background noise level. (c) Radiation flux around G, H, K, L, Q1, and S impact times. Other features are as same as in (b).

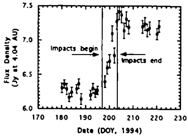

Figure 7.15: The intensity of Jovian DIM radio emission at 1665 MHz normalized to a distance of 4.04 AU [*Bolton et al.*, 1995]. Data points represent daily values of the total flux density including thermal and nonthermal components.

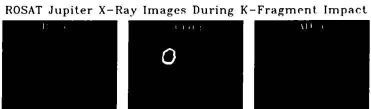

Figure 7.16: Jovian X-ray images before, during, and after the K impact (10:24 UT, July 19 1994) [*Waite et al.*, 1995].

There was another possible turbulence created by the passage of cometary fragments in the Jovian outer magnetosphere; increase of the charged particle population by trapping of plasma gas and/or charged dusts [*Herbert*, 1994], and generation of field-aligned current by dust-plasma [*Ip and Prangé*, 1994] and/or electrodynamical interaction [*Bolin and Brenning*, 1994; *Farrell et al.*, 1994]. The first may generate the activity increase for several weeks or months after the impact period, and the second and the third may provide the precursor radiation before the impact time of each fragment. Except for weak precursor feature of the HOM radiation, we find no clear variation of radio activity before and after the each impact time. This suggests that there are small amount of such direct interactions between the comet and Jovian outer magnetosphere. Since Io always induces radio activities through running in the Jovian magnetosphere accompanied by the plasma torus, we also conclude that the effect from the passage of cometary fragments seems to be weaker than from Io. In addition, in satellite observations with HST, IUE, and EUVE spacecraft, and ground-based radio observations, the Io plasma torus has not been significantly affected by either the comet fragments' passage through the magnetosphere or impact with Jupiter [cf. *McGrath et al.*, 1995; *Brown et al.*, 1995]. Since the Io plasma torus is one of the source regions of the KOM radiation, this is consistent with our results that no enhancement was found in the KOM radiation.

On the other hand, *Carr et al.* [1995] conclude from ground-based monitoring observations that there was no significant change in the Jovian decametric emission activity before, during, and after the impact period. This is consistent with our results, "The turbulence in the Jovian outer magnetosphere was weak.", because the DAM and HOM radiation are thought to be produced by the same cyclotron maser mechanism at different altitudes in the Jovian magnetosphere. However, it should be noted that the emission features of the DAM and HOM radiations are generally different. For example, the DAM radiation is controlled by Io location strongly, but the HOM radiation is not. Therefore, we need further observations to make this point clear.

7.2.5 Conclusion

GEOTAIL detected no clear enhancement of the Jovian non-thermal HOM and KOM radiation in the whole impacts' period. We find no change in features of the KOM radiation activity. On the other hand, there was a small decrease of the HOM radiation activity during the week of impacts, as well as small enhancement of the precursor activity accompanied with each impact. However, since these features are weaker than the galactic background radiation, we can not show a confident evidence. Jovian radiation during this period was weaker than ~ -180 dB $Vm^{-1}Hz^{-1/2}$ in the HOM radiation, and ~ -185 dB $Vm^{-1}Hz^{-1/2}$ in the KOM radiation.

Enhancement of X-ray [*Waite et al.*, 1995] and synchrotron radiation [cf. *Dulk et al.*, 1995; *Leblanc and Dulk*, 1995; *Klein et al.*, 1995; *Bolton et al.*, 1995] suggests the large turbulence in the Jovian inner magnetosphere associated with impacts of cometary fragments. However, our observation suggests that there was no clear activity variation in the Jovian outer magnetosphere. We conclude that there were few effects from mass loading or direct interactions between the cometary fragments and Jovian

Spacecraft	Year of Encounter	Closest Approach
Mariner 4 (USA)	1965	~13,200 km (flyby)
Mariner 6 (USA)	1970	flyby
Mariner 7 (USA)	1970	flyby
MARS 2 (USSR)	1971	~1,100 km (orbiter)
MARS 3 (USSR)	1971	~1,100 km (orbiter)
Mariner 9 (USA)	1972	flyby
MARS 5 (USSR)	1974	~1,800 km (orbiter)
Viking 1,2 (USA)	1976	landers
PHOBOS 2 (USSR)	1989	~850 km (orbiter)
Mariner 4 (USA)	1965	~13,200 km (flyby)
Mars Global Surveyor (USA)	1997	~380 km (orbiter)
PLANET-B (JAPAN)	1999	~150 km (orbiter)

Table 7.5: Summary of Mars measurements.

outer magnetosphere along the comet trajectory. This conclusion is consistent with no significant change of the DAM radiation monitored on the ground [cf. *Carr et al.*, 1995].

Although we did not get positive results, we could observe the first and perhaps the last unexpected events by a spacecraft observatory. It is needed to arrange a standing observatory in space.

7.3 Planetary missions in near future

Here, we summarize the spacecraft missions of Japan concerning to us in the near future; exploration of Mars and Moon. The present study is expected to contribute to them.

7.3.1 PLANET-B: Voyage toward Mars

The PLANET-B mission is the first Japanese exploration of Mars (Figure 7.17;Table 7.6) [*Tsuruda and Yamamoto*, 1995]. PLANET-B is scheduled for the launch in the summer of 1998 from Kagoshima Space Center. The arrival at Mars will be on October 1999. Collaborations with simultaneous Russian and US programs will mutually be beneficial and pursued.

The objectives are twofold. Scientific objectives are to study the structure and dynamics of the Martian upper atmosphere and its interaction with the solar wind. Except for the measurements by the two Viking landers, the Martian upper atmosphere has been left unexplored. The measurements by PLANET-B will shed light upon to our outer neighbor's upper atmosphere for the first time. Engineering objective is to develop basic technology for future planetary explorations. PLANET-B project is to overcome the mass limit by the development of light weight — high performance instruments. The technology developed in this challenge mission will become assets for the future planetary missions.

We participate in the Plasma Wave Analyzer (PWA) aboard the PLANET-B. The

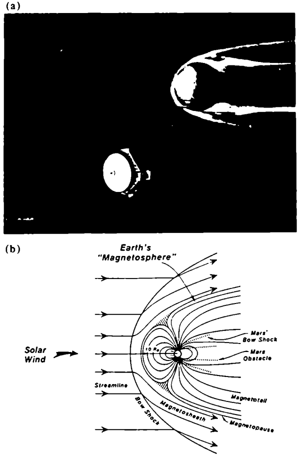

Figure 7.17: Planet-B, voyage toward Mars. (a) The spacecraft [*Tsuruda and Yamamoto*, 1995]. (b) The terrestrial and Martian magnetospheres [*Luhmann and Brace*, 1991].

Magnetic Field (MGF)	3-axis, 0.1 nT accuracy
Energetic Electrons (ESA)	5 eV – 22 keV
Energetic Ions (ISA)	10 eV – 20 keV/q
Energetic Ion Mass (IMI)	0.5 eV – 40 keV/q
High Energy Particles (EIS)	40 – 500 keV (e, p, He, O)
Thermal Ion Drift (TPA)	0.1 – 100 eV, drift velocity
Electron Temperature (PET)	Electron Temperature Probe
UV Spectra (UVS)	H, O, CO, CO_2, imaging, D/H ratio
Sounders and HF Waves (PWS)	Electron density profile, HF waves
Plasma Waves (LFA)	VLF/ELF waves
Visible Camera (MIC)	Visible image, 3 colors
Dust Counter (MDC)	Dust counter
EUV Spectrometer (XUV)	He^+ ion contents
Neutral Gas Mass (NMS)	Neutral gas mass spectrometer
Radio Science	Radio occultation measurement

Table 7.6: Scientific instruments of PLANET-B [*Tsuruda and Yamamoto*, 1995].

PWA is planned to investigate plasma wave measurements on the trajectories around Mars. The PWA consists of two instruments, 'Plasma Wave and Sounder experiment' (PWS) and 'Low Frequency wave Analyzer' (LFA). The PWS has the role to measure microscopic plasma wave phenomena by the high sensitive wave detector in the frequency range from 20 kHz to 7 MHz and the macroscopic plasma structure by the plasma sounder. On the other hand, the LFA takes the role of measuring plasma waves in the frequency range from DC to 30 kHz. The scientific objectives of the LFA are to study the wave phenomena related with the plasma dynamics in the different regions of the Martian ionosphere and magnetosphere, such as mass-loading and particle acceleration via wave-particle interactions. These observed data will be analyzed with reference of accumulated knowledge through studies of the terrestrial magnetosphere and ionosphere, including this thesis.

7.3.2 Moon project

Recently, 'Moon exploration program' is being planned as a joint mission of ISAS and NASDA in the early 2000's, following the LUNAR-A program which will be launched in 1997. This program aims to establish a bridgehead for future development of permanent bases on the Lunar surface.

We participate in the Lunar Radar Sounder Experiment (LRS) aboard the Lunar orbiter [*Ono et al.*, 1996]. The LRS is planned for radar sounding toward the surface and interior of Moon, to investigate evolution of Moon and exploration of natural resources, like ice at the polar region which is recently discovered. Since terrestrial and solar radio waves are concealed behind the Moon, the LRS also aims 'low frequency radio astronomy' from ~10 kHz to ~10MHz to investigate planetary, galactic, and extragalactic objects.

Chapter 8

Concluding Remarks

8.1 Summary

In this thesis, we presented numerous new facts which are found in huge observational data sets of the GEOTAIL spacecraft with the assistance of the WIND spacecraft and numerical simulations. Analyzed radio waves could provide real-time information around their sources and on their propagation paths to distant observers. These results showed the advantage of the spacecraft observations and the numerical simulations of low frequency radio waves to study fast and global phenomena in the geospace.

In Chapter 2, we investigated the terrestrial electron foreshock by remote observations of the $2f_p$ radio emission. We determined the geometry of the source of the $2f_p$ radiation by three methods; 'the two-spacecraft triangulation by collaboration with WIND'. 'the statistical analysis of direction finding', and 'the statistical analysis of bifurcation phenomena associated with solar wind density jump'. We found three points; (1) The $2f_p$ radio source is superposed on upstream and downstream wings of the electron foreshock. When the IMF displays a systematic rotation, the $2f_p$ radio source follows the motion of the electron foreshock. These results support the idea that the $2f_p$ radiation is generated in the electron foreshock from strong Langmuir waves. (2) The region close to the contact point is not bright source of the $2f_p$ radiation. This may be due to lack of a sharp electron beam in the region close to the contact point, because of a shortage of flight time to form sharp electron beams through the velocity filter process. (3) The distance of the source from the Earth is limited at a distance of 40–100 R_E. This may due to consumption of free energy of the electron beams.

In Chapter 3, we investigated physical conditions in the terrestrial electron foreshock by in-situ observations of $2f_p$ waves, other plasma waves, and energetic particles based on the results obtained in Chapter 2. First, we investigated global distributions of plasma waves and particles in the electron foreshock by mapping analysis. We found that the centroid of the $2f_p$ radiation source was on the IMF line tangent to the bow shock, at the distance of 5-40 R_E from the contact point. This suggested formation and consumption of sharp electron beams through time-of-flight effect and wave-particle interactions. We also found that the strength of the $2f_p$ radiation was positively correlated with solar wind kinetic flow and location of the contact point on the bow shock surface. These results suggested that the $2f_p$ radiation could work as a remote sensing probe to the population of energetic electron beams. On the other hand, we also investigated local physical properties on and across the electron foreshock. We confirmed that density of the quasi-beam component showed faster decrease than their kinetic energy. This favored the beam formation process through the time-of-flight effect. We also found the clear increase of plasma waves at $2f_p$ and below 1 kHz at the leading edge of the electron foreshock, associated with dramatic increase of Langmuir wave and energetic electrons. Upper limit of typical ratio of 'local' $2f_p$ wave to the Langmuir wave was ~ -40 dB, while that of low frequency electrostatic wave was ~ -10 dB.

In Chapter 4, we investigated the physical processes in the terrestrial electron foreshock by numerical simulations to generate electrostatic and electromagnetic $2f_p$ waves based on the results obtained in Chapter 2 and 3. Our numerical simulations were executed by electromagnetic particle code, KEMPO, in 1D and 2D periodic systems. In the 1D periodic systems, we generated electrostatic $2f_p$ waves associated with intense beam-excited Langmuir wave at $k = 2k_L$, where k_L is wave number of Langmuir wave. Growth of electrostatic $2f_p$ waves was strongly correlated with peak amplitude of Langmuir waves in ω-k space. These results supported the generation process of electrostatic $2f_p$ waves by wave–wave coupling of two of beam-excited Langmuir waves. Typical intensity ratio of electrostatic $2f_p$ waves to Langmuir wave was below -40 dB, which was consistent with in-situ observations presented in Chapter 3. On the other hand, we reproduced electromagnetic $2f_p$ waves in the 2D periodic system, Growth of electromagnetic $2f_p$ waves was strongly correlated with the amplitude of backscattered Langmuir waves, and independent of the electrostatic $2f_p$ waves. These features supported the generation process of electromagnetic $2f_p$ waves by wave–wave coupling between beam-excited and backscattered Langmuir waves. Typical intensity ratio of electromagnetic $2f_p$ waves to Langmuir wave was below -80 dB, which is too weak to detect enhancement of $2f_p$ waves at the leading edge of the electron foreshock.

In Chapter 5, we investigated global dynamics around the plasmapause during each substorms by remote observations of the continuum enhancement, short-lived enhancement of the nonthermal continuum radiation, generated at the plasmapause by injected electrons into the local midnight zone associated with substorm. We investigated three features; 'the occurrence conditions compared with the classical continuum', 'variation of the frequency range and source direction', and 'variation of the banded frequency and source direction'. We found three points; (1) The continuum enhancement and the following classical continuum are generated by a series of injected electrons associated with the same substorm onset. Dawnward motion of injected electrons caused by gradient and curvature drift supports such continuous variations of the continuum sources. (2) Sometimes the continuum enhancement consists of fast and main components distinguished by duration time and rising rate in frequency. Fast component is first generated by low energy electrons at the plasmapause in local midnight zone, while Main component is later generated by higher energy electrons on dawnside of the plasmapause. (3) Rising of spacing of banded frequency feature indicates decrease of the plasmapause radius for ~1 hour after substorm onsets. Converged radius of the plasmapause long after substorm is inversely correlated with Kp index. On the other hand, sometimes we also observed increase of the radius after finish of decrease. Since increase rate exceeds the value expected by refilling rate into the outer plasmasphere, decrease of the plasmapause radius is caused not only by peeling off of the plasma but also by relaxation of compression.

In Chapter 6, we investigated global dynamics in the auroral region by remote observations of AKR. We searched three factors which possibly affect generation and propagation conditions of AKR; 'the global magnetic disturbances', 'the longitude of the source region', and 'the angle between the geomagnetic axis and the Sun-Earth line'. Based on these analyses, we independently evaluated characteristics of generation and propagation conditions of AKR; (1) Extension of the illumination region of AKR is larger at lower frequency range. This feature should basically be explained by propagation of AKR, determined by difference of the source position and the propagation path. (2) In geomagnetic disturbed phase, the illumination region extends to more duskward at lower frequency than at higher frequency. This suggests that source region of AKR extends to duskward especially at high altitude. We suppose that such duskward extension is caused by blocking of the auroral plasma cavity formation at lower altitude by density increase of the duskside plasmasphere. (3) We find the dependence on the longitude of the source region especially at higher frequency range in the same manner as that of optical auroral activity. This suggests that the population of energetic electrons at lower altitude is controlled by altitude of the magnetic mirror point. Dependence at lower frequency should be suppressed by duskward extension of the source region. (4) From the dependence on the angle between the geomagnetic axis and the Sun-Earth line, we found that AKR is more active on the winter hemisphere especially at higher frequency range. Asymmetry of precipitating electron population which recently has been reported is a possible candidate. We also presented that an other possible candidate is blocking of the formation of the auroral plasma cavity on the summer hemisphere because of density increase of the inner plasmasphere.

In Chapter 7, we evaluated the applications of the techniques presented in the previous chapters to the planetary investigations. As an example of such studies, we investigated global dynamics in the Jovian magnetosphere associated with a first historic event, the impacts of Comet Shoemaker-Levy 9 (SL-9), by remote observations of the Jovian hectometric (HOM) and kilometric (KOM) radiations. Activities in X-ray and decimetric synchrotron radiations indicated strong perturbations at the impact sites have given non negligible changes in the inner magnetosphere, directly or indirectly. However, GEOTAIL detected no clear enhancement of the Jovian non-thermal HOM and KOM radiation in the whole impacts' period. This suggested that there was no clear variation in the Jovian outer magnetosphere induced by mass loading or direct interactions between the cometary fragments and Jovian outer magnetosphere along the comet trajectory. This conclusion was consistent with results of some ground-based DAM and optical observations.

We insisted that all the techniques presented in this thesis are not only applicable for further collaborations with other ground-based and ISTP satellites, but also for future missions. Especially in the future planetary explorations, these techniques will be able to reveal many features of global phenomena only by single spacecraft observations. In addition, physical processes presented in this thesis can be applied not only to the

	launch year	objective
MUSES-B	1996	radio astronomy (space VLBI)
LUNAR-A	1997	Moon
PLANET-B	1998	Mars
ASTRO-E	1999	X-ray & γ-ray astronomy
MUSES-C	2001	Asteroid (sample return)

Table 8.1: Future space mission of ISAS till 2001

	launch year	objective
COMETS	1997	communications and broadcasting engineering test
ETS-VII	1997	engineering test
TRMM	1997	tropical rain forest measuring
OICETS	1998	optical inter-orbit communications engineering test
ADEOS-II	1998	advanced earth observation
	1999	multipurpose transportation
JEM-1	1999	Japanese experiment module for space station
HOPE-X	2000	H-II orbiting plane
DRTS-W	2000	data relay and tracking satellite (W)
DRTS-E	2000	data relay and tracking satellite (E)
JEM-2	2000	Japanese experiment module for space station
ETS-VIII	2001	engineering test
ALOS	2001	advanced land observation

Table 8.2: Future space mission of NASDA till 2001

planetary world but also other astrophysical and laboratory phenomena concerning the plasma porcesses.

8.2 Future space studies

Today, various national space missions for both practical and scientific purposes are in preparation. Table 8.1 and Table 8.2 show space missions of ISAS and NASDA in the near future.

Increase of the space activities will inevitably include large number of the participants in the various fields in different disciplines. Future space missions should spread over three fields; scientific, technological, and social activities.

In the scientific fields, we should further expand both observational methods and interdisciplinary collaborations. In this thesis, we mainly owed to information of low frequency radio waves, electric and magnetic fields, and energetic particles in the planetary magnetospheres. We hope UV imaging technique using helium emission lines excited by solar UV emission to direct comparison with radio wave observations, and also introduce methods of astronomical investigations to study planetary phenomena. In addition, we should expand research field which is not sufficiently investigated. One example is low frequency radio astronomy toward the planetary, galactic, and extragalactic objects (Table 8.3). This is the most possible by arrays at the back of the moon from the Earth where intense solar and terrestrial radiations are completely shielded. The other example is precursor radio waves accompanied with large earthquakes. Re-

	Frequency Range	Short Description
LFVLA	10, 30, 75 MHz	extension of VLA
OLFRAS	1, 5, 13, 30, 75 MHz	A satellite for synthesis with ground-based arrays
LORAE	15 kHz to 30 MHz	One or more Lunar orbiters with one or more dipoles
LFSA	1, 5, 13, 26 MHz	An orbiting array in high earth orbit
Near Side Lunar Array	150 kHz to 30 MHz	At the first lunar outpost
Far Side Lunar Array	150 kHz to 30 MHz	Based on routine presence of human on the Moon

Table 8.3: Programs proposed for future low frequency radio astronomy [cf. *Kassim and Weiler*, 1990]

cently, some observations are reported such radio waves associated with release of large energy in the underground [cf. *Molchanov et al.*,, 1993]. Some satellite programs are beginning to be planned now. We should pay attention not only to the capability of remote and real-time observations of these phenomena, but also the other possibility of same kinds of detection at the other planetary objects.

In the technological aspects, we should contribute space technology based on the radio waves and communications. Improvement of capacity of communications, autonomous control of distant instruments, and automatic recognition of complicated information are essential to develop the space around the Earth and extend the human activities toward the planetary space.

On the social effects, we should pay attention that 'autarky' is completely becoming anachronism, and space development by a closed club of advanced countries will also crash against the limit. Since space development originally has a face of an international enterprise for future civilization, we should operate it under supports of whole human beings. Such movement is also contribute to harmonize neighbor countries. This is already displayed in Europe, as organizing of European Space Agency (ESA). Since space programs inevitably need long preparation and large number of participants, wide collaborations with neighboring countries will strongly contribute the steady constructions of concrete human relations and the harmonization of international relations.

Although contributions of individual works are limited, these studies will be devoted to the progress of whole human activities in the future civilization.

References

Ackerson, K. L., and L. A. Frank, Correlated satellite measurements of low-energy electron precipitation and ground-based observations of a visible auroral arc, *J. Geophys. Res.*, *77*, 1128, 1972.

Akimoto, K., H. L. Rowland, and K. Papadopoulos, Electromagnetic radiation from strong Langmuir turbulence, *Phys. Fluids*, *31*, 2185, 1983.

Alexander, J. K., and M. L. Kaiser, Terrestrial kilometric radiation, 1. Spatial structure studies, *J. Geophys. Res.*, *81*, 5948, 1976.

Anderson, K. A., R. P. Lin, F. Martel, C. S. Lin, G. K. Parks, and H. Réme, Thin sheets of energetic electrons upstream from the Earth's bow shock, *Geophys. Res. Lett.*, *6*, 401, 1979.

Anderson, K. A., Measurements of the bow shock particles far upstream from the Earth, *J. Geophys. Res.*, *86*, 4445, 1981.

Anderson, R. R., G. K. Parks, T. E. Eastman, D. A. Gurnett, and L. A. Frank, Plasma waves associated with energetic particles streaming into the solar wind from the Earth's bow shock, *J. Geophys. Res.*, *86*, 4493, 1981.

Bahnsen A., M. Jespersen, E. Ungstrup, and I. B. Iversen, Auroral hiss and kilometric radiation measured from the Viking satellite, *Geophys. Res. Lett.*, *14*, 471, 1987.

Benson, R. F., and W. Calvert, ISIS 1 observations at the source of auroral kilometric radiation, *Geophys. Res. Lett.*, *6*, 479, 1979.

Benson R. F., W. Calvert, and D. M. Klumpar, Simultaneous wave and particle observations in the auroral kilometric radiation source region, *Geophys. Res. Lett.*, *7*, 959, 1980.

Benson R. F., and S.-I. Akasofu, Auroral kilometric radiation/aurora correlation, *Radio Sci.*, *19*, 527, 1984.

Binsack, J. H., and V. M. Vasyliunas, Simultaneous IMP 2 and OGO 1 observations of bow shock compression, *J. Geophys. Res.*, *73*, 429, 1968.

Bolin, O., and N. Brenning, Electrodynamical interaction between comet Shoemaker-Levy 9 and Jupiter, *Geophys. Res. Lett.*, *21*, 1063, 1994.

Bolton, S. J., R. S. Foster, and W. B. Waltman, Observations of Jupiter's synchrotron radiation at 18 cm during the Comet Shoemaker-Levy 9 impacts, of Comet Shoemaker-Levy 9, *Geophys. Res. Lett.*, *22*, 1801, 1995.

Bougeret, J.-L., et al., WAVES: The radio and plasma wave investigation on the WIND spacecraft, *Space Science Reviews*, *71*, 231, 1995.

Brown, L. W., The galactic radio spectrum between 130 and 2600 kHz, *Astrophys. J.*, *180*, 359, 1973.

Brown, L. W., Spectral behavior of Jupiter near 1 MHz, *Astrophys. J.*, *194*, L159, 1974.

Brown, M. E., E. J. Moyer, A. H. Bouchez, and H. Spinrad, Comet Shoemaker-Levy 9: No effect on the Io plasma torus, *Geophys. Res. Lett.*, *22*, 1833, 1995.

Cairns, I. H., and D. B. Melrose, A theory for the $2f_p$ radiation upstream of the Earth's bow shock, *J. Geophys. Res.*, *90*, 6637, 1985.

Cairns, I. H., A semiquantitative theory for the $2f_p$ radiation observed upstream from the Earth's bow shock, *J. Geophys. Res.*, *93*, 3958, 1988.

Calvert, W., The auroral plasma cavity, *Geophys. Res. Lett.*, *8*, 919, 1981.

Carpenter, D. L., Whistler studies of the plasmapause in the magnetosphere, 1. Temporal variations in the position of the knee and some evidence on plasma motions near the knee, *J. Geophys. Res.*, *71*, 693, 1966.

Carpenter, D. L., and R. R. Anderson, An ISEE/Whistler model of equatorial electron density in the magnetosphere, *J. Geophys. Res.*, *97*, 1097, 1992.

Carr, T. D., M. D. Desch, and J. K. Alexander, Phenomenology of magnetospheric radio emissions, in *Jupiter*, edited by E. J. Dessler, 226, Cambridge University Press, New York, 1983.

Carr, T. D., F. Reyes, J. A. Phillips, J. May, L. Wang, J. Aparici, H. Alvarez, F. Olmos, L. Garcia, J. M. De Buizer, W. B. Greenman, T. Clark, J. Levy, S. Padin, and C. A. Higgins, Results of decametric monitoring of the comet collision with Jupiter, *Geophys. Res. Lett.*, *22*, 1785, 1995.

Chapman, S., The absorption and dissociative or ionizing effect of monochromatic radiation in an atmosphere on rotating Earth, *Proc. Phys. Soc.*, *43*, 26, 1931.

Chappell, C. R., K. K. Harris, and G. W. Sharp, A study of the influence of magnetic activity on the location of the plasmapause as measured by OGO 5, *J. Geophys. Res.*, *75*, 50, 1970.

Chappell, C. R., K. K. Harris, and G. W. Sharp, The dayside of the plasmasphere, *J. Geophys. Res.*, *76*, 7632, 1971.

Crawford, G. K., R. J. Strangeway, and C. T. Russell, VLF imaging of the Venus foreshock, *Geophys. Res. Lett.*, *20*, 2801, 1993.

DeForest, S. E., and C. E. McIlwain, Plasma clouds in the magnetosphere, *J. Geophys. Res.*, *76*, 3587, 1971.

de Pater, I., The effect of comet Shoemaker-Levy 9 on Jupiter's synchrotron radiation, *Geophys. Res. Lett.*, *21*, 1071, 1994.

Desch, M. D., and T. D. Carr, Decametric and hectometric observations of Jupiter from the RAE-1 satellite, *Astrophys. J.*, *194*, L57, 1974.

Desch, M. D., and M. L. Kaiser, Predictions for Uranus from a radiometric Bode's law, *Nature*, *310*, 5980, 1984.

Desch, M. D., M. L. Kaiser, W. M. Farrell, R. J. MacDowall, and R. G. Stone, Traversal of comet SL-9 through the Jovian magnetosphere and impact with Jupiter: Radio upper limits, *Geophys. Res. Lett.*, *22*, 1781, 1995.

Dulk, G. A., Y. Leblanc, and R. W. Hunstead, Flux and images of Jupiter at 13, 2, and 36 cm before, during, and after SL9 impacts, *Geophys. Res. Lett.*, *22*, 1789, 1995.

Ejiri, M., Trajectory traces of charged particles in the magnetosphere, *J. Geophys. Res.*, *83*, 4798, 1978.

Etcheto, J., and M. Faucheux, Detailed study of electron plasma waves upstream of Earth's bow shock, *J. Geophys. Res.*, *89*, 6631, 1984.

Farrell, W. M., M. L. Kaiser, M. D. Desch, and R. J. MacDowall, Possible radio wave precursors associated with the comet Shoemaker-Levy 9/Jupiter impacts, *Geophys. Res. Lett.*, *21*, 1067, 1994.

Farrell, W. M., M. L. Kaiser, M. D. Desch, and R. J. MacDowall, Possible radio wave precursors associated with the comet Shoemaker-Levy 9/Jupiter impacts, *Geophys. Res. Lett.*, *21*, 1067, 1994.

Filbert, P. C., and P. K. Kellogg, Electrostatic noise at the plasma frequency beyond the Earth's bow shock, *J. Geophys. Res.*, *84*, 1369, 1979.

Filbert, P. C., and P. J. Kellogg, Observations of low-frequency radio emissions in the Earth's magnetosphere, *J. Geophys. Res.*, *94*, 8867, 1989.

Fitzenreiter, R. J., The electron foreshock, *Adv. Space Res.*, *15*, 9, 1995.

Galperin, Yu. I., V. S. Soloviev, K. Torkar, J. C. Foster, and M. V. Veselov, Predicting plasmaspheric radial density profiles, *J. Geophys. Res.*, in printing, 1996.

Gough, M. P., Nonthermal continuum emissions associated with electron injections: Remote plasmapause sounding, *Planet. Space Sci.*, *30*, 657, 1982.

Green, J. L., D. A. Gurnett, and S. D. Shawhan, The angular distribution of auroral kilometric radiation, *J. Geophys. Res.*, *82*, 1825, 1977.

Greenstadt, E. W., and R. W. Fredricks, Shock systems in collisionless space plasmas, in *Solar System Plasma Physics*, *vol.3*, edited by L. J. Lanzerotti, C. F. Kennel, and E. N. Parker, 3, North-Holland, Amsterdam, 1979.

Greenstadt, E. W., G. K. Crawford, R.J. Strangeway, S. L. Moses, and F. V. Coroniti, Spatial distribution of electron plasma oscillations in the Earth's foreshock at ISEE 3, *J. Geophys. Res.*, *100*, 19933, 1995.

Gurnett, D. A., and R. R. Shaw, Electromagnetic radiation trapped in the magnetosphere above the plasma frequency, *J. Geophys. Res.*, *78*, 8136, 1973.

Gurnett, D. A., The Earth as a radio source: Terrestrial kilometric radiation, *J. Geophys. Res.*, *79*, 4227, 1974.

Gurnett, D. A., The Earth as a radio source: The nonthermal continuum, *J. Geophys. Res.*, *80*, 2751, 1975.

Gurnett, D. A., and L. A. Frank, Continuum radiation associated with low-energy electrons in the outer radiation zone, *J. Geophys. Res.*, *81*, 3875, 1976.

Gurnett, D. A., and R. R. Anderson, Plasma wave electric fields in the solar wind: Initial results from Helios 1, *J. Geophys. Res.*, *82*, 632, 1977.

Gurnett, D. A., Plasma waves and instabilities, in *Collisionless shocks*, *Geophysical Monograph*, *35*, edited by B. T. Tsurutani and R. G. Stone, 207, 1985.

Hashimoto, K., Reconciliation of propagation modes of auroral kilometric radiation, *J. Geophys. Res.*, *89*, 7459, 1984.

Herbert, F., The impact of Comet Shoemaker-Levy 9 on the Jovian magnetosphere, *Geophys. Res. Lett.*, *21*, 1047, 1994.

Hoang, S., Fainberg, J., J.-L. Steinberg, R. G. Stone, and R. H. Zwickl, The $2f_p$ circumterrestrial radio radiation as seen from ISEE 3, *J. Geophys. Res.*, *86*, 4531, 1981.

Horányi, M., New Jovian ring ?, *Geophys. Res. Lett.*, *21*, 1039, 1994.

Huff, R. L., W. Calvert, J. D. Craven, L. A. Frank, and D. A. Gurnett, Mapping of auroral kilometric radiation sources to the aurora, *J. Geophys. Res.*, *93*, 11445, 1988.

Ip, W.-H., and R. Prangé, On possible magnetospheric dust interactions of comet Shoemaker-Levy 9 at Jupiter, *Geophys. Res. Lett.*, *21*, 1051, 1994.

Jones, D., Source of terrestrial non-thermal radiation, *Nature*, *260*, 225, 1976.

Jones, D., Non thermal continuum radiation at the radio planets, in *Planetary radio emissions*, edited by H. O. Rucker and S. J. Bauer, Österreichische Akademie der Wissenschaften, Wien, 1985.

Kainer, S., J. Dawson, R. Shanny, and T. Coffey, Interaction of a highly energetic electron beam with a dense plasma, *Phys. Fluids*, *15*, 493, 1972.

Kaiser, M. L., and J. K. Alexander, Terrestrial kilometric radiation 3. Average spectral properties, *J. Geophys. Res.*, *82*, 3273, 1977.

Kaiser, M. L., Observations of non-thermal radiation from planets, in *Plasma Waves and Instabilities at Comets and in Magnetospheres*, edited by B. T. Tsurutani and H. Oya, *Geophys. Monogr.*, *53*, 221, AGU, Washington, D. C., 1989.

Kaiser, M. L., Time-variable magnetospheric radio emissions from Jupiter, *J. Geophys. Res.*, *98*, 18757, 1993.

Kaiser, M. L., M. D. Desch, W. M. Farrell, J.-L. Steinberg, and M. J. Reiner, LF band terrestrial radio bursts observed by WIND/WAVES, *Geophys. Res. Lett.*, *23*, 1287, 1996.

Kasaba, Y., H. Kojima, H. Matsumoto, and T. Murata, Search for Jovian hectometric and kilometric radiation by GEOTAIL spacecraft during the impact of comet Shoemaker-Levy 9, *J. Geomag. Geoelectr.*, *48*, 361-370, 1996.

Kasaba, Y., H. Matsumoto, and R. R. Anderson, GEOTAIL observation of $2f_p$ emission around the terrestrial foreshock region, *Advanced Space Research*, accepted, 1997.

Kassim, N. E., and K. W. Weiler, in *Low Frequency Astrophysics from Space, Proceedings of an International Workshop*, edited by N. E. Kassim and K. W. Weiler, Lecture Notes in Physics, 362, Springer-Verlag, Berlin, 1990.

Kellogg, P. J., Plasma effects on the interaction of a comet with Jupiter, *Geophys. Res. Lett.*, *21*, 1055, 1994.

Kellogg, P. J., S. J. Monson, K. Goetz, R. L. Howard, J.-L. Bougeret, and M. L. Kaiser, Early wind observations of bow shock and foreshock waves, *Geophys. Res. Lett.*, *23*, 1243, 1996.

Klein, M. J., S. Gulkis, and S. J. Bolton, Changes in Jupiter's 13-cm synchrotron radio emission following the impact of Comet Shoemaker-Levy 9, *Geophys. Res. Lett.*, *22*, 1797, 1995.

Klimas, A. J., A mechanism for plasma waves at the harmonics of the plasma frequency in the electron foreshock boundary, *J. Geophys. Res.*, *88*, 9081, 1983.

Kojima, H., H. Matsumoto, S. Chikuba, S. Horiyama, M. Ashour-Abdalla, R. R. Anderson, GEOTAIL Waveform Observations of Broadband/Narrowband Electrostatic Noise in the Distant Tail, *J. Geophys. Res.*, accepted, 1996.

Kokubun, S., T. Yamamoto, M. Acũna, K. Hayashi, K. Shiokawa, and H. Kawano, The Geotail magnetic field experiment, *J. Geomag. Geoelectr.*, *46*, 7, 1993.

Krimigis, S. M., T. P. Armstrong, W. I. Axford, C. O. Bostrom, C. Y. Fan, G. Gloeckler, L. J. Lanzerotti, E. P. Keath, R. D. Zwickl, J. F. Carbary, and D. C. Hamilton, Hot plasma environment at Jupiter: Voyager 2 results, *Science*, *206*, 977, 1979.

Kurth, W. S., M. M. Baumback, and D. A. Gurnett, Direction-finding measurements of auroral kilometric radiation, *J. Geophys. Res.*, *80*, 2764, 1975.

Kurth, W. S., D. A. Gurnett, and R. R. Anderson, Escaping nonthermal continuum radiation, *J. Geophys. Res.*, *86*, 5519, 1981.

Lacombe, C., C. C. Harvey, S. Hoang, A. Mangeney, J.-L. Steinberg and D. Burgess, ISEE observations of emission at twice the solar wind plasma frequency, *Ann. Geophys.*, *6*, 1, 113, 1988.

Leblanc, Y., and G. A. Dulk, Changes in brightness of Jupiter's radiation belts at 13 and 22 cm during and after impacts of Comet SL9, *Geophys. Res. Lett.*, *22*, 1793, 1995.

Lecacheux, A., B. M. Pedersen, Ph. Zarka, M. G. Aubier, M. D. Desch, W. M. Farrell, M. L. Kaiser, R. J. MacDowall, and R. G. Stone, In ecliptic observations of Jovian radio emissions by Ulysses comparison with Voyager results, *Geophys. Res. Lett.*, *19*, 1307, 1992.

Lee, L. C., Theories of non-thermal radiations from planets, in *Plasma Waves and Instabilities at Comets and in Magnetospheres*, edited by B. T. Tsurutani and H. Oya, *Geophys. Monogr.*, *53*, 239, AGU, Washington, D. C., 1989.

Lepping, R. P., M. H. Acũna, L. F. Burlaga, W. M. Farrell, J. A. Slavin, K. H. Schatten, F. Mariani, N. F. Ness, F. M. Neubauer, Y. C. Whang, J. B. Byrnes, R. S. Kennon, P. V. Panetta, J. Scheifele, and E. M. Worley, The WIND magnetic field investigation, *Space Science Reviews*, *71*, 207, 1995.

Leroy, M. M., and A. Mangeney, A theory of energization of solar wind electrons by the Earth's bow shock, *Ann. Geophys.*, *2*, 4, 449, 1984.

Luhmann, J. G., and L. H. Brace, Near-Mars space, *Reviews of Geophysics*, *29*, 121, 1991.

MacDowall, R. J., R. G. Stone, and J. D. Gaffey, Jr., Remote observations of solar wind parameters upstream of planetary bowshocks, *Solar Wind 7, Proceedings*, Ed. E. Marsch and R. Schwenn, Pergamon Press, Oxford, 647, 1992.

MacDowall, R. J., R. G. Stone, and J. D. Gaffey, Jr., Detection of $2f_p$, radio emission from the Jovian electron foreshock by the Ulysses spacecraft, *American Geophysical Union, Spring meeting*, 1993.

Maeda, K., N. K. Bewtra, and P. H. Smith, Ring current electron trajectories associated with VLF emissions, *J. Geophys. Res.*, *83*, 4339, 1978.

Manning, R., and J. Fainberg, A new method of measuring radio source parameters of a partially polarized distributed source from spacecraft observations, *Space Science Instrumentation*, *5*, 161, 1980.

Matsumoto, H., and Y. Omura, Particle simulations of electromagnetic waves and their applications to space plasmas, *Computer Simulations of Space Plasmas*, edited by H. Matsumoto and T. Sato, Terra Pub. and Reidel Co., 1985.

Matsumoto, H., I. Nagano, R. R. Anderson, H. Kojima, K. Hashimoto, M. Tsutsui, T. Okada, I. Kimura, Y. Omura, and M. Okada, Plasma wave observations with GEOTAIL spacecraft, *J. Geomag. Geoelectr.*, *46*, 59, 1994.

Matsumoto, H., H. Kojima, Y. Kasaba, T. Miyake, R. R. Anderson, and T. Mukai, Plasma waves in the upstream and bow shock regions observed by GEOTAIL, *Advanced Space Research*, accepted, 1997.

McGrath, P. J., D. T. Hall, P. L. Matheson, H. A. Weaver, J. T. Trauger, T. E. Smith, N. Thomas, R. Glabstone, N. M. Schneider, W. M. Harris, T. A. Livengood, R. Prangé, and M. C. Festou, Response of the Io plasma torus to Comet Shoemaker-Levy 9, *Science*, *267*, 1313, 1995.

Mellott, M. M., and W. A. Livesey, Shock overshoots revisited, *J. Geophys. Res.*, *92*, 13661, 1989.

Miki, N., Y. Omura, T. Mukai, H. Matsumoto, H. Kojima, R. R. Anderson, Y. Saito, and S. Kokubun, Comparison between electron velocity distribution functions and electrostatic waves observed by GEOTAIL, *Chapman Conference on The Earth's Magnetotail: New Perspectives*, Kanazawa, Japan, Nov. 1996.

Molchanov, O. A., O. A. Mazhaeva, A. N. Goliavin, and M. Hayakawa, Observation by the Intercosmos-24 satellite of ELF-VLF electromagnetic emissions associated with earthquakes, *Ann. Geophysicae*, *11*, 431, 1993.

Mukai, T., S. Machida, Y. Saito, M. Hirahara, T. Terasawa, N. Kaya, T. Obara, M. Ejiri, and A. Nishida, The low energy particle (LEP) experiment onboard the GEOTAIL satellite, *J. Geomag. Geoelectr.*, *46*, 669, 1994

Murata, T., Study of magnetotail dynamics via computer experiments and spacecraft observations, *Ph. D. thesis, Kyoto University*, 1995.

Muschietti, L., and C. T. Dum, Nonlinear wave scattering and electron beam relaxation, *Phys. Fluids*, *B3*, 1968, 1991.

Ness, N. F., K. W. Behannon, R. P. Lepping, Y. C. Whang, and K. H. Schatten, Magnetic field observations near Mercury: Preliminary results from Mariner 10, *Science*, *185*, 151, 1974.

Newell, P. T., C.-I. Meng, and K. M. Lyons, Suppression of discrete aurorae by sunlight, *Nature*, *381*, 766, 1996.

Nishida, A., The GEOTAIL mission, *Geophys. Res. Lett.*, *21*, 2871, 1994.

Ogilvie, K. W., D. J. Chornay, R. J. Fitzenreiter, E. Hunsaker, J. Keller, J. Lobell, G. Miller, J. D. Scudder, E. C. Sittler, Jr., R. B. Torbert, D. Bodet, G. Needell, A. J. Lazarus, J. T. Steinberg, J. H. Tappan, A. Mavretic, and E. Gergin, SWE, a comprehensive plasma instrument for the WIND spacecraft, *Space Science Reviews*, *71*, 55, 1995.

Ogilvie, K. W., and G. K. Parks, First results from WIND spacecraft: An introduction, *Geophys. Res. Lett.*, *23*, 1179, 1996.

Okuda, H., M. Ashour-Abdalla, M. S. Chance, and W. S. Kurth, Generation of nonthermal continuum radiation in the magnetosphere, *J. Geophys. Res.*, *87*, 10457, 1982.

Ono, T., H. Oya, T. Kobayashi, A. Morioka, K. Hashimoto, A. Yamaji, Y. Yamaguchi, and S. Sasaki, A proposed plan of the Lunar Radar Sounder Experiment from a Moon orbit, *Society of Geomagnetism and Earth, Planetary, and Space Sciences 1996 fall meeting*, Fuchu, Tokyo, Oct. 1996.

Nishikawa, K.-I., and I. H. Cairns, Simulation of the nonlinear evolution of electron plasma waves, *J. Geophys. Res., 96*, 19343, 1995.

Persoon, A. M., D. A. Gurnett, W. K. Peterson, J. H. Waite, Jr., J. L. Burch, and J. L. Green, Electron density depletions in the nightside auroral zone, *J. Geophys. Res., 93*, 1871, 1988.

Pritchett, P. L., and J. M. Dawson, Electromagnetic radiation from beam-plasma instabilities, *Phys. Fluids, 26*, 1114, 1983.

Reiner, M. J., J. Fainberg, and R. G. Stone, Source characteristics of Jovian hectometric radio emissions, *J. Geophys. Res., 98*, 18767, 1993.

Reiner, M. J., M. L. Kaiser, J. Fainberg, M. D. Desch, and R. G .Stone, 2fp radio emission from the vicinity of the Earth's foreshock: WIND observations, *Geophys. Res. Lett., 23*, 1247, 1996.

Rycroft, M. J., Some aspects of geomagnetically conjugate phenomena, *Annals Geophysics., 5A*, 463, 1987.

Sagan, C., *COSMOS (in Japanese)*, Asahi Shinbun, Tokyo, 1980.

Shawhan, S. D., Magnetospheric plasma waves, in *Solar System Plasma Physics vol. III*, edited by I. J. Lanzerotti, C. F. Kennel, and E. H. Parker, 213, 1979.

Slavin, J. A., A. Szabo, M. Peredo, R. P. Lepping, R. J. Fitzenreiter, K. W. Ogilvie, C. J. Owen, and J. T. Steinberg, Near-simultaneous bow shock crossings by WIND and IMP 8 on December 1, 1994, *Geophys. Res. Lett., 23*,, 1207, 1996.

Sonnerup, B. U. Ö., Solar wind interaction with planetary magnetic fields, In *Future Missions in Solar, Heliospheric and Space Plasma Physics*, edited by E. Rolfe and B. Battrick, 53, ESA, Noordwijk, 1985.

Spreiter, J. R., A. L. Summers, and A. Y. Alksne, Hydromagnetic flow around the magnetospheres, *Planet. Space Sci., 14*, 233, 1966.

Steinberg, J.-L., and S. Hoang, Electric noise observations with the ISEE-3 radio receiver: thermal noise and the $2f_p$ line from the Lagrange point to 14 R_E from the Earth, *Ann. Geophysicae, 4A*, 429, 1986.

Stenback-Nielsen, H. C., T. N. Davis, and N. W. Glass, Relative motion of auroral conjugate points during substorms, *J. Geophys. Res., 77*, 1844, 1973.

Stone, R. G., J. L. Bougeret, J. Caldwell, P. Canu, Y. de Conchy, N. Cornilleau-Wehrlin, M. D. Desch, J. Fainberg, K. Goetz, M. L. Goldstein, C. C. Harvey, S. Hoang, R. Howard, M. L. Kaiser, P. J. Kellogg, B. Klein, R. Knoll, A. Lecacheux, D. Lengyel-Frey, R.J. MacDowall, R. Manning, C. A. Meetre, A. Meyer, N. Monge, S. Monson, G. Nicol, M. J. Reiner, J.-L. Steinberg, E. Torres, C. de Villedary, F. Wouters, and P. Zarka, The unified radio and plasma wave investigation, *Astron. Astrophys. Suppl. Ser., 92*, 291, 1992.

Thejappa, G., D. G. Wentzel, and R. G. Stone, Low-frequency waves associated with Langmuir waves in solar wind, *J. Geophys. Res., 100*, 3417, 1995.

Tsuruda, K., and T. Yamamoto, *Planet-B Interim Report*, SES Data Center, The Institute of Space and Astronautical Science, 1995.

Tsytovich, V. N., *Nonlinear Effects in Plasmas*, Plenum, New York, 1970.

Voots, G. R., D. A. Gurnett, and S.-I. Akasofu, Auroral kilometric radiation as an indicator of auroral magnetic disturbances, *J. Geophys. Res., 82*, 2259, 1977.

Waite, Jr., J. H., G. R. Gladstone, K. Franke, W. S. Lewis, A. C. Fabian, W. N. Brandt, C. Na, F. Haberl, J. T. Clarke, K. C. Hurley, M. Sommer, and S. Bolton, ROSAT observations of X ray emissions from Jupiter during the impact of Comet Shoemaker-Levy 9, *Science, 268*, 1598, 1995.

Warwick, J. W., D. R. Evans, J. H. Romig, J. K. Alexander, M. D. Desch, M. L. Kaiser, M. Aubier, Y. Leblanc, A. Lecacheux, and B. M. Pedersen, Planetary radio astronomy observations from Voyager 2 near Saturn, *Science*, *215*, 582, 1982.

Wu, C. S., and L. C. Lee, A theory of the terrestrial kilometric radiation, *Astrophys. J.*, *230*, 621, 1979.

Wu, C. S., A fast Fermi process: energetic electrons accelerated by a nearly perpendicular bow shock, *J. Geophys. Res.* *89*, 8857, 1984.

Wu, C. S., Kinetic cyclotron and synchrotron maser instabilities: Radio emission processes by direct amplification of radiation, *Space Sci. Rev.*, *41*, 215, 1985.

Yeomans, D. K., and P. W. Chodas, *private communication*, 1995.

Yoon, P. H., C. S. Wu, A. F.-Vinus, M. J. Reiner, J. Fainberg, and R. G. Stone, *J. Geophys. Res.*, *99*, 23481, 1994.

Publication List

Publication Papers

1. Ito, M., Y. Kasaba, M. Ueno, S. Sato, and M. Kimata, Evaluation of a 512x512-element platinum silicide Schottky-barrier infrared image sensor and pilot observations of the Cygnus X region, *Pub. Astro. Soc. Pac., 107*, 691-701, 1995.
2. Kasaba, Y., H. Kojima, H. Matsumoto, and T. Murata, Search for Jovian hectometric and kilometric radiation by GEOTAIL spacecraft during the impact of comet Shoemaker-Levy 9, *J. Geomag. Geoelectr., 48*, 361-370, 1996.
3. Kasaba, Y., H. Matsumoto, and R. R. Anderson, GEOTAIL observation of $2f_p$ emission around the terrestrial foreshock region, *Advanced Space Research*, accepted, 1997.
4. Matsumoto, H., H. Kojima, Y. Kasaba, T. Miyake, R. R. Anderson, and T. Mukai, Plasma waves in the upstream and bow shock regions observed by GEOTAIL, *Advanced Space Research*, accepted, 1997.
5. Reiner, M. J., Y. Kasaba, M. L. Kaiser, H. Matsumoto, I. Nagano, and J.-L. Bougeret, $2f_p$ radio source location determined from WIND/GEOTAIL triangulation, *Geophys. Res. Lett.*, submitted, 1997.
6. Anderson, R. R., D. A. Gurnett, H. Matsumoto, K. Hashimoto, H. Kojima, Y. Kasaba, M. L. Kaiser, G. Rostoker, J.-L. Steinberg, I. Nagano, and H. J. Singer, Observations of low frequency terrestrial type III bursts by GEOTAIL and WIND and their association with geomagnetic disturbances detected by ground and space-borne instruments, *Geophys. Res. Lett.*, submitted, 1997.
7. Murata, T., H. Matsumoto, H. Kojima, T. Iyemori, T. Nagai, and Y. Kasaba, Proposal of a new index for substrom study: AKR index, *J. Geophys. Res.*, submitted, 1997.
8. Kasaba, Y., H. Matsumoto, K. Hashimoto, and R. R. Anderson, The angular distribution of auroral kilometric radiation observed by GEOTAIL spacecraft, *Geophys. Res. Lett.*, submitted, 1997.
9. Kasaba, Y., H. Matsumoto, K. Hashimoto, R. R. Anderson, J.-L. Bougeret, M. L. Kaiser, X. Y. Wu, and I. Nagano, Remote sensing of the plasmapause during substorm: GEOTAIL observation of the continuum enhancement, *J. Geophys. Res.*, to be submitted, 1997.
10. Kasaba, Y., H. Matsumoto, R. R. Anderson, T. Mukai, Y. Saito, Y. Omura, T. Yamamoto, and S. Kokubun, Plasma waves and energetic particles in and around the terrestrial electron foreshock observed by GEOTAIL spacecraft, *J. Geophys. Res.*, to be submitted, 1997.
11. Kasaba, Y., H. Matsumoto, and Y. Omura, Numerical simulations of electrostatic and electromagnetic $2f_p$ waves, *J. Geophys. Res.*, to be submitted, 1997.

Proceeding Papers

1. Ueno, M., M. Ito, Y. Kasaba, and S. Sato, Astronomical application of 512x512 PtSi infrared image sensor, *Proceeding of SPIE conference vol. 1762, Infrared Technology XVIII*, 423-430, 1992.
2. Ueno, M., T. Ichikawa, S. Sato, Y. Kasaba, and M. Ito, Near-infrared survey of the central 12 square degrees of the Galaxy, *AIP conference Proceeding vol. 278, Back to the Galaxy*, 64-66, 1993.
3. Ueno, M., T. Ichikawa, S. Sato, Y. Kasaba, and M. Ito, Near infrared survey of the Galactic Center with 512x512 PtSi camera, in *Infrared Astronomy with Arrays: The Next Generation*, edited by I. McLean, Kluwer Academic Publishers, 119-120, 1994.

Oral Papers

1. Kasaba, Y., T. Ohtani, M. Nishida, and T. Ichikawa, JHK images of Seyfert galaxy NGC7469, *Astronomical Society of Japan 1989 Spring Meeting*, Tokyo, Japan, March 1989.

2. Kasaba, Y., M. Ito, M. Ueno, S. Sato, M. Kimata, and N. Tsubouchi, Evaluations of 512×512 PtSi IR array, *Astronomical Society of Japan 1990 Fall Meeting*, Sendai, Miyagi, Japan, Oct. 1990.

3. Ueno, M., M. Ito, Y. Kasaba, S. Sato, M. Kimata, and N. Tsubouchi, PtSi Schottky-barrier 2-dimensional infrared array detector, *Astronomical Society of Japan 1990 Fall Meeting*, Sendai, Miyagi, Japan, Oct. 1990.

4. Kasaba, Y., Infrared survey of galaxies, *RIKEN Symposium on Cosmology by Observations of Galaxies*, Wako, Saitama, Japan, March 1991.

5. Kasaba, Y., M. Ito, M. Ueno, S. Sato, and T. Ichikawa, Test observation of PtSi NIR camera: First infrared images of M31, *Astronomical Society of Japan 1991 Spring Meeting*, Tokyo, Japan, Oct. 1991.

6. Ito, M., Y. Kasaba, M. Ueno, S. Sato, and T. Ichikawa, Test observation of PtSi NIR camera: Pilot observations of the Cygnus region, *Astronomical Society of Japan 1991 Spring Meeting*, Tokyo, Japan, Oct. 1991.

7. Ichikawa, T., M. Ueno, Y. Kasaba, S. Sato, Y. Mikami, Y. Torii, A. Yanagisawa, and M. Ito, Imaging of nearby galaxies by the wide-field infrared imager, *Astronomical Society of Japan 1991 Fall Meeting*, Mito, Ibaraki, Japan, Oct. 1991.

8. Kasaba, Y., M. Ueno, S. Sato, and T. Ichikawa, Super Wide-field Infrared imager for Nearby Galaxies: SWING, *Astronomical Society of Japan 1991 Fall Meeting*, Mito, Ibaraki, Japan, Oct. 1991.

9. Kobayashi, Y., S. Sato, H. Miura, K. Waseda, K. Fang, T. Minezaki, and Y. Kasaba, Development of the infrared imager: PICNIC, *Astronomical Society of Japan 1992 Spring Meeting*, Osaka, Japan, May 1992.

10. Kasaba, Y., H. Kojima, H. Matsumoto, I. Nagano, and K. Hashimoto, Search for radio emission by Geotail satellite during SL-9 impacts, *Symposium of the Japanese Society for Planetary Sciences, "The Collision between Comet Shoemaker-Levy 9 and Jupiter"*, Nagoya, Japan, Oct. 1994.

11. Kasaba, Y., H. Kojima, H. Matsumoto, S. Chikuba, J. Koizumi, I. Nagano, K. Hashimoto, T. Murata, H. Hamada, T. Miyake, and S. Horiyama, Search for Jovian kilometric radiation by GEOTAIL spacecraft during the impact of comet Shoemaker-Levy 9, *Society of Geomagnetism and Earth, Planetary, and Space Sciences (SGEPSS) 1994 Fall Meeting*, Nagoya, Japan, Oct. 1994.

12. Murata, T., H. Matsumoto, H. Kojima, K. Otsuka, T. Iyemori, T. Nagai, and Y. Kasaba, AKR index: Proposal of a new index for substrom study, *Japan Earth and Planetary Science Joint Meeting*, Tokyo, Japan, March 1996.

13. Kasaba, Y., H. Kojima, and H. Matsumoto, Possibility of correlation between type III solar radio bursts and plasma environment / plasma waves around Earth, *Japan Earth and Planetary Science Joint Meeting*, Tokyo, Japan, March 1996.

14. Kasaba, Y., H. Matsumoto, R. R. Anderson, J.-L. Bougeret, M. L. Kaiser, Remote sensing of magnetosphere: GEOTAIL and WIND observation of discrete radio emissions in the Earth's magnetosphere, *GEOTAIL US-Japan Joint Workshop*, Sagamihara, Kanagawa, Japan, Oct. 1995.

15. Matsumoto, H., H. Kojima, Y. Kasaba, T. Murata, R. R. Anderson, H. Usui, Y. Omura, K. Hashimoto, I. Nagano, M. Tsutsui, and T. Okada, *Long-term variation of plasma wave features observed by GEOTAIL, SGEPSS 1995 Fall Meeting*, Kyoto, Japan, Oct. 1995.

16. Kasaba, Y., H. Matsumoto, R. R. Anderson, J.-L. Bougeret, and M. L. Kaiser, Remote sensing of magnetosphere: 1. The $2f_p$ emission from the terrestrial foreshock region, *SGEPSS 1995 Fall Meeting*, Kyoto, Japan, Oct. 1995.

17. Kasaba, Y., H. Matsumoto, R. R. Anderson, J.-L. Bougeret, and M. L. Kaiser, GEOTAIL and WIND observation of discrete radio emissions in the Earth's magnetosphere, *American Geophysical Union 1995 Fall Meeting*, San Francisco, USA, Dec. 1995.

18. Matsumoto, H., Y. Kasaba, K. Hashimoto, T. Murata, and R. R. Anderson, Distant tail view of averaged AKR spectral variation observed by GEOTAIL spacecraft, *American Geophysical Union 1995 Fall Meeting*, San Francisco, USA, Dec. 1995.

19. Kasaba, Y., H. Matsumoto, K. Hashimoto, and R. R. Anderson, Remote sensing of the magnetosphere: The angular distribution of AKR observed by GEOTAIL spacecraft, *GEOTAIL Joint Workshop*, Uji, Kyoto, Japan, March 1996.

20. Kasaba, Y., H. Matsumoto, M. J. Reiner, R. R. Anderson, J.-L. Bougeret, and M. L. Kaiser, Remote sensing of the magnetosphere: The $2f_p$ emission from the terrestrial foreshock region, *GEOTAIL Joint Workshop*, Uji, Kyoto, March 1996.

21. Kasaba, Y., H. Matsumoto, M. J. Reiner, R. R. Anderson, J.-L. Bougeret, and M. L. Kaiser, Remote sensing of magnetosphere: 2. The $2f_p$ emission from the terrestrial foreshock region, *Japan Earth and Planetary Science Joint Meeting*, Osaka, Japan, March 1996.

22. Kasaba, Y., H. Matsumoto, and R. R. Anderson, GEOTAIL observation of $2f_p$ emission around the terrestrial foreshock region, *COSPAR 1996 General Meeting*, Birmingham, UK, July 1996.

23. Matsumoto, H., H. Kojima, Y. Kasaba, T. Miyake, R. R. Anderson, and T. Mukai, T. Yamamoto, and S. Kokubun, Plasma waves in the upstream and bow shock regions observed by GEOTAIL, *COSPAR 1996 General Meeting*, Birmingham, UK, July 1996.

24. Anderson, R. R., H. Matsumoto, K. Hashimoto, Y. Kasaba, M. L. Kaiser, G. Rostoker, J.-L. Bougeret, J.-L. Steinberg, and I. Nagano, Low frequency terrestrial "Type III" bursts observed simultaneously by GEOTAIL and WIND, *Universal Radio Science International 1996 Meeting*, Lille, France, Aug. 1996.

25. Matsumoto, H., H. Kojima, Y. Kasaba, Y. L. Zhang, Y. Omura, D. Morikawa, S. Kudo, N. Miki, K. Otsuka, and R. R. Anderson, Upstream waves observed by GEOTAIL, *SGEPSS 1996 Fall Meeting*, Fuchu, Tokyo, Japan, Oct. 1996.

26. Kasaba, Y., H. Matsumoto, M. J. Reiner, J.-L. Bougeret, M. L. Kaiser, T. Mukai, and Y. Saito, Remote and in-situ observations of the electron foreshock: the $2f_p$ emission, plasma waves, and energetic particles, *SGEPSS 1996 Fall Meeting*, Fuchu, Tokyo, Japan, Oct. 1996.

27. Matsumoto, H., H. Kojima, Y. Kasaba, T. Miyake, R. R. Anderson, and T. Mukai, Plasma waves in the upstream and bow shock regions observed by GEOTAIL, *Chapman Conference on The Earth's Magnetotail: New Perspectives*, Kanazawa, Japan, Nov. 1996.

28. Kasaba, Y., H. Matsumoto, K. Hashimoto, R. R. Anderson, J.-L.Bougeret, M. L. Kaiser, X. Y. Wu, and I. Nagano, Remote sensing of the plasmapause during substorm: GEOTAIL observation of the continuum enhancement, *Chapman Conference on The Earth's Magnetotail: New Perspectives*, Kanazawa, Japan, Nov. 1996.

29. Reiner, M. J., Y. Kasaba, M. L. Kaiser, H. Matsumoto, and I. Nagano, $2f_p$ terrestrial foreshock emissions located by WIND/Geotail triangulation, *American Geophysical Union 1996 Fall Meeting*, San Francisco, USA, Dec. 1996.

30. Kasaba, Y., H. Matsumoto, M. J. Reiner, R. R. Anderson, T. Mukai, and Y. Saito, Remote sensing and in-situ observations of the terrestrial foreshock: GEOTAIL observation of $2f_p$ emission, *American Geophysical Union 1996 Fall Meeting*, San Francisco, USA, Dec. 1996.

31. Anderson, R. R., D. A. Gurnett, H. Matsumoto, K. Hashimoto, H. Kojima, Y. Kasaba, M. L. Kaiser, G. Rostoker, J.-L. Bougeret, J.-L. Steinberg, I. Nagano, and H. J. Singer, A multi-spacecraft, multi-discipline study of terrestrial low frequency radio bursts and their relationship to the dynamics of geomagnetic disturbances detected by ground and space-borne instruments, *American Geophysical Union 1996 Fall Meeting*, San Francisco, USA, Dec. 1996.

32. Kasaba, Y., H. Matsumoto, Y. Omura, R. R. Anderson, T. Mukai, Y. Saito, T. Yamamoto, and S. Kokubun Spacecraft observations and numerical simulations of 2fp waves in the electron foreshock, *The Fifth International School / Symposium for Space Simulations*, Uji, Kyoto, Japan, March 1997.

33. Kasaba, Y., H. Matsumoto, R. R. Anderson, T. Mukai, Y. Saito, Y. Omura, T. Yamamoto, and S. Kokubun, In-situ observations of waves and particles in the Earth's electron foreshock, *Japan Earth and Planetary Science Joint Meeting*, Nagoya, Japan, March 1997.

34. Kudo, S., K. Hashimoto, H. Matsumoto, H. Kojima, Y. Kasaba, and I. Nagano, Analysis of auroral myriametric radiation observed by GEOTAIL spacecraft, *Japan Earth and Planetary Science Joint Meeting*, Nagoya, Japan, March 1997.

Thesis papers

1. Kasaba, Y., Evaluation of performance and possible applications of 512×512 PtSi IR array, *Master's thesis, Kyoto University*, 1991.